UNIVERSITÀ
DEGLI STUDI
FIRENZE

DOTTORATO DI RICERCA IN
INGEGNERIA INDUSTRIALE

Indirizzo: Energetica e Tecnologie Industriali e Ambientali Innovative

CICLO XXIX

COORDINATORE Prof. Maurizio De Lucia

Experimental Analysis of Effusion Cooled Combustor Liners

Settore Scientifico Disciplinare ING-IND/09

Dottorando
Dott. Becchi Riccardo

Tutore
Prof. Facchini Bruno

Co-Tutor
Dr. Ing. Antonio Andreini

Coordinatore
Prof. De Lucia Maurizio

Anni 2013/2016

Acknowledgements

I wish to express my sincere appreciation to those who have contributed to this work and supported me in one way or the other during this experience.

First of all, I would like to state my gratitude to Prof. Bruno Facchini, for his support and for the great opportunity he offered me.

I take this opportunity to thank Ing. Antonio Peschiulli from Avio Aero for his valuable advices for the preparation of the present work. My sincere thanks go also to Prof. Francesca Satta and Prof. Sergio Camporeale for their helpful edits and precious suggestions in the writing of this thesis.

I wish to thank Dr. Antonio Andreini and Dr. Lorenzo Tarchi, for their continuous supervision and outstanding competence. A special mention is dedicated to my mentor and, most of all, my friend Alessio, we spent four years side by side and I really feel lucky for this. I am also indebted to all my colleagues for providing a stimulating and fun environment in which to learn and grow.

Finally, I want to express a special thank to Deborah and to my parents (and to Kowi) for their endless support, encouragement and affection.

Contents

Acknowledgements **i**

Abstract **XI**

Nomenclature **XIII**

1 Technical Background **1**

1.1 Combustors for aero-engines 3

1.2 Rich-Quench-Lean combustors 6

1.3 Lean combustion 7

2 Heat Transfer in Gas Turbine Combustion Chamber **15**

2.1 Aero-engine combustors flow field 16

2.2 Combustor liner cooling 20

2.2.1 Effusion cooling 22

2.3 Liner cooling literature review 27

2.4 Thesis motivations and outline 38

3 Measurement Techniques **43**

3.1 Flow field by particle image velocimetry 44

3.2 TLC steady state technique for HTC tests 49

3.2.1 Experimental procedure and data post-processing . . . 51

3.3 PSP for film effectiveness measurements 58

3.4 Measurement uncertainty 65

4 Experimental Apparatus **69**
4.1 Three sector test rig 69
4.1.1 TSTR test conditions 76
4.2 Cold side test rig 79
4.2.1 CSTR test conditions 83
4.3 Test matrix 87

5 Experimental Results **91**
5.1 Flow field of PERM injector 92
5.2 Hot side heat transfer 100
5.2.1 Geometries comparison: impact of the injection angle on heat transfer 105
5.3 Film cooling effectiveness 109
5.3.1 $90deg$ liner configuration 109
5.3.2 $20deg$ liner configuration 114
5.3.3 Geometries comparison: impact of the injection angle on film covering 118
5.4 Cold side heat transfer 122
5.5 Concluding remarks 127

6 Effusion Performance with Reactive Conditions **133**
6.1 Experimental apparatus 135
6.2 Test conditions 144
6.3 Preliminary results 146

Conclusions **153**

Bibliography **157**

List of Figures

1.1 Cayley's engraved disc: front (left) shows his design for a fixed-wing aircraft, back (right) shows how thrust is used to generate lift and overcome drag 1
1.2 Thrust/Weight ratio advancements for aero-engines [1] 2
1.3 Overall pressure ratio progress for aero-engines [1] 3
1.4 Sketch of the main three combustor concepts [4] 5
1.5 NO_x formation varying the air/fuel mixture [6] 5
1.6 Rich-Quench-Lean combustor concept [8] 7
1.7 Rich (a) / Lean (b) burn combustor geometries [10] 8
1.8 Injector concepts developed within NEWAC project (adapted from http://www.newac.eu) 10
1.9 Schematic and picture of PERM injection system [13],[14] . . . 11

2.1 Flow structures of a typical gas turbine combustor with a coaxial injector. [11] 16
2.2 Axial velocity distribution of a LDI injector at isothermal condition [25] 18
2.3 Isothermal (left) and stable reacting flow field (right) of a PERM injector [15] 19
2.4 Flow field within a combustor equipped with a PERM injection system [30] 20
2.5 Combustor liner cooling arrangements [31] 21
2.6 Effusion cooled liner 22
2.7 Combustor prototype of European Project NEWAC [35] . . . 23
2.8 Main geometrical parameters for an effusion arrangement . . . 24

2.9 Measured normalised heat transfer coefficient for low density ratio injection conditions [57] 30
2.10 Cooling effectiveness distributions varying the Blowing Ratio F [59] 31
2.11 Film effectiveness maps [61] 32
2.12 Cooling effectiveness (contour) and local blowing ratios (isolines) varying the pressure drop across effusion liner (top: $\Delta P/P_{eff} = 1\%$ and bottom $\Delta P/P_{eff} = 3\%$. [27] 34
2.13 View of dividing streamlines approaching orthogonal extraction [76] 36
2.14 Passage heat transfer coefficient maps varying Reynolds number [79] 37

3.1 Experimental set-up for PIV measurements 44
3.2 Adaptive correlation operating principle scheme 47
3.3 TLC calibration set-up 50
3.4 TLC calibration curve 51
3.5 RGB map of the effusion plate 52
3.6 $\dot{q}_{Joule}$ distribution on a portion of the multi-perforated liner . . 54
3.7 Meshed model for cold side heat flux evaluation 55
3.8 Iterative post-processing procedure 56
3.9 Photo-physical process governing the PSP operating principle [87] 58
3.10 PSP calibration apparatus 59
3.11 PSP calibration curves for three temperature values 60
3.12 Heat and mass transfer analogy for film cooling: thermal (a) and mass transfer (b) boundary conditions [89] 61
3.13 Block diagram of the PSP post-processing procedure 64

4.1 Cross sectional view of the three sector test rig 70
4.2 Perm injectors installed on the test rig 70
4.3 Swirlers flow check experimental apparatus 71
4.4 Effusion plate with Inconel foil 72
4.5 Sketch of PIV set-up 73

4.6 Test section set-up for HTC measurements. View of TLC activation for smooth liner [13] 74
4.7 Cross sectional view of the cold side test rig 79
4.8 Top view of the annulus channel; location of pressure and temperature sensors 81
4.9 Hexa grid mesh (left). Top view of flow streamlines obtained with $k-\epsilon$ turbulence model (right) 81
4.10 Investigation areas used in the HTC post-processing procedure 84
4.11 Tested SR values as a function of Reynolds number. 85
4.12 Spatially averaged overall and adiabatic effectiveness distributions [58] 87

5.1 PERM flow field with no coolant injection ($\Delta P/P_{eff} = 0\%$ and $W = 0\%$) 93
5.2 PERM flow field with only effusion coolant injection ($\Delta P/P_{eff} = 3\%$ and $W = 0\%$) 94
5.3 PERM flow field with effusion and slot coolant injection ($\Delta P/P_{eff} = 3\%$ and $W = 3\%$) 95
5.4 Axial velocity profiles for various streamwise locations 96
5.5 Flow field comparison varying the holes injection angle 97
5.6 Axial velocity profiles: Impact of the injection angle 98
5.7 Heat transfer coefficient distribution on the smooth liner geometry ($\Delta P/P_{eff} = 0\%$ and $W = 0\%$) 101
5.8 $90deg$ liner HTC distributions: effect of the effusion pressure drop 102
5.9 Laterally averaged HTC distributions varying the effusion mass flow rate ($W = 0\%$) 103
5.10 $90deg$ liner HTC distributions: impact of slot cooling 104
5.11 Laterally averaged heat transfer coefficient distributions: impact of slot cooling ($\Delta P/P_{eff} = 3\%$) 104
5.12 Laterally averaged heat transfer coefficient distributions: impact of the holes injection angle ($\Delta P/P_{eff} = 3\%$ and $W = 0\%$) 105
5.13 Laterally averaged HTC distributions: impact of slot injection 107
5.14 HTC results comparison within different experimental campaign 108

5.15 $90deg$ adiabatic effectiveness maps: effect of the effusion pressure drop . . . 110
5.16 Laterally averaged adiabatic effectiveness distributions: impact of effusion pressure drop ($W = 0\%$) . . . 111
5.17 $90deg$ adiabatic effectiveness maps: impact of slot cooling . . . 112
5.18 Laterally averaged adiabatic effectiveness distributions: impact of slot cooling . . . 114
5.19 $20deg$ adiabatic effectiveness maps: effect of the effusion pressure drop . . . 115
5.20 $20deg$ laterally averaged η_{ad} distributions: impact of effusion pressure drop ($W = 0\%$) . . . 116
5.21 $20deg$ adiabatic effectiveness maps: impact of slot cooling . . . 117
5.22 Laterally averaged adiabatic effectiveness distributions: impact of slot cooling . . . 118
5.23 Adiabatic effectiveness maps: geometries comparison varying cooling conditions . . . 119
5.24 Laterally averaged η_{ad} distributions: comparing different geometries . . . 121
5.25 Nusselt number maps varying the ByPass ratio($\Delta P/P_{eff} = 3\%$) 122
5.26 Nusselt number 1D distributions varying $ByR(\Delta P/P_{eff} = 3\%)$ 123
5.27 Nusselt number 1D distributions varying $\Delta P/P_{eff}$ ($ByR = 40\%$) 124
5.28 Enhancement Factor as a function of SR . . . 125
5.29 Enhancement factor correlation . . . 126
5.30 Net Heat Flux Reduction distributions for different cooling conditions . . . 128

6.1 Cross sectional view of the reactive combustor rig . . . 135
6.2 Air flow distribution across the combustor . . . 136
6.3 PERM injector fabricated by rapid prototyping (courtesy of Avio Aero) . . . 137
6.4 Combustor fuel manifolds . . . 137
6.5 Test cell skid fuel . . . 138
6.6 Effusion liner (courtesy of Avio Aero) . . . 139
6.7 Flame detector optical device . . . 140

6.8 Reference cold junction with 90 K-type thermocouples connected 142
6.9 Thermocouples location on the liner surface 146
6.10 Metal temperature distributions in the streamwise direction. Outer liner: top. Inner liner: bottom 147
6.11 Metal temperature distributions in the spanwise direction on the outer liner 148
6.12 Flame video snapshots 149
6.13 DMLS components final inspection (courtesy of Avio Aero) . . 151

List of Tables

3.1 Uncertainty analysis 66

4.1 Flow conditions achieved on the TSTR 78
4.2 Flow conditions imposed in the cold side HTC investigation . 83
4.3 Test matrix 88

6.1 Reported operating points 145

Abstract

The introduction of stricter and stricter NO_x emissions standards in civil aero-engines is forcing all engine manufacturers to adopt Lean Burn concept as basic scheme for combustors. With this type of devices a high amount of air flow is admitted through the injection system (up to 70% of total air mass flow) in order to reduce and control primary zone fuel/air ratio. This has two consequences: first of all, for the sake of flame stabilization, primary air is injected with relevant swirl components producing very complex flow structures such as recirculations, vortex breakdown and precessing vortexes, which may deeply interact in the near wall region of the combustor liner. Secondly, a reduced amount of air is available for combustor liner cooling, pushing the adoption of high effectiveness cooling schemes.

Among different cooling approaches, effusion or full-coverage film cooling, realized with the multi-perforation of the liner in single or double skin solutions, represents one of the first choices due to its high thermal effectiveness, low weight and a relatively easy manufacturability. Liner metal temperature is kept low by the combined protective effect of coolant film, heat removal inside holes and convection on the cold side. The evolution of film protection, which represents the dominant contribution to overall effectiveness, can be heavily influenced by the aforementioned swirl flow interaction with combustor walls.

A large part of the activities and the achievements deriving from the Ph.D. course are collected on an experimental apparatus, developed within EU project LEMCOTEC, consisting of a non-reactive three sectors planar rig. The test model is characterized by a complete cooling system and three

swirlers, replicating the geometry of a Avio Aero PERM (Partially Evaporated and Rapid Mixing) injector technology. The final aim of the study is the experimental characterization of the flow field and the measurement of cooling performance in terms of heat transfer coefficient and adiabatic effectiveness, due to the interaction of the swirling flow coming out from the injectors and the cooling scheme. Particular attention is focused on the impact on the effusion system of the coolant injection angle, for this purpose three different liner configurations are tested. To deepen the comprehension and the knowledge on the thermal behaviour of the system, a supplementary investigation is carried out with the aim of estimating the heat transfer on the annulus side of the liner for the reference effusion geometry.

To enhance the TRL (Technology Readiness Level) of experiments and to stress the capability of alternative manufacturing technologies, a new test rig is developed within EU project IMPACT-AE. It consists of a linear three sector combustor, whose main parts are manufactured using metal laser sintering technologies, equipped with an effusion cooling scheme on both the outer and inner liners. The same PERM injector concept is exploited to provide fuel atomization and flame stabilization. A large number of thermocouples are embedded into the combustor walls to monitor continuously the metal temperature. Such apparatus gives the opportunity of testing the key components of the combustion chamber in reactive conditions, achieving an important step toward their implementation in the engine.

Nomenclature

Symbols

A	Area	$[m^2]$
BR	Blowing ratio	$[-]$
ByR	By-pass ratio	$[-]$
C	Mass fraction	$[-]$
d	Holes diameter	$[m]$
D	Outlet injector diameter	$[m]$
d_h	Test section hydraulic diameter	$[m]$
DR	Density ratio	$[-]$
I	Light intensity	$[counts]$
EF	Heat transfer enhancement factor	$[-]$
FAR	Fuel air ratio	$[-]$
h	Slot height	$[m]$
HTC	Heat transfer coefficient	$[W/(m^2K)]$
L	Holes length	$[m]$
Le	Lewis number	$[-]$
$\dot{m}$	Mass flow rate	$[kg/s]$
$NHFR$	Net heat flux reduction	$[-]$
M	Molar mass	$[kg/kmol]$
MR	Momentum ratio	$[-]$
Nu	Nusselt number	$[-]$
OPR	Overall Pressure Ratio	$[-]$
P	Static pressure	$[Pa]$
$\dot{q}$	Heat flux	$[W/m^2]$
Re	Reynolds number	$[-]$
S_x	Streamwise hole pitch	$[m]$
S_y	Spanwise hole pitch	$[m]$

Sc	Schmidt number	$[-]$
SR	Suction Ratio	$[-]$
Stk	Stokes number	$[-]$
S_N	Swirl number	$[-]$
T	Temperature	$[K]$
TIT	Turbine inlet temperature	$[K]$
U	Velocity	$[m/s]$
VR	Velocity ratio	$[-]$
W	Slot coolant consumption	$[-]$
x	Axial direction	$[m]$
y	Lateral direction	$[m]$
z	Orthogonal to test plate direction	$[m]$

Greeks

α	Hole inclination angle	$[deg]$
β	Compound angle	$[deg]$
η_{ad}	Adiabatic effectiveness	$[-]$
η_{ov}	Overall effectiveness	$[-]$
θ	Dimensionless temperature	$[-]$
λ	Thermal conductivity	$[W/(mK)]$
μ	Dynamic viscosity	$[Pa \cdot s]$
ρ	Density	$[kg/m^3]$
σ	Perforation porosity	$[-]$
τ	Particle relaxation time	$[s]$
ϕ	Equivalence ratio	$[-]$

Subscripts

0	No coolant injection
air	Air
ann	Annulus
aw	Adiabatic wall
$bleed$	Bleed flow
$cool$	Cooling flow
$corr$	Correlation
CS	Liner cold side
$dark$	Dark image
eff	Effusion flow
fg	Foreign gas
in	Inlet
$Joule$	Joule effect
$loss$	Loss
$main$	Mainstream
max	Maximum
$pilot$	Pilot fuel line
ref	Reference
O_2	Oxygen
out	Outlet
$slot$	Slot cooling system
w	Wall
x	Axial direction
y	Lateral direction

Acronyms

CCD	Couple Charged Device
$CSTR$	Cold Side Test Rig
$DMLS$	Direct Metal Laser Sintering
EDM	Electrical Discharge Machining
FEM	Finite Element Method
LDA	Laser Doppler Anemometry
LDI	Lean Direct Ignition
LES	Large Eddy Simulation
LPP	Lean Premixed Prevaporised
$PERM$	Partially Evaporated and Rapid Mixing
PIV	Particle Image Velocimetry
$PMMA$	Poly-Methyl Methacrylate
POD	Proper Orthogonal Decomposition
PSP	Pressure Sensitive Paint
PVC	Precessing Vortex Core
$QDRV$	Quick Design Rapid Validation
$RANS$	Reynolds Averaged Navier-Stokes Equations
RQL	Rich Quench Lean
RCZ	Recirculation Zone
SST	Shear Stress Transport
TLC	Thermocromic Liquid Crystals
TRL	Technology Readiness Level
$TSTR$	Three Sector Test Rig
ULN	Ultra Low NO_x

Chapter 1

Technical Background

Contents

1.1	**Combustors for aero-engines**	**3**
1.2	**Rich-Quench-Lean combustors**	**6**
1.3	**Lean combustion**	**7**

For more than two hundreds years the world of aviation has been a world of innovation. Since 1799, when Sir George Cayley (1773 – 1857) set the basis for modern air-plane concept showing the aerodynamic forces that govern heavier-than-air flight (Fig. 1.1), a long way has been travelled. Wright brothers first human flight in 1903 represent the greatest and most recognised milestone in the *air-conquest*, equally the contributions on jet propulsion carried in the late 30's by two distinct studies in England and in Germany left

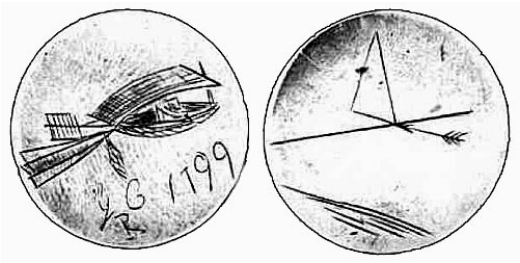

Figure 1.1: Cayley's engraved disc: front (left) shows his design for a fixed-wing aircraft, back (right) shows how thrust is used to generate lift and overcome drag

an indelible mark on future aircrafts. The English Royal Air Force engineer Frank Whittle was the first to register a patent for a turbojet engine in 1930 and the first flight based upon his concept took place in 1941. Almost simultaneously, Hans von Ohain was granted a patent for his turbojet engine in 1936 and his jet was the first to fly in 1939.

Turbojet engines have become rapidly the standard solution for flight propulsion and have arrived to our days through continuous and impressive technological improvements. According to Ballal and Zelina [1], almost seven times superior thrust/weight ratios have been achieved (Fig. 1.2) and, while the early jet prototypes barely lasted for less than 10 hours, modern civil engines can stay on wings for up to 10000 hours. Advances in blade cooling technologies and high-temperature materials have permitted an increase in turbine inlet temperature (TIT) from $970K$ to $2030K$ and, thanks to the outstanding performance of today's fans and compressors, engines can now reach overall pressure ratios (OPR) up to 45 (Fig. 1.3).

These developments have resulted in a constant decay of thrust specific fuel consumption during years, but have also involved significant issues. TIT and OPR strongly affects the design of the combustion chamber, which represents from a thermal point of view one of the most critical components of the

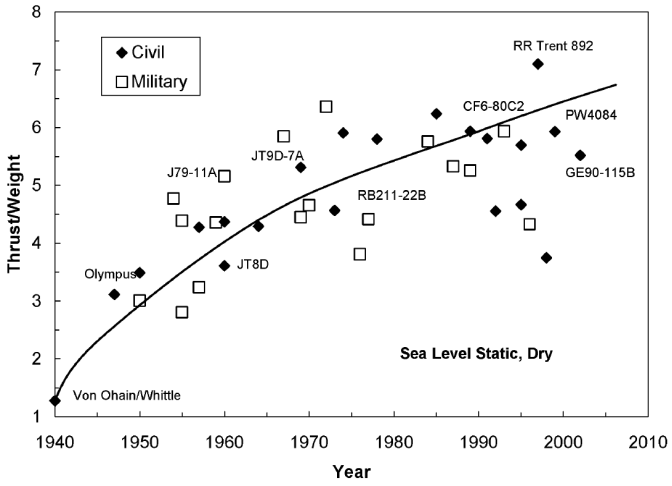

Figure 1.2: Thrust/Weight ratio advancements for aero-engines [1]

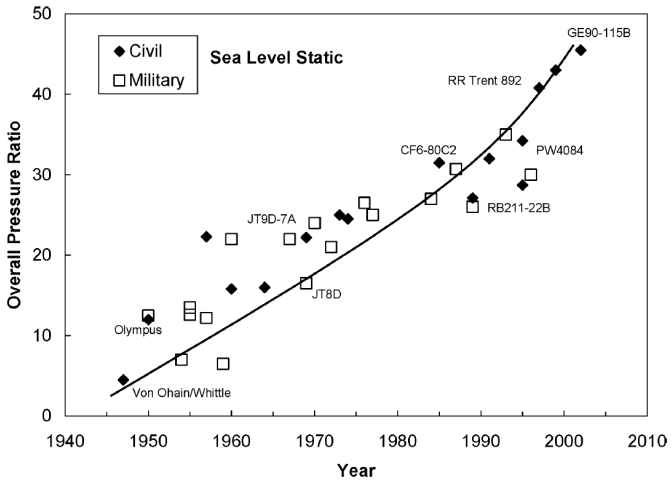

Figure 1.3: Overall pressure ratio progress for aero-engines [1]

engine. An enhancement in OPR, not only, leads to an higher temperature at the compressor discharge, limiting the cooling capacity of the air destined to combustor liners, but involves also an increase of radiative thermal loads in the chamber. Therefore, the definition and the optimization of the most appropriate cooling scheme represents one of the most challenging tasks in the combustor design, since it directly determines the component life.

In relatively recent years, an other important concern has arisen in aero-engine design, this is represented by the environmental impact of air traffic and the consequent strict regulations regarding pollutant emissions. In 2015, air passengers traffic has grew up by 6.8% in terms of Revenue Passenger Kilometres (RPKs) [2] and forecast predict for year 2034 more than seven billion people taking to the skies [3], making the achievement of an environmental-friendly aviation even more essential.

1.1 Combustors for aero-engines

Combustors represent the *burning heart* of gas turbines and their design deals with several fields of engineering, as chemistry, fluid dynamics, heat

transfer and structural mechanic, deeply interacting each other. Most of the basic features of current gas turbine combustor were already well-known since the 1950's, from that time a gradual and continuous development was achieved in order to satisfy new requirements and needs.

Earliest aircraft applications employed so called *can* combustors (Fig. 1.4a), characterized by separate cylindrical chambers spaced concentrically around the engine shaft. Each casing possesses its own liner and fuel supply, entailing relatively limited efforts for development (process can be performed on a single can, employing only a fraction of the total air and fuel) and reduced maintenance time. The excessive weight and size instead have represented the main disadvantages of this configuration, essentially impeding its use on current aircraft design.

Separate tubular liners are maintained also in *tubo-annular* combustors (Fig. 1.4b), however in this case a single annular casing is present surrounding the circularly arranged flame tubes. This arrangement aims to couple the strength and the versatility of the can concept to an increased compactness, establishing as the selected choice in several engines by major manufacturers.

Nowadays the ideal configuration has been identified in *annular* combustion chamber concept (Fig. 1.4c), where a single annular liner is installed concentrically inside a single annular casing. This configuration leads to the maximum possible compactness of the component and to limited pressure losses. Its main drawbacks are related to the structural weakness of the chamber external walls and to high development costs, however these issues have been practically overcome during years and annular combustion chambers have been established as the automatic choice for aircraft engines.

Development of gas turbine for propulsion applications has been driven for years by the goal of increasing performance and efficiency, however the stringent regulations of these last decades on pollutant emissions have led engine manufacturers to develop new combustors concepts able to meet various regulatory requirements. Nitrous oxides (NO_x), carbon monoxide (CO), carbon dioxide (CO_2) and unburned hydrocarbon (UHCs) are some of the pollutant gaseous species that composed the exhaust products of an aero-engine; in particular among these, NO_x abatement is considered a mayor

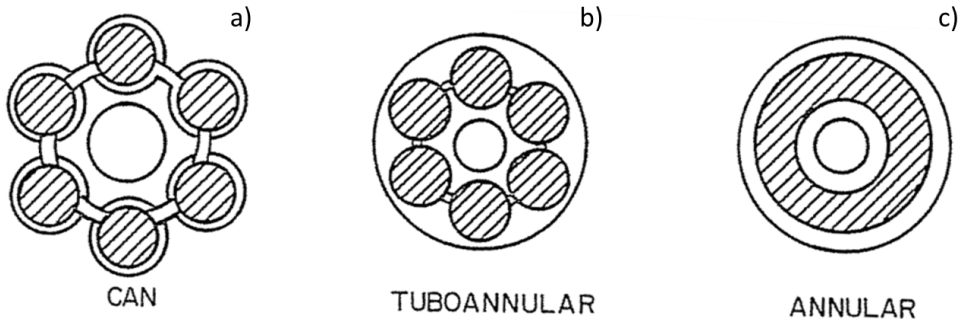

Figure 1.4: Sketch of the main three combustor concepts [4]

target for the industrial and scientific community with an ambitious goal of a 90% reduction in emissions set for 2050 (from a 2011 baseline)[5].

Different processes contribute to nitrous oxides formation, the most relevant for aero-engine combustors is represented by Zeldovich mechanism [7], that leads to the production of the so called Thermal NO_x through the oxidation of atmospheric nitrogen in high temperature regions of the flame

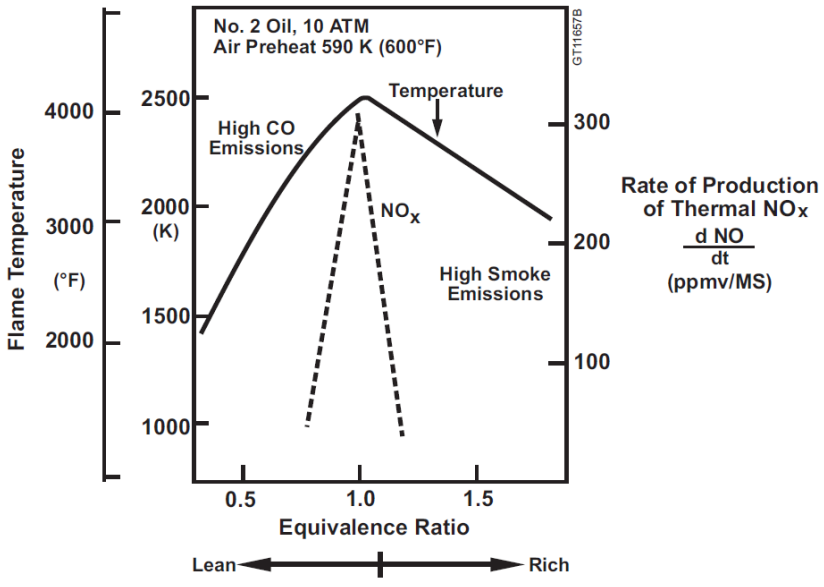

Figure 1.5: NO_x formation varying the air/fuel mixture [6]

and in the post-flame gases [4]. As showed in Fig. 1.5, within the combustion process the peak of temperature, and consequently of NO_x production, occurs in proximity of the air-fuel stoichiometric value, therefore emissions abatement efforts head towards avoiding this condition.

It is straightforward that opposite approaches can be exploited, moving towards high equivalence ratio, as in RQL (Rich-Quench-Lean) concept, or opting for values of ϕ significantly below the unity (lean combustion).

1.2 Rich-Quench-Lean combustors

Operating with a fuel rich mixture in the primary zone leads to a reduction of the flame temperature and to a decrease of the concentration of available oxygen for nitrous oxides formation. On the other hand, locally rich conditions generate excessive amounts of CO, unburned hydrocarbons and soot. A solution to exploit advantages and reduce hazards can be represented by a process of staged combustion, currently employed by the most of aero-engines in the civil aviation by means of Rich burn - quick Quench - Lean burn (RQL) concept.

As sketched in Fig. 1.6, fuel is injected in the primary rich-burn zone ($\phi = 1.2-1.6$) where it mixes via turbulent and molecular diffusion with part of the air flow coming from the compressor; this rich zone guarantees an high resistance to blow out, keeping the combustion process stable at low power conditions where the combustor overall is running very lean. Subsequently, the gas, characterized by high quantities of partially oxidized hydrocarbon species, hydrogen, and carbon monoxide, is diluted by means of the addition of an high quantity of air through wall jets (dilution holes) to favour a rapid mix and to support a quenching of the reactions, that leads to lean conditions ($\phi = 0.5 - 0.7$) at the exit of the combustor.

In contra-position to wide stability limits and range of operation, some important issues are related to RQL combustor technology, all connected to the need of avoiding $\phi = 1$ condition. The most critical aspect concerns the velocity of the transition from Rich to Lean phase, if the mixing process be-

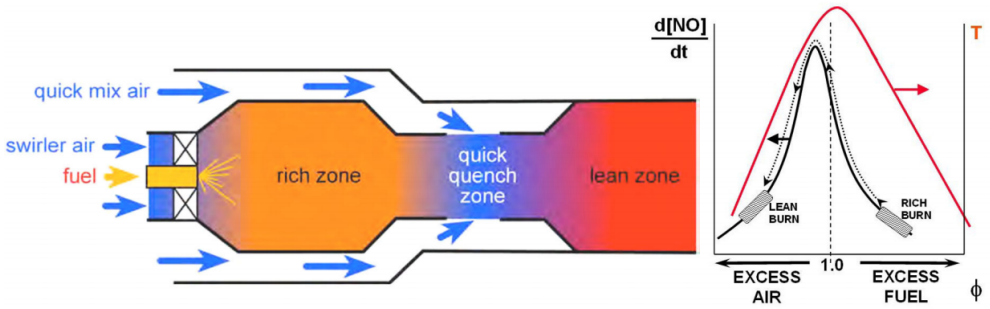

Figure 1.6: Rich-Quench-Lean combustor concept [8]

tween gas and air dilution jets isn't enough rapid, pockets of hot gas would last for a sufficient time to reach near-stoichiometric conditions, leading to the generation of significant amounts of NO_x. Furthermore, the chamber design must avoid recirculation regions in some locations which can increase gas residence time [9]. Regarding the combustor cooling, the adoption of techniques based on liner film protection may produce locally stoichiometric conditions near the walls, entailing a different design perspective which paradoxically places the cooling requirements on a secondary plane.

1.3 Lean combustion

The intrinsic limits connected to RQL approach and the consequent difficulties to overcome for respecting the even more stricter emissions standards, can explain why nowadays the major aero-engines manufacturers are pushing towards the implementation of lean combustion systems, operating with an high excess of air in the combustor primary region. The aim is to reduce flame temperature and to avoid the formation of diffusion flames where the fuel locally burns at stoichiometric conditions. For this reason, fuel and air should be accurately mixed before entering the combustion zone.

Lean technology is already largely employed in gas turbines for land-based industrial applications, facilitated by the use of gaseous fuels which

allow to obtain a good level of mixing without serious complexity. The situation becomes more challenging for aero-engine combustor where the use of liquid fuels is mandatory. Combustible must be atomized into small droplets, vaporized and then distributed in an air stream, where an effective mixing must be achieved before the admission in the flame zone. Moreover, the process is deeply influenced by the operating conditions (e.g. air temperature and inlet pressure) and it is difficult to scale various non-linear effects, therefore different technologies must be exploited depending on the size and the cycle of the engine.

As illustrated in Fig. 1.7, in conventional rich-burn combustor, the fuel is injected directly into the combustion chamber along with approximately the 30% of the total air, while employing a lean combustion strategy the amount of air entering through the injector and the cowl rises up to 70%. To accommodate this increased mass flow requirement, without excessively enhancing the pressure drop, lean burn injectors are significantly larger than those currently in use within rich burn architecture [10]; furthermore a re-

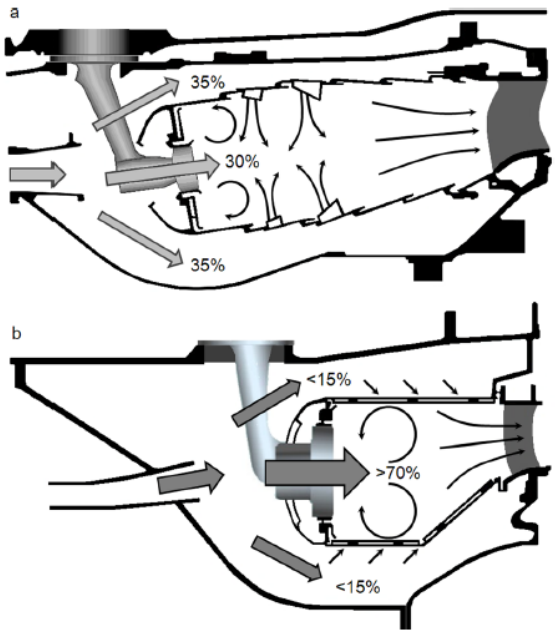

Figure 1.7: Rich (a) / Lean (b) burn combustor geometries [10]

duced amount of cooling air is available for the combustor dome and the liner walls, demanding for the design of efficient cooling systems to safeguard the components integrity.

With respect to engine operating with diffusion flames, lean combustion implies some critical concerns to take care: the high air-fuel ratios in the primary zone lead the combustor to operate near the lean blow-out limits, requiring the adoption of proper strategies for flame stabilization. Therefore the fuel injector, in addition to its primary function of preparing and injecting the combustible mixture, must be act as a sensitive element capable of modulating the flow field and the combustion processes in the chamber. The majority of engine employs swirl injectors in order to generate central toroidal recirculation zones to provide the dominant flame stabilization mechanism. The flow in this region is generally associated with high shear stresses and strong turbulence intensity resulting from vortex breakdown [11].

Different types of injectors can be distinguished depending on the basic physical mechanism used to generate liquid fuel atomization. Basically, two different concepts of injectors are used in the aero-engine field: pressure atomizers and airblast atomizers. The same operating principle is adopted in both systems, with the liquid combustible stream and the gas-phase interacting with each other with a high relative velocity which generates strong aerodynamic stresses leading to the fragmentation into droplets. In pressure atomizers a high velocity jet or sheet is injected into a low velocity medium whereas airblast atomizers employ the kinetic energy of the flowing high velocity air-stream to disintegrate the fuel into drops. The last ones represent the prominent technology in gas turbine applications with high pressure ratio, showing some clear advantages with respect pressure atomizers, as the request of lower fuel pressure, the generation of a finer spray, low soot formation and little changes in performance over a wide range of operating conditions [12].

Several advanced configurations have been developed during years, yearning for an efficient lean burn combustion process. These systems have been designed as internally staged injectors, with pilot and main streams

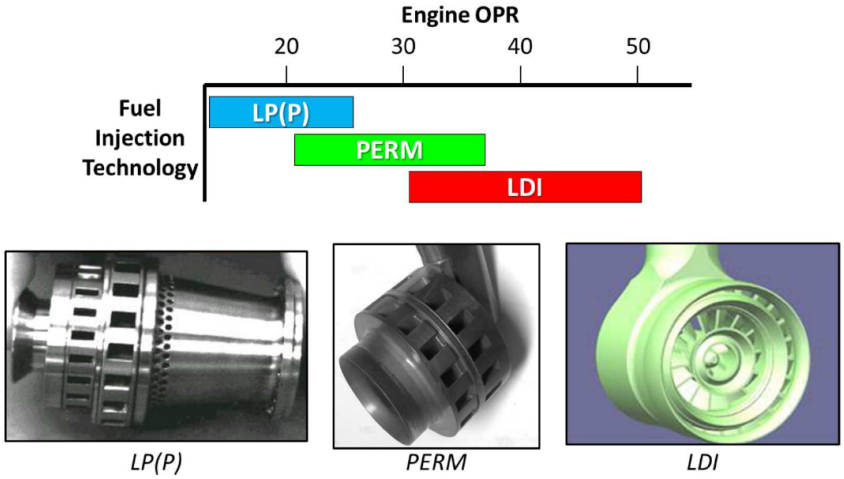

Figure 1.8: Injector concepts developed within NEWAC project (adapted from http://www.newac.eu)

combined employing the two atomization concepts, and multiple swirling channels. In Fig. 1.8 have been showed the three injector concepts studied within the integrated project co-funded by the European Commission, within the Sixth Framework Programme, named NEWAC (New Aero Engine Core Concepts).

Lean Premixed Prevaporised (LPP) technology represents a plausible choice for low OPR applications, their working principle is based on the action of two distinct air flows: one has the task to provide a good liquid combustible atomization, while the second supports the mixing process and the fuel evaporation. Furthermore, the combination of the two acts also as a promoter for the flame stabilization in the combustor. Intrinsically this concept has the greatest potential for nitrous oxides reduction, since allows the formation of a highly homogeneous air-fuel mixture before the entering in the combustion chamber.

The primary concern on LPP combustors is related to flashback and auto-ignition phenomena, that may occur in the premixing duct especially at high operating pressure. This issue makes their application on future aircraft extremely challenging, explaining why most of the attention of aero-engine

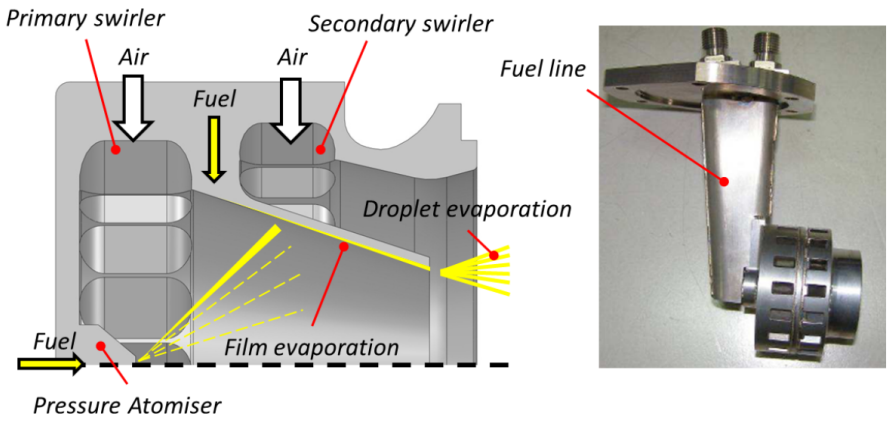

Figure 1.9: Schematic and picture of PERM injection system [13],[14]

manufacturer has been moved on to different systems.

Lean Direct Injection (LDI) combustors differ from the LPP systems as the fuel is injected directly into the flame zone, where it is simultaneously vaporized, mixed and burned. As the fuel is not premixed and pre-vaporized, to keep low the flame temperature and to avoid hot spots it is important to achieve a fine atomization of the fuel. Furthermore, to ensure a stable operating range, fuel staging is arranged within the injector. Thanks to their wide stability limits and the absence of flashback and auto-ignition risks, suitable application for LDI injectors is represented by high OPR engines.

Partially Evaporated and Rapid Mixing (PERM) injection system, developed by Avio Aero, is the third concept taken into consideration and on its improvement and optimization has focused the attention the collaborative project LEMCOTEC (Low Emissions Core-Engine Technologies), developed by the European Commission within the Seventh Framework Programme (2007-2013). PERM technology (Fig. 1.9) consists of a double swirler air-blast atomizer designed with the aim of achieving partial evaporation inside the inner duct and rapid mixing within the combustor, optimising the location and the stability of the flame.

A double fuel supply is involved, the primary injection is accomplished in the inner swirler by means of an hollow cone pressure atomizer, which

provides a fuel spray within the injector nozzle able to generate a stabilizing pilot flame. The secondary fuel is supplied as a thin layer of liquid combustible generated on the inner surface of the nozzle lip. As the film reaches the edge of the lip, it is broken up generating fine droplets, that under the action of the two co-rotating swirled flows contribute to mixture rapid mixing. The pilot injector is usually active within the entire operating range with a variable fuel split between pilot and main stage.

PERM concept has demonstrated to overcome typical issues related to LPP injectors, avoiding inherent risk for auto-ignition and flashbacks, that may lead to integrity problems for the burners and the combustor, and establishing itself as a suitable solution on medium/high OPR engines. Nevertheless, crucial attention must be paid under some operating conditions, as IDLE operation at low power, where the flame is quite susceptible to extinction near the lean blowout [15]. As already stated previously, this type of injector is distinguished by an extremely high amount of air directly supplied to the nozzle, making extremely arduous the task conferred to the liner cooling scheme due to the reduced air availability.

A common problem faced by lean combustor design is represented by the onset of thermo-acoustic instabilities. Large amplitude oscillations in pressure and velocity can establish in the chamber, due to unstable phenomena related to the coupling between the acoustic field and heat release fluctuations of the flame. Although combustion instability is not considered to be an issue for diffusion flames, this phenomenon becomes influential for combustors operated near the lean blowout limit, and characterized by shorter axial extension, which shifts the instabilities to higher frequencies.

The presence of such instabilities can compromise the integrity of the combustion chamber, leading to serious safety problems and reducing deeply the components life. Therefore, a control and a mitigation of thermo-acoustic phenomena is absolutely required and is carried out by different ways, based on both active or passive control methods. Dealing with this aspect, multi-perforated liners are hence very attractive in aero-engine field for their acoustics damping characteristics, allowing to combine an efficient cooling system

to a device intrinsically capable to mitigate undesired pressure fluctuations.

Within this scenario, several European projects have been funded during the last years with the aim of identifying the technology routes to meet the targets set by the Advisory Council for Aeronautics Research and Innovation in Europe (ACARE) for 2020 [16]. In this regard, the activities leading to the results presented in this dissertation were carried out within the context of two European projects called LEMCOTEC (Low Emissions Core-Engine Technologies) and IMPACT-AE (Intelligent Design Methodologies for Low Pollutant Combustors for Aero-Engines). The main technological objective of LEMOCTEC project is the improvement of the core-engine thermal efficiency by increasing the overall pressure ratio. Specifically, the University of Florence has been involved, as a scientific partner of Avio Aero, in the subproject SP3, aiming to develop lean combustion technologies suitable with new engine requirements. The partner project IMPACT has the purpose of developing design methods suitable to scale combustor geometries for future aero-engine architectures, in detail the experimental survey reported in the present work deals with the modelling and design of advanced combustor wall cooling concepts for combustion chamber liner.

Chapter 2

Heat Transfer in Gas Turbine Combustion Chamber

Contents

2.1 Aero-engine combustors flow field 16

2.2 Combustor liner cooling 20

2.2.1 Effusion cooling 22

2.3 Liner cooling literature review 27

2.4 Thesis motivations and outline 38

In a lean combustor, an increased amount of air is needed for the fuel preparation and therefore is introduced in the combustion chamber directly through the injection system: as a consequence, a strong reduction of air available for cooling purposes is required. In addition, the enhancement of the performance of the whole engine passes through an increasing of the overall pressure ratio, leading to an higher cooling air temperature at the inlet of the combustor and so reducing its cooling capacity. A further parameter subjected to a substantial growth in new engine development is the maximum chamber temperature, resulting in a more problematic management of the working temperatures of the walls. Considering all these aspects, it becomes obvious that the design of more efficient cooling technologies is mandatory.

2.1 Aero-engine combustors flow field

In the design of a well-performing cooling scheme for combustor liners a significant role is played by a thorough comprehension of the combustion chamber flow field. Modern injectors for combustion chamber involve the presence of high swirling and expanding flows, that deeply affect the thermal balance of the combustor walls and tend to interact with the liner cooling flows, varying their behaviour and effects.

The swirl intensity is usually characterized by the swirl number S_N, commonly defined as the ratio of the axial flux of the tangential momentum to the product of the axial momentum flux and a characteristic radius [17]. A critical value of $S_N = 0.6$ was identified as the minimum swirl level essential to achieve a central recirculation zone, induced by the vortex breakdown, and other typical lean systems flow structures reported in the sketch of Fig. 2.1.

Several works dealt with the characterization of the flow structures generated by swirlers, exploiting both numerical and experimental approaches. Vu and Gouldin [18] performed time mean and fluctuating flow field measurements, by means of a directional Pitot probe and hot-wire anemometer, in a model combustor composed of two confined coaxial swirling jets. Tests

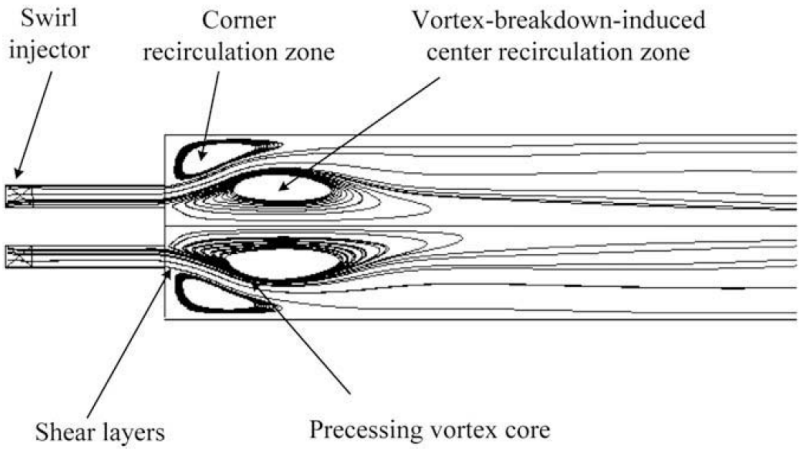

Figure 2.1: Flow structures of a typical gas turbine combustor with a coaxial injector. [11]

were carried out in non-reactive conditions and results revealed limited tangential velocities in the RCZ, while levels of turbulence and dissipation rate were rather significant. Rhode et al. [19] presented mean flow field studies in axisymmetric combustor geometries with swirl. Six different flow field configurations were investigated with various side-wall and swirl vane angles. The length and the width of the recirculation zone was found to increase with swirl vane angle until a critical angle was reached, after which any further increase in swirl shortened the length, but continued to increase the width. The major effect of side wall expansion angle was to shorten the corner recirculation region, with no major effects on the central recirculation.

Simultaneous two-component velocity measurements, including the spatial distribution of normalized Reynolds stress, were performed by Brum and Samuelson [20] in a complex flow swirl stabilized combustor model using a two-color laser anemometer. Small-scale form intermittences were manifested and associated with an oscillation of the recirculation zone, and a precessing vortex core. A strong impact on the flow field structure can be ascribed to the presence of reactive processes, resulting in increased values of normalized Reynolds stress, an enhanced rate of back-mixing, and a shorter and wider zone of recirculation. Syred et al. [21] used a two component laser anemometry system to measure the flow field due to the interaction of PVC and the reverse flow zone in the exhaust of a swirl burner.

In more recent years, an exhaustive study was performed at Loughborough University [22, 23] on an annular full scale three sector isothermal model of a gas turbine combustor, employing Particle Image Velocimetry, Laser Doppler Anemometry (LDA) and hot wire measurements, coupled with LES calculations. A better understanding of the aerodynamics of the flow field, on an instantaneous and time mean basis, was achieved, focusing the attention on particular aspects as the annular jet impingement and the interaction of the swirled flow with the primary jets. Furthermore, analysis of data, using techniques such as conditional averaging and correlation fields, also allows the organized flow structures to be extracted from the global flow field. Gnirß and Tropea [24] performed PIV and concentration measurements using POD (Proper Orthogonal Decomposition) analysis on a gas-turbine model com-

posed by 5 swirlers in planar arrangement. The most dominant mode showed a symmetric deformation of the flow field, coupled with a change of concentration especially in the corner vortex and downstream regions. Other modes showed asymmetric deformation of the flow field or reveal vortex structures of the PVC. However none of them influenced the corresponding concentration distribution in a significant way.

The majority of the works reported above deal with flow field analysis of injector developed for traditional diffusive combustor, however in the last years with the growing interest on development and optimization of lean combustion concept, several authors have carried out flow field investigations on novel Ultra Low NOx (ULN) technologies.

Different swirler configurations on a LDI burner were investigated in isothermal flows and combustion cases by Li and Gutmark [26]; the effects on the development of recirculation zones, velocity field, temperature distribution, flame structure and emissions were studied. Wurm et al. [25, 27] carried out the investigation of swirled combustion chamber flows in a three sector scaled test facility equipped with LDI injector at isothermal condition. An engine representative cooling scheme was included in the test apparatus, in order to asses the impact of the swirling flow on the cooling performance of the system (Fig. 2.2).

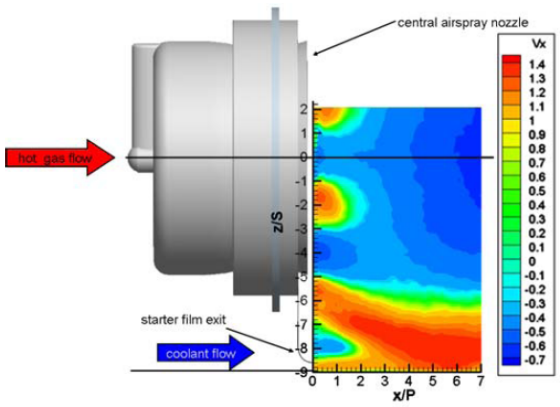

Figure 2.2: Axial velocity distribution of a LDI injector at isothermal condition [25]

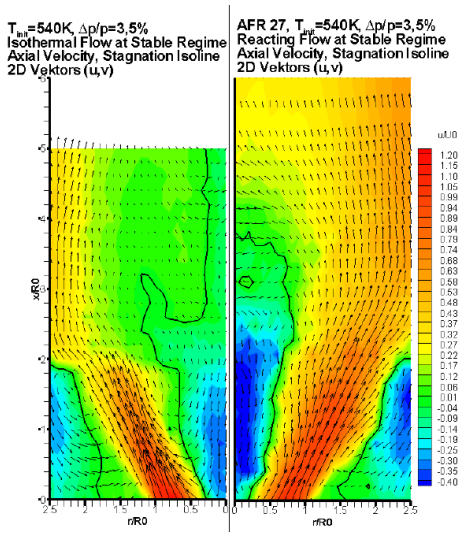

Figure 2.3: Isothermal (left) and stable reacting flow field (right) of a PERM injector [15]

Marinov et al. [15] and Kern et al. [28] investigated the flow field generated by a PERM injector in a cylindrical combustion chamber by means of LDA measurements and numerical simulations (Fig. 2.3). Two lean operation conditions were analysed, one in stable regime and the other very close to the weak extinction limit: a similar flow pattern was observed for the two flame regimes, however in the case of stable flame Inner Recirculation Zone (IRZ) was shorter. In addition, it has been shown that only highly sophisticated models as LES are capable to correctly predict the mean flow field and to identify the high frequent and dominant coherent structure of the precessing vortex core.

The flow field generated by an innovative Ultra Low NOx injector was experimentally investigated thanks to Particle Image Velocimetry and Hot Wire Anemometry by Berrino et al. [29]. A large reverse flow region, capable to provide a good stabilization to the flame, was detected; the interfaces between this region and the high velocity jet exiting from the swirler were identified as the most suitable for fuel injection, due to the presence of turbulent tangential stresses and vortical structures which promote the fuel atomization and mixing. Andreini et al. [30] carried out a CFD analysis

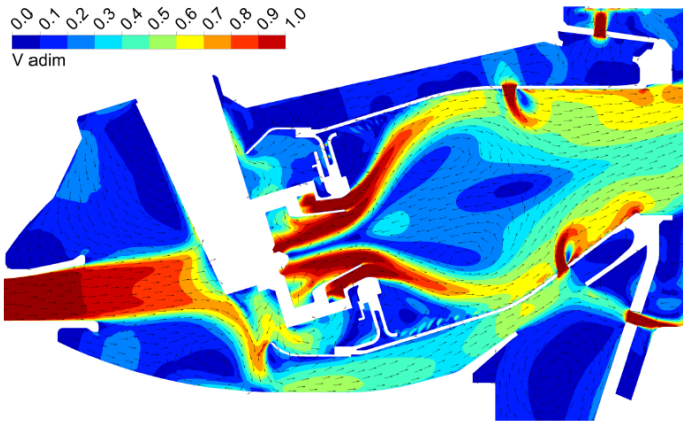

Figure 2.4: Flow field within a combustor equipped with a PERM injection system [30]

on a test case consists of a prototype of a single annular lean-burn combustor, equipped with a PERM injector. Velocity field on the meridional plane highlighted an almost entirely occupation of the combustion chamber by the recirculation zone generated by the swirler (Fig. 2.4).

2.2 Combustor liner cooling

Although primary attention to cooling problems within the engine was traditionally focused on the high pressure turbine blades, nowadays there is a need to view combustor liner cooling as a technical issue of equal importance, in order to meet targeted performance goals and durability improvements. Conventional methods employed forced convection inside the annulus to remove heat from the liner. However, the high temperatures and thermal gradients that burden on this component make the forced convection alone not suitable for modern combustion chambers cooling.

The actual most widely used technique to control the liner temperature is film cooling. Purpose is to create a protective cold layer between hot gasses and liner walls using the pressurized air that does not participate directly to combustion process. Several arrangements were proposed and investigated

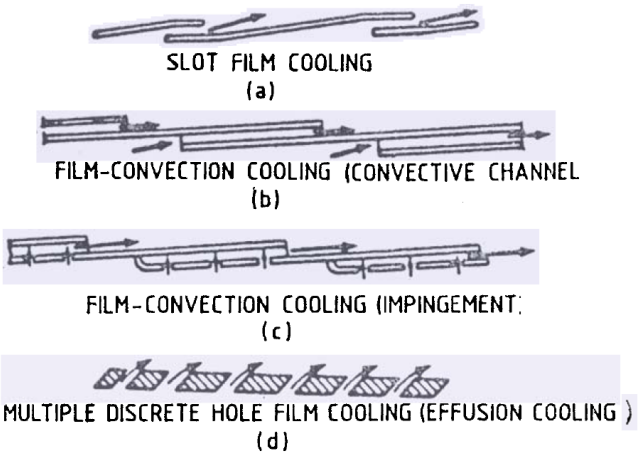

Figure 2.5: Combustor liner cooling arrangements [31]

during years, bi-dimensional slot injection (Fig. 2.5a) has represented a basic choice thanks to its simplicity and low weight, founding widespread application in both industrial and aircraft gas turbines. The thin coolant layer produced by the slot is gradually destroyed downstream of the injection point by the turbulent mixing with hot gas flow, so the normal practice is to repeat a succession of injection sources along the liner axial length.

The proven benefit of exploiting the heat sink effect available in the cooling air for convection cooling prior to ejecting it for film cooling [32] has led to the development of liner schemes based on a film-convection cooling approach (Fig. 2.5b). A significant reduction in coolant mass flow rates ($20\% - 25\%$) are achieved with respect to the prior arrangement [33]. Furthermore more uniform metal temperatures and higher mechanical robustness are provided. Principal disadvantages of this design are heavier construction and increased manufacturing complexity.

Impingement cooling systems (Fig. 2.5c) guarantee a further intensification of the convective heat transfer on the cold side. Cooling air is shaped into multiple jets directed towards the liner inner surface, before to merge to form an annular sheet operating in a conventional film cooling mode. A double-wall construction is required, leading to some penalties in terms of weight and cost.

Despite the cooling methods proposed above have the ability to create an effective thin cold layer at liner wall, the requirement of large amounts of coolant is not compatible with the lean combustor architecture. Therefore the demand of developing more performing cooling systems is already mandatory for more powerful and low emissions engines. In this scenario one of the more promising technologies has been identified in effusion cooling systems (Fig. 2.5d).

2.2.1 Effusion cooling

Effusion cooling can be simultaneously view as an evolution of discrete coolant injection methods above mentioned and a simpler approach to a practical form of transpiration cooling, that represent the most efficient arrangement based on porous and no-metallic materials, but whose employment on gas turbines is currently not feasible due to reliability issues. Effusion cooling consists of an array of closely spaced discrete film cooling holes, generally manufactured by means of laser drilling technique, distributed on the whole liner surface (Fig. 2.6). Generally perforation has small injection angles (α), relative to the nominal main flow direction, with usual values of about $30deg$. Thanks to manufacturing technology advancement, extremely slanted angles (up to $10deg$) can be achieved, but significant increasing in fabrication costs are demanded.

The intrinsic features of this cooling technique determine several favourable

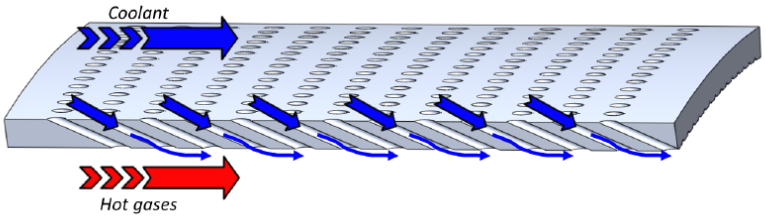

Figure 2.6: Effusion cooled liner

characteristics:

- Homogeneous film cooling protection is achieved thanks to the dense array of holes and is ensured, along the axial direction of the combustor, by the continuous coolant injection that gradually increases row by row due to the film superposition effect.
- Quite high length-to-diameter ratio (l/d) involves a significant heat sink effect, which permits to lower significantly the metal temperature, due to the heat removed by the forced convection of the coolant flowing through each holes [34].
- The mass bleeding on the cold side due to the intensive coolant extraction provides a significant increase in heat transfer coefficient, contributing deeply to balance the thermal load acting on the liner

Despite effusion cooling generates an insulating coolant layer not excellent as 2D slot system (at least in the first part of the liner, where superposition is not fully developed) and entails larger manufacturing costs, this technology allows to meet the requirements of lean combustion systems, overcoming limitations connected to the reduced air flow rate available for liner cooling

Figure 2.7: Combustor prototype of European Project NEWAC [35]

purpose. Furthermore a more homogeneous cooling of the liner is achieved due to the small holes uniformly distributed all over the wall surface, avoiding the arising of dangerous thermal gradients that could generate cracks formation on the liner.

As already stated, modern, low emission systems are prone to thermoacoustic instabilities since the heat release process is more sensitive to fluctuations when operating at lean conditions. Regarding this concern, another attractive feature of effusion cooled liner is the capability of providing an acoustic instabilities damping. Abatement mechanism is based on the generation and the diffusion of vorticity near the hole lip, that allows to transfer the acoustic energy to the flow field field as kinetic energy and then to dissipate instabilities through the action of shear stresses [36], [37].

In Fig. 2.7 is reported a picture of a prototype of a combustion chamber equipped with an effusion scheme developed within the European Integrated Project NEWAC.

Many parameters have been introduced in literature to characterize effusion cooling schemes. Main dimensional characteristics are sketched in Fig. 2.8 and are represented by the hole diameter (D), the inclination angle (α), the hole length (L) and the holes pitch (S_x for the streamwise pitch and S_y for the spanwise pitch). Perforation array can be manufactured in a staggered arrangement, as illustrated, or with holes positioned in an in-line

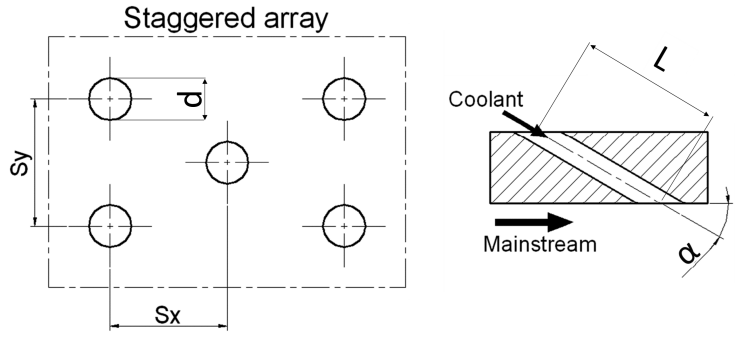

Figure 2.8: Main geometrical parameters for an effusion arrangement

configuration. Holes can also present a different orientation with respect the main flow direction, in this case is introduced the compound angle parameter β. A supplementary geometrical feature, usually employed in gas turbine blades cooling, can be achieved by means of a modification of the hole exit section, obtaining so called fan-shaped holes. Despite the advantages achievable with such kind of geometrical arrangement, its adoption for the huge amount of effusion holes expected on a liner would introduce a significant increase in manufacturing cost.

Film cooling method also depends on special combinations of parameters that govern the interaction between main and coolant flows. This set of non-dimensional quantities includes the velocity ratio (VR), the density ratio (DR), the blowing ratio (BR) and the momentum ratio (MR).

$$VR = \frac{U_{cool}}{U_{main}} \tag{2.1}$$

$$DR = \frac{\rho_{cool}}{\rho_{main}} \tag{2.2}$$

$$BR = \frac{(\rho U)_{cool}}{(\rho U)_{main}} \tag{2.3}$$

$$MR = \frac{(\rho U^2)_{cool}}{(\rho U^2)_{main}} \tag{2.4}$$

where the subscript *main* refers to mainstream hot gases quantities, while *cool* indicates the conditions of the air exiting from the cooling system.

In modern aero-engine combustors the working conditions are highly variable, both in terms of different regimes of the engine, characterized by several

levels of pressure, temperature and mass flow rate, and also within the own combustion chamber, with portions of the liner which face various heat loads and flow velocities near wall. This aspect must be taken into important consideration for a reliable and efficient design. Thermal performances of the cooling scheme are affected by some fluid dynamics parameters, first of all it's worth mentioning the mainstream heat transfer coefficient (HTC_{main}) which appears in the expression of the heat flux from a film cooled surface provided by Goldstein [38]:

$$\dot{q}_{conv} = HTC_{main} \cdot (T_w - T_{aw}) \tag{2.5}$$

$\dot{q}_{conv}$ represents the convective heat flux, while the temperature difference is evaluated between the wall temperature T_w and the adiabatic wall temperature T_{aw}, that represents the surface temperature obtainable in the extreme case of perfectly insulated (adiabatic) surface, with heat flux equal to zero. As pointed out by Eckert [39], in case of injection at the free-stream temperature, no differences subsist between adiabatic wall, free-stream and jet temperature: hence heat transfer coefficient may be evaluated once free-stream and wall temperatures are known. Adiabatic wall temperature is present also in another non-dimensional parameter of primary importance, this is adiabatic film cooling effectiveness η_{ad} and is defined as:

$$\eta_{ad} = \frac{T_{main} - T_{aw}}{T_{main} - T_{cool}} \tag{2.6}$$

Extreme values of $\eta_{ad} = 0$ and $\eta_{ad} = 1$ point out respectively the absence of surface film cooling ($T_{main} = T_{aw}$) and the perfect situation of complete wall covering ($T_{cool} = T_{aw}$). The above mentioned parameters govern the two mechanisms appointed to lower the metal temperature and can be coupled to analyse the performance of cooling systems leading to the definition of the Net Heat Flux Reduction ($NHFR$) proposed by Sen et al. [40]:

$$NHFR = 1 - \frac{\dot{q}}{\dot{q}_0} = 1 - \frac{HTC_{main}}{HTC_0}\left(1 - \eta_{ad} \cdot \theta\right) \tag{2.7}$$

In this equation HTC_{main} is compared to HTC_0, this is the heat transfer coefficient evaluated without film cooling. The terms θ is a non-dimensional temperature calculated as follows:

$$\theta = \frac{T_{main} - T_{cool}}{T_{main} - T_w} \tag{2.8}$$

Goal of the cooling systems is obviously to increase the $NHFR$ as much as possible. It is worth to notice that, in presence of high radiation the $NFHR$ parameter is not fully representative of the reduction of heat load to the liner surface. Furthermore, as stated by Kelly and Bogard [41], the increased mixing within the boundary layer due to coolant injection causes a substantial increase in the mainstream heat transfer coefficient, therefore η_{ad} should be high enough to compensate for this HTC augmentation, otherwise the heat transfer reduction is not achieved.

$NHFR$ definition does not explicitly take into account the heat sink effect, which instead plays an important role in effusion cooling technique, due to generally high holes length to diameter ratios. To overcome this issue, the overall effectiveness parameter η_{ov} has been introduced in literature:

$$\eta_{ov} = \frac{T_{main} - T_w}{T_{main} - T_{cool}} \tag{2.9}$$

As it is possible to notice, the definition considers the actual wall temperature, hence taking into account all the contributions to liner temperature lowering.

2.3 Liner cooling literature review

For full coverage film cooling applications, the analysis and the characterization of the liner heat transfer represent fundamental issues in order to optimize the entire cooling system performance, and a main purpose for several works performed since the 70's.

Metzger et al. [42] were among the firsts to study the variation of heat transfer coefficient for full-coverage film cooling scheme with normal holes, both for in-line and staggered arrays, finding a significant increase (up to $20 - 25\%$) compared to values obtained with no injection. Mayle and Camarata [43] studied the effects of hole spacing and blowing ratio on heat transfer for a staggered array composed of holes inclined at $\alpha = 30deg$ and compounded at $\beta = 45deg$. Within the hole pattern, the Stanton number increases as hole pitch-to-diameter ratio decreases and the mass flux ratio increases. Downstream of the hole pattern, the Stanton number decreases rapidly tending to the flat plate behaviour.

Crawford et al. [44] experimentally determined Stanton number for different effusion cooling systems. The work aim was to estimate, for each geometry, the effects on surface heat flux of injection blowing ratio, injection temperature ratio, and upstream initial conditions. In a companion paper [45], same authors proposed one of the first approaches based on the numerical modelling of film cooling injection in a 2D boundary layer code.

An outstanding effort was carried out by University of Leeds researchers in the early 1990's, Andrews et al. [46, 47, 48] experimentally investigated the impact on overall cooling effectiveness of typical system parameters (number of holes, pressure losses through the injection plate, holes length, injection angle) for a wide range of practical engine conditions. Ekkad et al. [49, 50] measured effectiveness and heat transfer coefficient distributions over a flat surface with one row of injection holes inclined streamwise at 35° for several blowing ratios and compound angles. Tests were conducted taking into account effects of density ratio between the main hot gases and the cooling flows, using carbon dioxide as a coolant.

An extremely slanted holes configuration was studied by Martiny et al. [51] employing IR thermography for adiabatic effectiveness measurements and Schlieren photography for flow visualization. They noticed that in the starting region of a cooling film, with a blowing ratio equal to 0.5, coolant jets remain attached to the wall and for higher values of blowing parameter a closed cooling film is prevented by the jets lifting-off from the surface. Nevertheless, even in cases of complete penetration, cooling benefits, in terms

of adiabatic effectiveness, are still present and they are ascribable to the massive coolant injection, which increases row by row and reduces main flow temperature in the mixing zone. The same test case was faced also developing a mathematical model able to detect the dependencies of dimensionless quantities on the overall thermal effectiveness [52].

A parametric study of temperature distribution on effusion-cooled plates under typical combustion chambers conditions was performed using infra-red thermography by Gustafsson and Johansson [34]. Among several parameters investigated, the effect of reducing the injection angle resulted in moreattached jets, especially for small amounts of cooling air, and marginally lowers the wall temperature.

Martinez-Botas and Yuen [53] used an efficient steady-state wide band liquid crystal technique to study the film cooling performance of a variety of geometries in a flat plate. Exploiting all the capabilities of this measurement approach, the most effective film cooling was achieved at a value of blowing ratio close to 0.5 and for near unity density ratio. Among the three tested angles of injection ($\alpha = 30deg, 60deg, 90deg$), the more inclined geometry provided consistently higher effectiveness for most of the blowing ratios tested without significant trade off in high levels of HTC_{main}/HTC_0. An experimental and numerical investigation of adiabatic film cooling effectiveness was conducted by [54] on four full-coverage inclined multi-hole walls with different arrangements. The hole geometrical patterns and the test conditions were chosen to be representative of film cooling designs for modern aero-engine combustor liners and an heat-mass transfer analogy method was employed for experimental measurements.

Scrittore et al. [55] measured velocity profiles and adiabatic effectiveness of a full coverage scheme with blowing ratios varying from 3.2 to 5.0, finding the attainment of a fully developed effectiveness region at the 15th row and a very low effect of blowing ratio on cooling performance. They also observed a fundamental independence of penetration height for the cooling hole rows on the momentum flux ratio for the range that was considered at the fully-developed condition. More recently, Ligrani et al. [56] presented film effectiveness and heat transfer results for full coverage film cooling con-

figurations with streamwise pressure gradient; they studied the effect of the blowing ratio and the influence of dense and sparse hole arrays on the thermal effectiveness.

Kakade et al. [57] reported a thorough analysis of typical effusion-cooling performance at a range of combustor relevant free-stream conditions. They observed that for high turbulence conditions, although the levels of heat transfer augmentation are higher, the impact is generally similar to the low free-stream turbulence states: relatively small changes in the heat transfer augmentation when the flow is attached to the surface and significant increase when the injected coolant is detached from the surface (Fig. 2.9).

More recently, an experimental investigation was set up by Andreini et al. [58] for the evaluation of thermal performance, in terms of overall and adi-

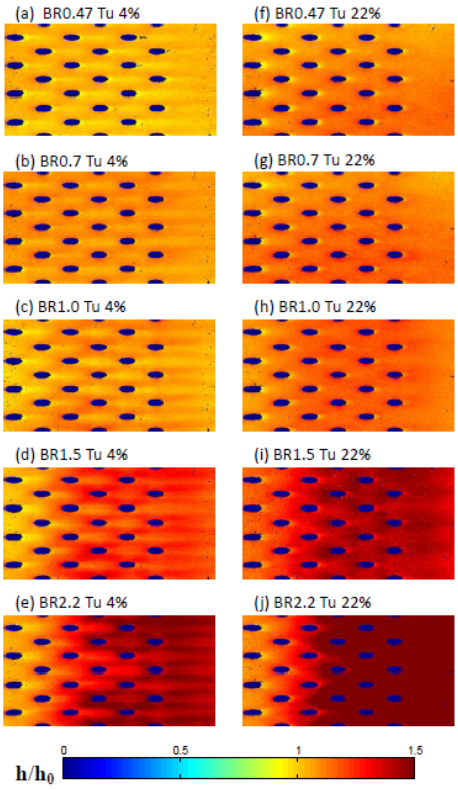

Figure 2.9: Measured normalised heat transfer coefficient for low density ratio injection conditions [57]

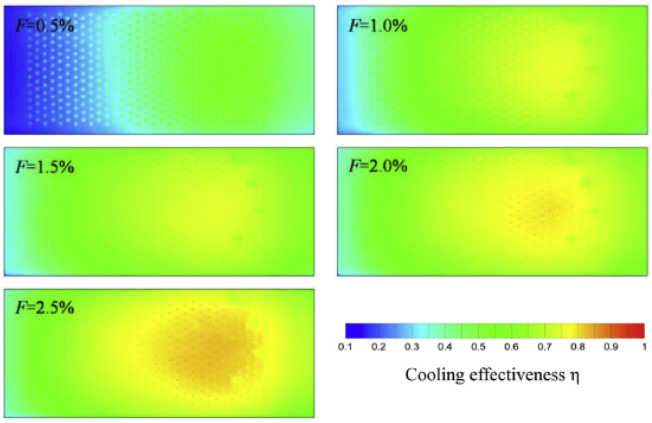

Figure 2.10: Cooling effectiveness distributions varying the Blowing Ratio F [59]

abatic effectiveness, of several multi-perforated planar plates. Results highlighted the impact of fluid dynamic parameters and geometrical features; moreover, a correlative analysis was performed to solve the augmentation of hot side heat transfer coefficient and to compute the effect of a gas side radiation on thermal behaviour.

An interesting work by Huang et al. [59] dealt with perforated flat plates with orthogonal cooling holes arranged in a staggered pattern. External surface temperature distributions were acquired for two different hole diameters using an IR thermal imaging system, varying the Blowing Ratio. The obtained cooling efficiencies, reported in Fig. 2.10, were compared with former transpiration cooling results, highlighting similar performance for the high porosity configuration. Two techniques for qualitatively assessing relative adiabatic film cooling performance of different combustor wall cooling concepts were presented by Krawciw et al. [60]: an experimental campaign was carried out employing the oxygen quenched luminescent properties of Pressure Sensitive Paint, and a RANS based CFD approach was used to predict film effectiveness with minimised computational cost.

PSP technique was also adopted by [61] for adiabatic film effectiveness

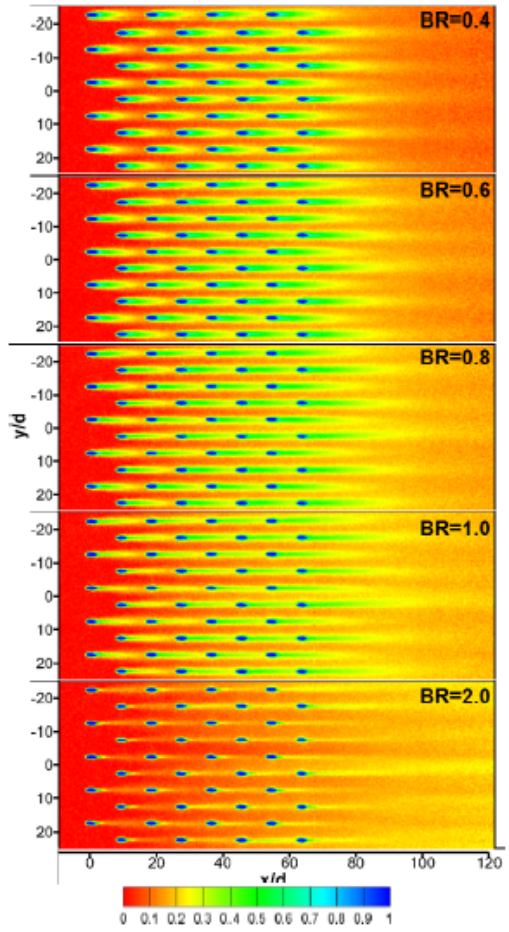

Figure 2.11: Film effectiveness maps [61]

measurement on a multi-perforated flat plate with $20deg$ holes inclination angle. Results, reported by means of bi-dimensional maps in Fig. 2.11, pointed out that film effectiveness increases with enhancing BR for $BR < 0.8$ and decreases with increasing BR for $BR > 0.8$.

With the development of innovative addictive manufacturing technologies several studies investigated the applicability of methods as Direct Metal Laser Sintering (DMLS) for combustor film cooling applications. Jackowski et al. [62] investigated a set of six combustor liner tile specimens; besides well known geometries like cylindrical, fan-shaped, laidback or a combination of those, two geometries with bent cooling holes, unobtainable with conven-

tional manufacturing processes, were studied. The cooling performance were determined by comparing the total cooling effectiveness for a given pressure difference across the combustor liner tiles. The results showed a tremendous improvement of total cooling effectiveness for one bent cooling hole geometry compared to traditional concepts.

The effects on film cooling effectiveness of surface and hole interior roughness due to DMLS manufacturing were investigated by Vinton et al. [63] by means of a steady state, PSP technique. They observed that large portions of the film cooling holes were blocked by the roughness created from the DMLS technique, leading to a detrimental impact on film covering distributions.

The majority of scientific works on effusion cooling systems deals with the measurements of thermal behaviour with simplified flow conditions on the hot side; on the other hand very few works are related to the effusion cooling performance under realistic flow field conditions. Nevertheless, the swirled flow in a combustion chamber has a deep impact on the heat transfer coefficient distribution, especially considering the combustor chamber equipped with lean-burn injection systems.

In some studies, a backward facing step was employed to simulate the effect of typical corner recirculation zone [64, 65, 66]; recently, to increase the readiness level of the experimental results, several heat transfer measurements have been performed in more realistic environments: Patil et al. [67, 68] carried out experimental and numerical investigations on liner wall convective heat transfer coefficient in an annular and can combustor test rigs without cooling system, they employed a swirler which generates a flow field representative of a real engine injector. The experimental analysis was carried out using air at ambient conditions and measuring the temperature of heated flat liner wall by means of an Infra-Red camera. The interaction of the swirled flow with the different surface curvature (can liner, annular convex and concave liners) results in a slightly larger region of peak heat transfer on the concave liner wall. It is highlighted that, as the Reynolds number increases, the Nusselt number augmentation reduces on the walls.

A pioneering work on cooling performance of effusion systems under

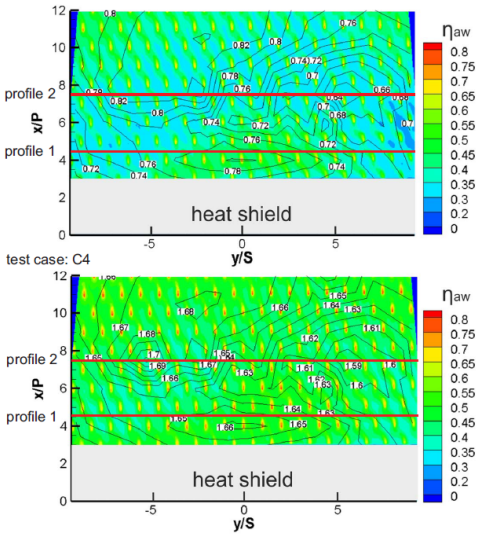

Figure 2.12: Cooling effectiveness (contour) and local blowing ratios (isolines) varying the pressure drop across effusion liner (top: $\Delta P/P_{eff} = 1\%$ and bottom $\Delta P/P_{eff} = 3\%$. [27]

realistic swirled flows has been recently reported by Wurm et al. [25, 27, 69]: developing a three sector scaled facility, they studied the flow field generated by the injectors and their interaction with the cooling arrangement; moreover, the Infra-Red camera technique was used to perform film effectiveness measurements and to estimate a posteriori the efficiency of the cooling system. As illustrated in Fig. 2.12, results showed that better adiabatic effectiveness can be achieved increasing the pressure drop across the multi-perforated plate.

Andreini et al. [13, 70, 71] carried out an experimental survey aimed at measuring adiabatic effectiveness and heat transfer coefficient in a planar three sector rig operated with representative swirl flow field; a cooling scheme based on slot cooling and effusion was considered. In both studies dealing with full-coverage film cooling, a specific configuration of multi-perforated liner was used, without a systematic deepening about the role of geometric parameters on overall thermal effectiveness.

All these studies deal with combustor cooling systems exposed to realistic chamber flow field, however experiments are conducted at atmospheric

and non-reacting conditions, therefore the effects of hot highly turbulent and swirling gas flows on the cooling film and thus on the cooling effectiveness can not be completely covered by these investigations. To the author's knowledge, in only very few works, focused to liner cooling study, the hot gas flow is represented by actual combustion products, with velocity and temperature distributions typical of real gas turbine combustors. Behrendt et al. [72] provided a systematic and quantitative characterization of the influence of the cooling air properties and the combustor pressure on the cooling effectiveness of different advanced cooling configurations. More recently, employing the same High Pressure Cooling Rig, Jackowski et al. [62] tested at realistic aero-engine conditions an innovative cooling configuration manufactured with DMLS process.

A scaled annular combustor equipped with three axial swirlers was tested at reactive conditions by Ji et al. [73]. The cooling scheme for the liner is an effusion perforation with 7 rows of cooling holes with a $90deg$ inclination angle and an in-line layout. Overall cooling effectiveness was evaluated measuring the temperature on the liners cold side by means of IR thermography. A better cooling protection was observed on the outer liner with minimum values detected for an unit equivalence ratio.

Another aspect of effusion cooling where a moderate lack of knowledge is evident from the analysis of the technical literature is represented by the thermal behaviour of the multi-perforated liner on the feeding cold side. Nevertheless, Gerendas et al. [74] pointed out that in case of effusion cooling, up to 30% of the heat extracted from the liner is due to cold side convective cooling. This evidence is explained by a heat transfer augmentation at the hole entrance due to the reduction in boundary layer thickness related to the coolant bleeding and the acceleration of the coolant around of the holes. Understanding and predicting the effects of the coolant extraction on the cold-side convective heat load is hence fundamental to design more effective cooling schemes and to improve combustors durability.

In open literature several works highlighted a close relationship between the coolant bleed rate and the heat transfer augmentation in the holes entrance region. Sparrow and Kemink [75] performed experiments to study

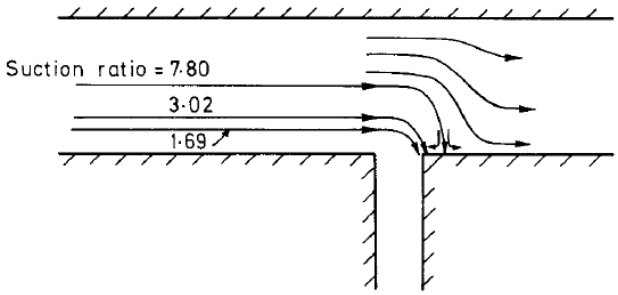

Figure 2.13: View of dividing streamlines approaching orthogonal extraction [76]

how fluid withdrawal at a branch point in a tube affects the heat transfer of the main line flow downstream of the extraction. Varying the main channel Reynolds number, they highlighted that heat transfer coefficients in the thermal entrance region are much higher than those for a conventional axisymmetric flow.

Byerley et al. [76] and Byerley [77] collected the results of an extensive experimental campaign aimed at analysing the heat transfer enhancement factor EF varying the suction ratio SR (i.e. the ratio between velocity within the hole and within the feeding channel) from 0 to 8, the hole inclination angle (film cooling holes angled at $30deg$, $90deg$, and $150deg$ to the oncoming flow), the main duct Reynolds number and the upstream temperature and velocity profiles. Smoke visualization technique allowed to show the mainstream flow behaviour as SR was varied, dividing streamline, upstream of the hole, moved from the duct wall surface towards the duct centreline as the suction ratio was increased (Fig. 2.13). Furthermore, the stagnation point was observed to move downstream with the formation of reverse flow in the region immediately downstream of the hole. This mechanism contributes to the attainment of average heat transfer enhancement factors up to six downstream of the extraction. Also results by Cho [78] revealed an increase in heat transfer in the same region, in particular the mass transfer coefficient for the surface of a film-cooled plate was found to be three to five times higher than for a fully developed duct flow.

Ieronymidis et al. [79] conducted a detailed analysis of the heat trans-

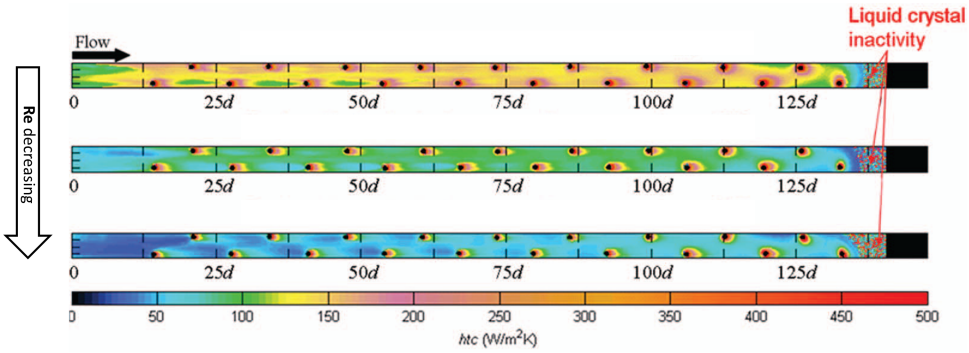

Figure 2.14: Passage heat transfer coefficient maps varying Reynolds number [79]

fer within a cooling passage equipped with 19 extraction holes by means of experiments. As showed in (Fig. 2.14), the authors confirm heat transfer enhancements downstream of the extraction holes. Furthermore, they also pointed out that the spanwise averaged heat transfer coefficient is roughly constant in the central part of the array and it shows a decreasing trend approaching the cooling passage end cap. In their contribution, Cottin et al. [80] numerically investigate the aero-thermal field of effusion cooling plates, suggesting an expression to correlate the cold side heat transfer coefficient augmentation to the local suction ratio.

Andreini et al. [81] carried out a numerical activity aimed at investigating the phenomenology of the heat transfer at the entrance of film cooling holes. Steady state RANS simulations were performed, modelling turbulence by means of the $k-\omega$ SST (Shear Stress Transport) model. Methodology was validated using the well-known Byerley's test case [77] and results showed very good agreement with experimental data. This work set the basis for the study performed by Da Soghe et al. [82] which led to the development of an empirical correlation for the prediction of the cold side heat transfer coefficient enhancement factor EF. Proposed expression supplied EF related to each extraction hole as a function of the pressure ratio and the effusion plate porosity factor σ.

2.4 Thesis motivations and outline

Among advanced liner cooling strategies, full coverage effusion cooling has imposed itself as one of the most promising answer to the request for continuous performance improvement imposed by the development trend of novel core engines. In this context, a full comprehension of effusion cooling behaviour under realistic flow conditions is absolutely mandatory, even more so for lean-burn combustor technologies which involve highly swirling and expanding flows generated by the injectors. At the same time, deepening the knowledge about the influence of parameters affecting the liner thermal management is required for a proper optimization of the cooling arrangement.

Available literature identified the effusion holes inclination angle as one of the most relevant feature of the cooling system, pointing out a remarkable impact on both the two fundamental mechanisms of temperature lowering (i.e. film covering and heat sink effect) provided by the perforation. For this reason, the present experimental work has focused the attention on several differently inclined effusion configurations subjected to a realistic swirled mainstream flow field. A thorough characterization of the system was achieved through the exploitation of three different experimental techniques on a isothermal test rig.

A further heat transfer contribution to liner total cooling effectiveness is represented by cold side convective heat removal. This aspect is scarcely considered in the open literature, despite the considerable role played in the thermal balance of combustor walls. Therefore, a dedicated analysis is addressed to the investigation of the heat transfer coefficient distribution, due to holes coolant extraction, on an inclined effusion geometry.

As already stated, innovative combustion techniques in aero engines require highly effective cooling schemes of combustor walls; however the freedom in the design of advanced liner configurations is limited due to manufacturing capability. Therefore it's not surprising that emerging additive manufacturing methods have attracted the interest of aero engine indus-

tries, thanks to virtually unlimited design and reduced costs and procurement times. With the aim of identifying appropriate criteria to develop components manufactured with rapid prototyping technique and of validating at TRL 5-6 the potentiality of such technology, a new test rig is designed and commissioned. The module is a linear sector combustor, equipped with three PERM fuel injectors and two air cooled effusion liners, all manufactured by Direct Metal Laser Sintering (DMLS). Results from a preliminary experimental survey, aimed to verify rig and test cell apparatus commissioning, are reported. During test, several engine conditions are explored, varying the fuel air ratio and the split between main and pilot combustible.

Regarding this dissertation outline, the previous and the present chapters introduced the research area of this work: in Chapter 1 low emission aero-engines and lean burn technology are initially presented; the PERM injection system, used as the reference geometry in the experimental activity developed in this research, is also described. Chapter 2 aims to clarify the phenomena that characterize the heat transfer in lean combustors. The liner cooling technologies used to manage the thermal loads are introduced, with a particular focus on effusion cooling approach. Relevant past studies on this topic are reported.

In forthcoming Chapter 3 the attention is focused on the measurement techniques employed during the experimental activity at isothermal conditions. Particle Image Velocimetry, TLC steady state technique and Pressure Sensitive Paint approach are described in detail and a measurement uncertainties analysis is conducted. Chapter 4 shows the apparatuses for the experimental investigations performed at ambient conditions on two distinct, but related, test rigs: the Three Sector Test Rig (TSTR) and the Cold Side Test Rig (CSTR). Results from these campaigns are presented in Chapter 5 by means of bi-dimensional maps and laterally averaged distributions. Great relevance is addressed to the comparison between different effusion geometries characterized by varying the holes inclination angle.

In the final part of the work, attention is moved to test performed at reactive conditions. Chapter 6 introduces the VALIDATOR test rig, pointing

out the main features of the apparatus and describing the rig commissioning; results in terms of discrete temperature values and flame snapshots are presented.

Finally in the last chapter, a summary of the main achievements of this research is given together with conclusions and recommendations for future research.

Chapter 3

Measurement Techniques

Contents

3.1	**Flow field by particle image velocimetry**	**44**
3.2	**TLC steady state technique for HTC tests** . . .	**49**
3.2.1	Experimental procedure and data post-processing .	51
3.3	**PSP for film effectiveness measurements**	**58**
3.4	**Measurement uncertainty**	**65**

Objective of the present chapter is to introduce the measurement techniques and the data reduction procedures employed in this study on the three sector test rig. The extensive experimental survey aimed to completely characterized an effusion cooling system under realistic flow conditions and is organized through the development of three distinct measurement approaches:

- A standard 2D Particle Image Velocimetry (PIV) is employed to investigate the PERM injector flow field and its interactions with the cooling system flows near the liner wall.

- A steady state technique, using Thermochromic Liquid Crystals (TLC) paint, coupled with thermal FEM simulations, is exploited to estimate the heat transfer coefficient both on the hot and on the cold side of the liner.

- Pressure Sensitive Paints (PSP) are used to obtain detailed adiabatic effectiveness maps in order to analyse the impact of the swirling main-

stream jets on the system cooling performance and to investigate the effects related to the holes injection angle.

3.1 Flow field by particle image velocimetry

In this section the main features of the PIV technique will be briefly described to support a general understanding of basic principles; an exhaustive overview on this technique is provided in the work of Raffel et al. [83].

PIV technique is designated for achieving instantaneous whole-field velocities and is based on the insertion inside the test case flow of seeding particles, able to follow the mean flow field. As sketched in Fig. 3.1, the particles are illuminated through a laser sheet and their positions are caught by a CCD (Charge Coupled Device) camera within a known time interval between two laser pulses. The laser system used to illuminate the seeding particles must not generate chromatic aberrations and is able to supply a monochromatic light with high density of energy; a set of optic lens are used to generate the light sheet while a mirror can be used to deviate the laser beam.

In order to evaluate the particle movements, the images acquired by the

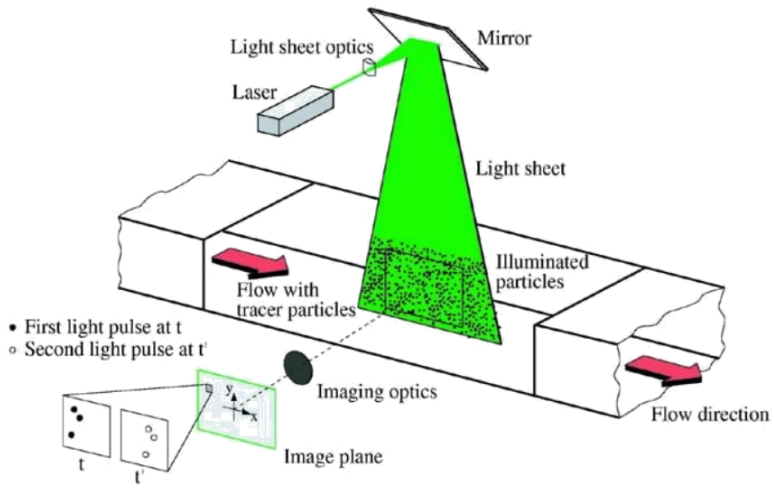

Figure 3.1: Experimental set-up for PIV measurements

camera are divided in different interrogation areas. Assuming an homogeneous movement of particles inside each area, a statistic approach based on an adaptive correlation method is exploited to compute a vector associated to the particle movement. Moreover, the velocity vector on the laser plane is directly computed by the movement vector knowing the time delay between the pair of images and the so called "scale factor" to convert CCD coordinates into space coordinates.

In contrast with conventional techniques for the measurement of flow velocities, which generally employees probes as pressure tubes, PIV is a totally non-intrusive technique, allowing its application in a broad range of experiments, as high speed flows with shocks or in boundary layers close to the wall. Wide PIV operability is established also in terms of measurable velocities, indeed with a single experimental set-up not theoretical limits are present if a correct time interval between the two laser pulses is selected.

Fluid-mechanical properties of the tracking particles must be accurately checked in relation to the nature of the flow under investigation to avoid significant discrepancies between the measured velocity, i.e. the particles velocity, and the actual velocity of the flow. A dimensionless number able to describe the capability of particles to follow the mean flow field is represented by the Stokes number:

$$Stk = \frac{\tau U}{d} \tag{3.1}$$

where τ is a characteristic time of particle drag phenomena, generally it is inversely proportional to the particle Reynolds number; U is the local drag velocity and d is the particle diameter. To follow faithfully the streamlines, the particles must have a limited value of Stokes number; from a practical point of view it can be stated that the condition $Stk < 0.1$ returns an acceptable flow tracing accuracy with errors below 1% [84]. In addition the particles must have good properties in terms of light reflection in order to be correctly detected during the test.

In the present work, olive oil particles with a mean diameter of about

$1\mu m$ are used as a seeding, atomization is carried out by means of a Laskin nozzle. Oil represents a favourable choice for ambient temperature applications, achieving some good peculiarities for a tracer: it is not toxic, it can stay in air at rest for a long time, and it does not change in size significantly under various conditions. Injection takes place upstream of the test rig entry mouth by means of a drilled pipe which extents as long as the height of the inlet of the test model in order to uniformly distribute the seeding particles.

Particle Image Velocimetry measurements are performed using a Dantec Dynamics PIV system, consisting of a $120mJ$ New Wave Solo Nd:YAG pulsed laser, operating with a wave-length of $532nm$, and a SpeedSense 4Mpixel camera operated at a frame rate of $10Hz$, in double frame mode. A narrow band optical filter is installed in front of the camera to ensure that only the reflected light from the particle is caught. All devices are controlled via the commercial software Dantec Dynamic Studio, that allows system synchronization, through a Programmable Timing Unit (PTU) used to provide the trigger signals to camera and laser system, and data post-processing.

The time delay between the two laser pulses is adjusted depending on an estimated local averaged velocity. It represents a key parameter and must be selected accurately during the commissioning of the experimental technique: if it is too long the recognized velocity can only be assimilated to a mean and not instantaneous value; on the other hand if it is too short there is not significant gain in the measurements (i.e. small variation of particle position) and the flow field cannot be reconstructed. The laser sheet thickness is set to about $1mm$, acting on the focus of the optical system, to keep the number of loss of pairs due to out of plane motion as low as possible. In addition, to avoid reflection of the laser light and hence to reduce the noise into the acquired images, all the components inside the test rig are painted with opaque black coating.

For each investigated condition, 480 image pairs (2560 x 1600 pixel) are acquired in order to reconstruct the mean flow field. First step of data post-processing is a background noise removal, the operation takes place through the subtraction from each acquired image of the averaged single pixel inten-

sity.

In PIV standard cross-correlation technique, each pair of images is divided in several interrogation areas and the 2D cross correlation is applied to find the particle movement. However particles in the time delay between the laser pulses can left the interrogation area, loss of these particle images is known as the *in-plane drop-out*, which reduces signal strength and, as a result, the number of successful vectors that can be obtained because the signal peak in correlation is lowered [24]. To overcome this issue an adaptive grid iterative method is used (Fig. 3.2). The fundamental principle of this approach is an iterative procedure based on the shift of the interrogation windows (i.e. the interrogation area is not locked in the space): from an initial guessed shift value, a shift is introduced from the first window (the interrogation area in the image frame from laser pulse one) to the second window (the interrogation area in the image from laser pulse two). The obtained movement vector calculated through standard cross correlation algorithm is used as a new estimate for the window shift in the second iteration. From the results of the previous iterative process a new run is made, but this time with a refinement of the size of the interrogation area. The employment of adaptive provide a two-ways benefit. First, the signal strength is raised due to the capture of the in-plane drop-out. Secondly, a refinement of the interrogation area is possible because an adaptive window offset is applied, again producing a successful signal and increasing the resolution of results.

The approach adopted in this work starts from a 128 x 128 pixel initial windows size, which is reduced in two steps to a 32 x 32 pixel final size; two iterations are chosen for each step. The resulting velocity field from

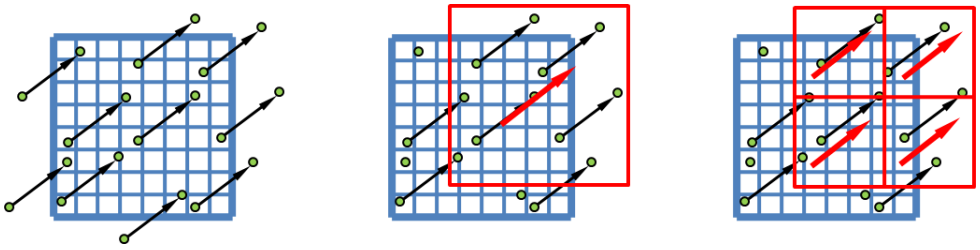

Figure 3.2: Adaptive correlation operating principle scheme

the adaptive correlation contains 159 x 99 vectors for each camera framing. These raw vector maps are validated and filtered using in succession two approaches: peak-height validation and moving-average validation. The first method validates or rejects individual vectors based on the values of the peak heights in the cross correlation plane; the criterion is to compare the highest peak with the second highest peak, if the ratio is greater than 1.2 the vector is not rejected. The second method validates or rejects vectors based on a comparison between neighbouring vectors. The rejected vectors are replaced by vectors estimated from surrounding values, assuming the continuity of the flow field.

3.2 TLC steady state technique for HTC tests

Heat transfer coefficient distributions are obtained by means of a steady state technique, employing TLC paint to measure the wall temperature from a heated surface. In gas turbine field, thermochromic liquid crystal coating has been widely used as an effective tool to visualize temperature distributions on solid surfaces. The capability of TLC of displaying different colors at different temperatures depends on selective reflection of certain wavelengths by the crystalline structure of the material. With respect to other heat transfer measurements technique, TLC offers some advantageous characteristics: it is a non intrusive method, achieving negligible interactions with the flow field, and it's able to provide continuous information on the whole test surface, overcoming typical limitations of methods based on discrete temperature measurement (i.e. thermocouples).

The liquid crystals used in this activity are wide band TLC 30C20W supplied by Hallcrest, such paint presents an activation range from about $32°C$ to $53°C$. The active substance of the liquid crystal is encapsulated into a polymer layer that provides protection against the environmental light that could damage it reducing the lifetime. The paint is blended with water and sprayed over the desired test surface using an airbrush, generally a black coating is used to provide the proper background for TLC. During tests, the investigated surface is heated up, when the temperature reaches the crystals activation temperature, the TLC start to reflect light from the long wavelength to the short wavelength: red is the first color to appear and as heating continues (i.e. the surface temperature increases), the color passes through the visible color spectrum to green and finally reaches blue. A further heating with temperature over $53°C$ leads to the TLC deactivation and color disappears.

Among possible TLC technique approaches used for temperature measurements, a steady-state, Hue-capturing method is adopted in this study. The hue angle is probably the most employed parameter as far as wide band crystals are considered; it is defined in a polar chromaticity space by the intensities of the red, green and blue primary colors and can be computed

as:

$$hue = \arctan \frac{\sqrt{3}(G - B)}{2R - G - B} \tag{3.2}$$

where R, G and B represents the red, green and blue channel values. The choice of hue as the color detector is due to the fact that this parameter is less sensitive to measurement conditions (e.g. light intensity) with respect to others, furthermore its dependency from temperature is monotonic inside the activation range of the TLC [85].

A robust TLC color-temperature response calibration is mandatory for high-accuracy measurements. When temperature is measured with the TLC, extra care has to be taken to fix all the conditions identical to the calibration to avoid the color variation problem due to the lighting/viewing arrangement. In this work, the illuminating apparatus consist of two $18W$ LED tubes ($5500K$ temperature color), which ensure an uniform illumination on the test surface and allows to keep both color temperature and light power constant. The TLC calibration has been conducted following the steady state gradient method [86] and an image of the set-up is reported in Fig. 3.3.

The calibration component is made by a $4.5mm$ thin aluminium rectangular plate, sprayed with black background paint and then TLC, with seven thermocouples embedded inside. From one side the plate is heated by an electric heater, while from the other it is cooled by air. The whole apparatus is placed into an insulating basis. A linear temperature gradient will appear on TLC surface: once steady conditions are reached, a digital camera

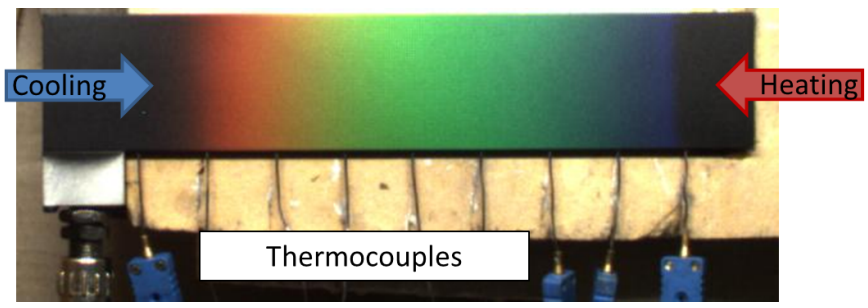

Figure 3.3: TLC calibration set-up

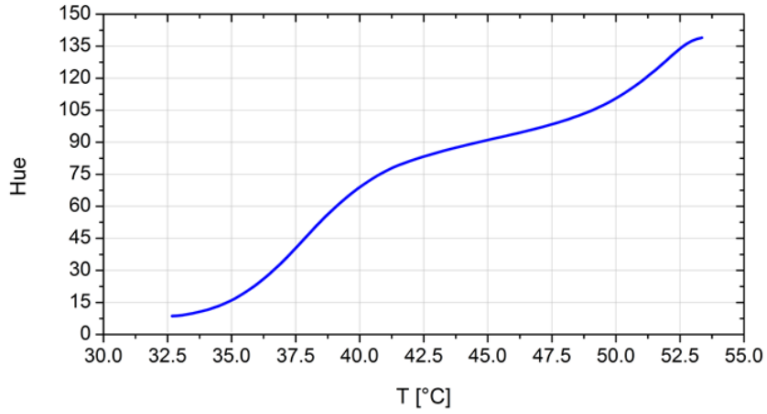

Figure 3.4: TLC calibration curve

(Sony XCD-SX90CR) is employed to capture the image (1280 x 960 pixel) of the TLC painted surface. This arrangement allows an entire TLC hue-temperature calibration curve to be computed from a single image, however, several tests have been carried out, in order to increase global accuracy. In Fig. 3.4 is depicted the obtained calibration curve employed to couple, pixel by pixel, the hue values to surface temperatures.

3.2.1 Experimental procedure and data post-processing

TLC steady state technique has been applied to evaluate heat transfer coefficient distributions on both the hot and the cold side of an effusion liner. Although measurements are performed on two distinct test rigs, the experimental set-up and the post-process procedures are maintained unaltered.

The effusion liner is manufactured in Arnite, a plastic material with low thermal conductivity and is covered with a thin heating foil made of Inconel 600 (sheet thickness: $0.0254mm$) replicating the same hole pattern of the multi-perforated plate. Surface heating is electrically supplied by two lateral copper bus bars, connected to a low voltage DC power supply which is current or voltage regulated during experiments, with the aim of obtaining

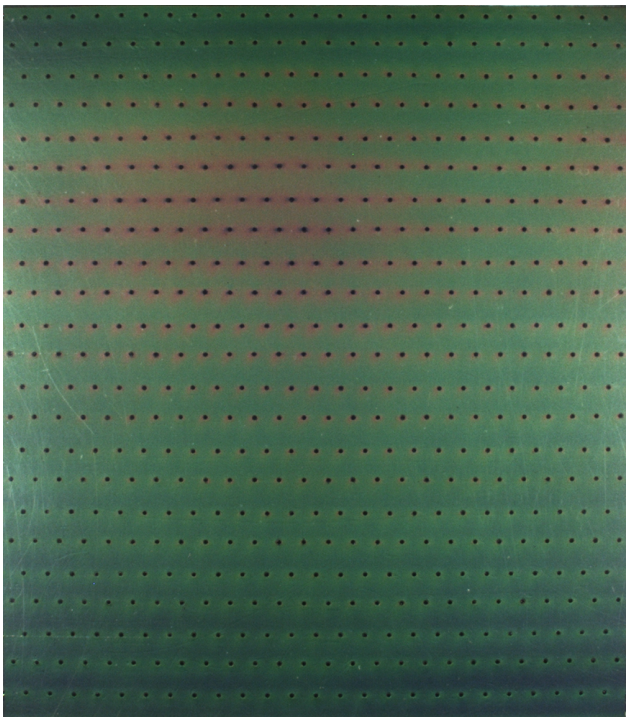

Figure 3.5: RGB map of the effusion plate

a liner temperature within the activation band of the selected TLC paint.

The acquisition time for one test point is around 1.5 hour: after setting the desired flow conditions, the voltage of the power supply is increased slowly in order to provide a smooth heating of the liner and a gradual activation of the thermochromic liquid crystals; finally the steady state conditions are awaited for about 45 minutes and when these are achieved the digital camera records a raw bitmap image of the painted surface on a PC (IEEE-1394 standard).

The post processing procedure of the acquired images is performed by a MatLab in-house code. The raw bitmap images are converted into color map exploiting *demosaic* Matlab command, in order to reconstruct full color images from the spatially under-sampled channels (Fig. 3.5). After that, the Red, Green and Blue value matrices, constituting the processed images, are converted into the single hue matrix, which leads straightforwardly to the temperature map through the use of the calibration curve.

The next step is the calculation of the heat transfer coefficient assessable through the expression:

$$HTC = \frac{\dot{q}_{conv}}{T_w - T_{aw}} \tag{3.3}$$

where the T_{aw} represents the surface temperature of a perfectly insulated wall. As the mainstream Mach number is low, recovery effects can be neglected and therefore the mainstream temperature (i.e. the annulus flow temperature for cold side investigation), measured with several thermocouples positioned in the test sections, is used as adiabatic wall temperature. T_w is the measured wall temperature recorded during the experiments by means of TLC; $\dot{q}_{conv}$ represents the heat flux exchanged by convection between the test plate and the main flow and can be computed as:

$$\dot{q}_{conv} = \dot{q}_{Joule} - \dot{q}_{loss} \tag{3.4}$$

Starting from previous equations, it's straightforward that for an accurate and reliable measurement of HTC is absolutely required a correct evaluation of the convective heat flux distribution . For an effusion cooled liner, two issues have to be taken into essential consideration:

- the holes on the heating element lead to a non uniform heat distribution by Joule effect ($\dot{q}_{Joule}$). As highlighted in the portion of the liner of Fig. 3.6 current density, and consequently the heat generated, is higher between each couple of holes in spanwise direction and lower before and after each hole in streamwise direction.
- a certain fraction of the heat generated by Joule effect is not exchanged by convection with the main flow, but it is lost by conduction through the Arnite® plate, by radiation from the heated liner to the surrounding walls and by forced convection from its back side and especially within the perforation (heat sink effect). The sum of these contributions is represented by the terms $\dot{q}_{loss}$ in Equation 3.4.

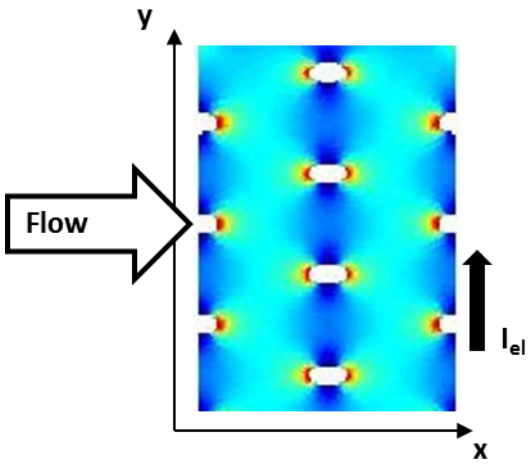

Figure 3.6: $\dot{q}_{Joule}$ distribution on a portion of the multi-perforated liner

For these reasons, a thermal-electric FEM simulation is performed using the commercial code Ansys Mechanical APDL 15® with the purpose of evaluating the net heat flux transferred from the surface to the annulus flow. For both hot side and cold side campaign, longitudinal portions of the liner plate are assumed as test cases, exploiting the symmetry of the problem and avoiding an excessive computational effort. The liner models are opportunely meshed, simulating both the thin Inconel sheet with thermal-electric elements and the ARNITE plate with thermal elements (Fig. 3.7). The properties of the material in terms of electric and thermal characteristics are set based on the data-sheets of the manufacturer. The Inconel 600 foil has a thermal conductivity of $14.9 W/(mK)$ and an electrical resistivity of $1.03 \mu\Omega \cdot m$. The thermal conductivity of the perforated test plate, made of Arnite, is measured by a certified research center: a value of $0.247 W/(mK)$ is reported for both the two temperature conditions ($20°C$ and $60°C$) examined.

Boundary conditions of FEM simulation are imposed as follow, reproducing typical conditions expected and evaluated during the experiments. Thermal loads:

- Holes: a correlative approach by means of proper expression for turbulent flow, taking into account holes length to diameter ratio, is applied

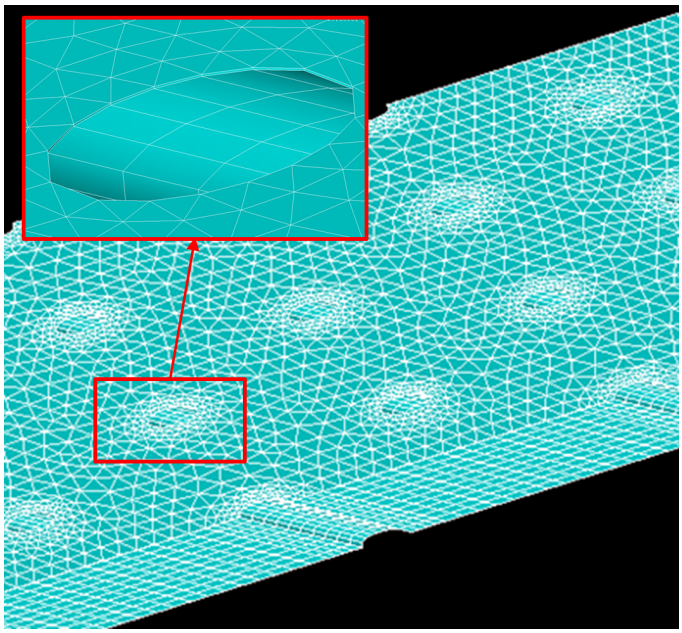

Figure 3.7: Meshed model for cold side heat flux evaluation

to estimate the convective load. Typical set values are around the range $HTC_{hole} = 400 - 450 W/(m^2K)$, depending on test conditions. The flow temperature is imposed on the basis of experimental tests.

- Plenum side of the liner plate (i.e. the annulus surface for hot side test and the internal surface of the combustion chamber for cold side test): a constant convective load, derived from natural convection correlation, is applied to the whole surface ($\approx 24 W/(m^2K)$).

- Measurement surface (i.e. the TLC side of the liner plate): a bi-dimensional convective load is applied according to the iterative procedure described below.

Electrical loads:

- Inconel heating foil: a DC voltage difference is applied at the two extremities of the model, in accordance with the values employed during experimental tests.

As the heat transfer coefficient distribution on the TLC painted surface is the unknown parameter, an iterative approach must be used in order to correctly asses the FEM simulation loads. The flow diagram of Fig. 3.8 summarizes the developed iterative procedure, which couples a MatLab in-house code to Ansys simulations.

As previously stated, wall temperature map T_w is evaluated by means of TLC steady state technique and T_{aw} has assumed as the free-stream temperature directly measured with thermocouples during the tests. At the first iteration, a constant $\dot{q}_{conv}$ value is imposed on the whole measurement surface, in detail $\dot{q}_{Joule}$ is employed as starting input, theoretically assuming an uniform heat generation and no heat losses through the plate. Exploiting Equation 3.3 the bi-dimensional convective load distribution is hence calculated and is used as a thermal load for the FEM model.

The primary outputs from Ansys calculation are a new-computed wall temperature map and the relative $\dot{q}_{conv}$ distribution, this is then used, substituting the previously imposed constant heat flux, to evaluate the HTC

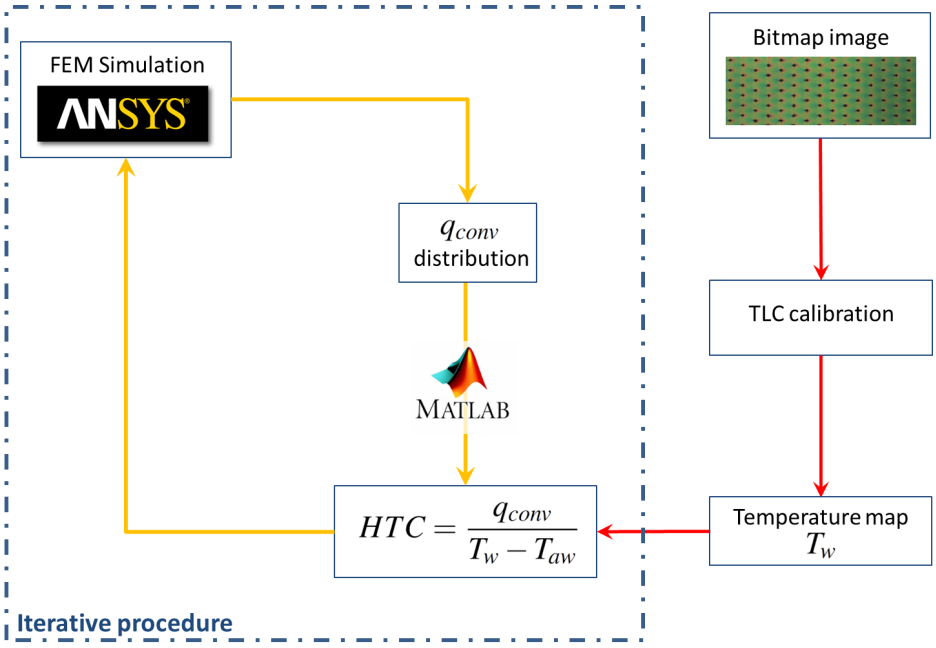

Figure 3.8: Iterative post-processing procedure

distribution on the test surface and to complete the procedure loop. Data issued from each iteration are then applied on the FEM model for the following iteration. The whole procedure stops when the mean difference between the temperature distributions coming from the FEM calculation and the TLC data is below $0.5K$, typically 4-5 iterations are required.

To verify the robustness of the procedure, a series of FEM simulations with the convective loads applied to the plate plenum side and within the effusion holes enhanced of 50% with respect to the employed correlation are performed. Results shown that the variation of the HTC is about 5%, anyway confined inside the relative error committed on the calculation of the heat transfer coefficient.

3.3 PSP for film effectiveness measurements

Pressure sensitive paint (PSP) is an organic substance, composed by oxygen sensitive molecules embedded in the paint solution using a polymer binder permeable to oxygen. Through the exploitation of the luminescence behaviour of these molecules, PSP can be used to measure the oxygen concentration of the atmosphere surrounding the paints, which in turn can be linked to the partial pressure of air.

As schematise in Fig. 3.9, electrons in the oxygen sensitive molecules are excited to higher energy levels by an incidence light of a certain frequency (UV wavelength band). From the excited state the molecule has several competing relaxation paths. The path of interest for PSP involves a forbidden transition to an excited triplet state from which the molecule may simply emit a photon. However, if there is oxygen present the molecule may interact with the oxygen transmitting its energy into a vibrational mode of the oxygen [87].

This radiationless deactivation results in a system where the luminescence level increases as the oxygen concentration in the binder around the sensitive molecules is decreased, this well known phenomenon is called *oxygen quenching* and a detailed analysis of this process is provided by Navarra [88],

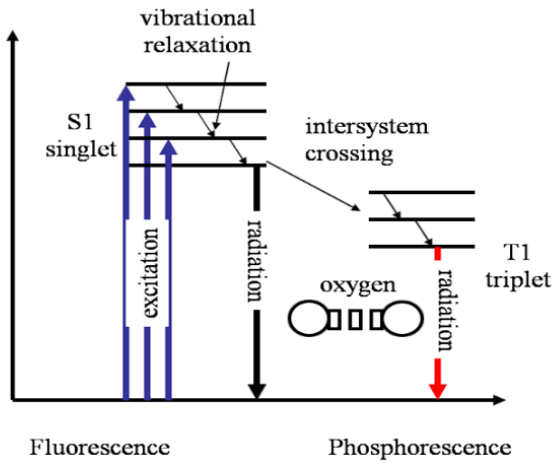

Figure 3.9: Photo-physical process governing the PSP operating principle [87]

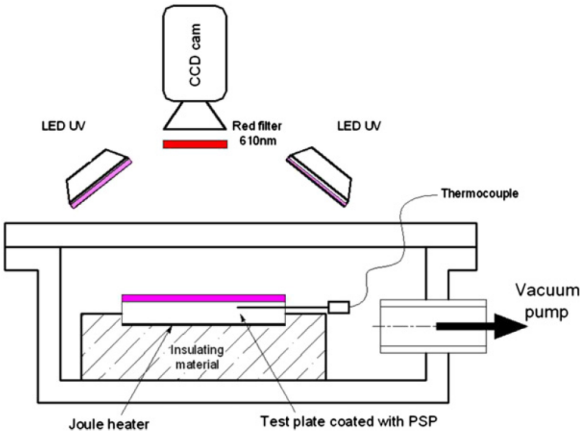

Figure 3.10: PSP calibration apparatus

employing a mathematical formulation based on the Stern-Volmer equation.

Pressure Sensitive Paints used in the present activity are supplied by Innovative Scientific Solutions, Inc. and are composed by a blend of Fluoro Isopropyl Butyl polymer (FIB) and Platinum tetra porphine (PtTFPP); paint is sprayed with an air brush directly on the test surface with 8-10 very light cross coats resulting in a total thickness between $10-30\mu m$. The PSP is fairly insensitive to the material of the base plate, any rigid (non-deforming) material impervious to oxygen can be used.

To provide an adequate excitation of the oxygen sensitive molecules an high performance UV LED Illuminator system IL104 is employed, while a 1600×1200 resolution 14-bit CCD camera (PCO.1600) is used to acquire the images. A 610 nm red filter is installed on the camera in order to ensure that the exciting UV light is not captured by the acquisition device.

Peculiar features of the PSP technique are the high resolution of the results and the reduced experiments time due to high response time. In fact, the space resolution of the measurements is practically coincident with the camera resolution and the response time is in the order of microseconds. Both these characteristics are governed by the diffusion of oxygen inside the thin layer of paint binder.

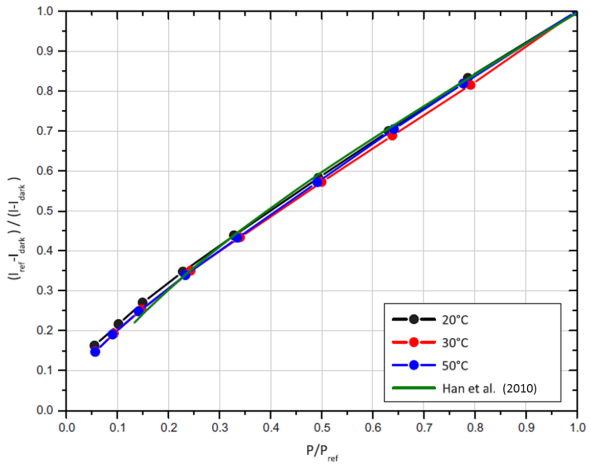

Figure 3.11: PSP calibration curves for three temperature values

Before their use on the test rig, PSP are accurately calibrated in order to relate the partial pressure of the oxygen to the intensity of the emitted light. For this purpose, a dedicated experimental apparatus (Fig. 3.10), consisting in an aluminium test plate sprayed with PSP installed in a vacuum chamber, is prepared.

Various pressures and three different temperature levels are imposed: pressure is controlled in the calibration chamber by vacuum pumps and the temperature of the aluminium test plate set by means of an adhesive electric heater. The obtained curves are reported in Fig. 3.11, adding a comparison with the results achieved by Han and Rallabandi [89] for the same paint formulation.

The pressure is normalized with the reference ambient condition P_{ref}, while the intensity values are normalized with three different reference conditions, recorded at room pressure and at the same temperature of the correspondent curve I_{ref}. In order to taking into account the background noise a non-excited acquisition is also achieved and subtracted from all the other images. As expected, the three curves collapse together allowing to neglect the temperature effect on oxygen quenching. A polynomial curve can be computed by fitting the calibration dataset, relating the air pressure to the intensity emitted by PSP:

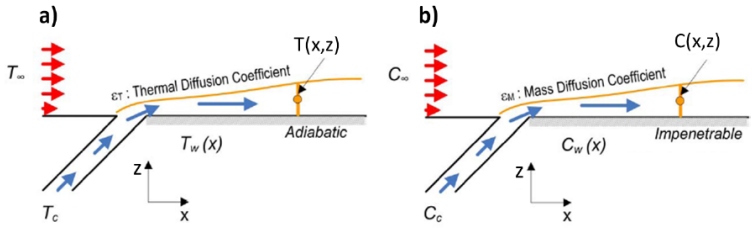

Figure 3.12: Heat and mass transfer analogy for film cooling: thermal (a) and mass transfer (b) boundary conditions [89]

$$\frac{P_{O_2}}{P_{O_2;ref}} = -0.066 + 0.716 \cdot \frac{I_{ref} - I_{dark}}{I - I_{dark}} + 0.429 \cdot \left(\frac{I_{ref} - I_{dark}}{I - I_{dark}}\right)^2 - 0.065 \cdot \left(\frac{I_{ref} - I_{dark}}{I - I_{dark}}\right)^3 = \frac{P}{P_{ref}} \tag{3.5}$$

Applicability of PSP method on film cooling effectiveness measurement is based on heat/mass transfer analogy. With reference to the Fig. 3.12a, the governing differential equations for heat transfer in a 2D turbulent boundary layer, given by Crawford and Kays [90], can be written as:

$$G_x \frac{\partial T}{\partial x} + G_z \frac{\partial T}{\partial z} = \rho \left(\epsilon_T + \alpha\right) \frac{\partial^2 T}{\partial^2 x} \tag{3.6}$$

where G represents the mass flux per unit of area, ϵ_T the turbulent diffusivity and α the thermal diffusion coefficient. The boundary conditions in case of adiabatic wall are, Eq. 3.7:

$$\begin{aligned} z = 0 \quad &\Rightarrow \quad T = T_{ad}; \quad \frac{\partial T}{\partial z} = 0 \\ z > \delta_f \quad &\Rightarrow \quad T = T_\infty \\ x = 0 \quad &\Rightarrow \quad T = T_c \end{aligned} \tag{3.7}$$

Considering the analogous case for mass transfer situation of Fig. 3.12b, where the hot mainstream has a tracer element concentration of C_∞ and the

coolant has a tracer concentration of C_c, the governing equation are:

$$G_x \frac{\partial C}{\partial x} + G_z \frac{\partial C}{\partial z} = \rho \left(\epsilon_C + D\right) \frac{\partial^2 C}{\partial^2 x} \tag{3.8}$$

where C is the mass fraction, ϵ_C the turbulent mass diffusivity and D the mass diffusion coefficient. For an impenetrable wall situation, the following boundary conditions can be assumed:

$$\begin{aligned} z = 0 \quad &\Rightarrow \quad C = C_w; \quad \frac{\partial C}{\partial z} = 0 \\ z > \delta_f \quad &\Rightarrow \quad C = C_\infty \\ x = 0 \quad &\Rightarrow \quad C = C_c \end{aligned} \tag{3.9}$$

It is easy to observe that the set of equations for heat and mass transfer situations have same modelling expression. Moreover, if the boundary conditions of the two analogous problems are the same and if the molecular and turbulent Schmidt number Sc_T are identical to molecular and turbulent Prandtl number Pr_T respectively (i.e. turbulent Lewis number Le_T equal to one), the solutions of the heat and mass transfer phenomena are identical:

$$Le_T = \frac{Pr_T}{Sc_T} = \frac{\epsilon_T + \alpha}{\epsilon_C + D} \approx 1 \tag{3.10}$$

Despite the fact that the applicability of heat and mass transfer analogy has limitations, especially for fluid field where viscous effects are dominating, based on several literature works [90, 91, 89], the stipulation of an unitary turbulent Lewis number is legitimate for turbulent gaseous flow fields such as those encountered in the present work. For this reason is possible to asses:

$$\eta_{ad} = \frac{T_{main} - T_{ad}}{T_{main} - T_{cool}} \equiv \frac{C_{main} - C_w}{C_{main}} \tag{3.11}$$

where C_{main} is the oxygen concentration of main free stream and C_w is the oxygen concentration in proximity of the wall. According to Charbonnier

et al. [92], Equation 3.11 can be expressed in terms of partial pressure of oxygen as measured with PSP:

$$\eta_{ad} = \frac{C_{main} - C_w}{C_{main}} = 1 - \frac{1}{\left(1 + \left(\frac{P_{O_2;air}/P_{O_2;ref}}{P_{O_2;fg}/P_{O_2;ref}} - 1\right)\frac{W_{fg}}{W_{air}}\right)} \tag{3.12}$$

subscripts fg and air indicate, respectively, the case with foreign (tracer) gas and air injection through cooling system; while ref is used to identify a reference case. In the case $W_{fg}/W_{air} \approx 1$, as for nitrogen injection employed in this activity, the Equation 3.12 is simplified as:

$$\eta_{ad} = \frac{C_{main} - C_w}{C_{main}} = 1 - \frac{P_{O_2;fg}/P_{O_2;ref}}{P_{O_2;air}/P_{O_2;ref}} \tag{3.13}$$

In order to perform the adiabatic effectiveness distribution using PSP technique four types of images are needed for each tested flow condition. The experimental apparatus is equipped with the same illumination system and camera used for calibration test and each type of image is evaluated as an average of at least 10 images to reduce measurement noise.

1. *Dark Image*: it is acquired with the UV illumination system switched off and no flow conditions. It is necessary to correct the background noise of the camera CCD (I_{dark}).

2. *Ref Image*: acquisition employed turning on the excitation light, with no flow condition; it represents the reference intensity field of the measurements (I_{ref}).

3. *Tracer Image*: the desired flow conditions are set and the UV light is kept on. Foreign gas is injected for the cooling line, while air is used for the mainstream flow (I_{fg}).

4. *Air Image*: analogous flow conditions with respect to Test 3, but with air employed as a coolant (I_{air}).

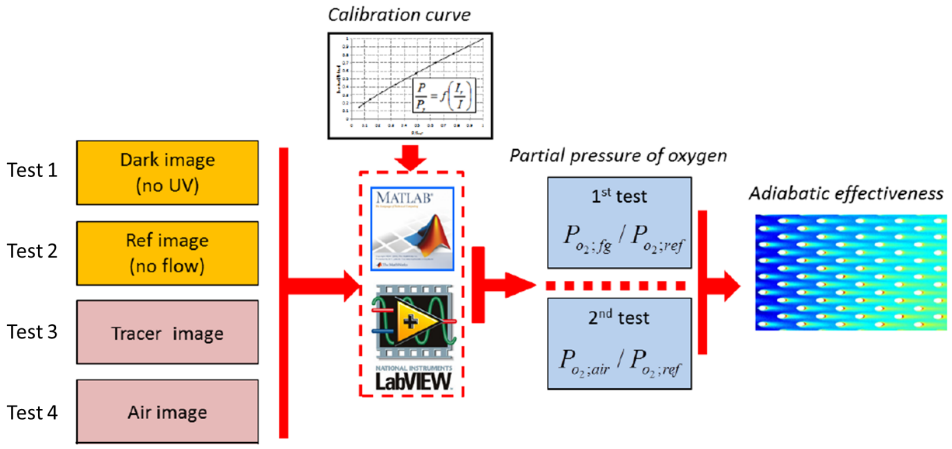

Figure 3.13: Block diagram of the PSP post-processing procedure

Exploiting the calibration curve (Equation 3.5) is possible to estimate pixel by pixel the normalized partial pressure of oxygen $P_{O_2}/P_{O_2;ref}$ for both Test 3 ($I = I_{fg}$) and Test 4 ($I = I_{air}$). Then, the two partial pressure distributions are combined as suggested by Equation 3.13 to obtain the adiabatic effectiveness bi-dimensional map. A schematic description of the experimental procedure is summarized in Fig. 3.13,

3.4 Measurement uncertainty

All the results derived from experiments or tests are measured with devices and sensors that are characterized by an instrumentation accuracy, so it is mandatory the knowledge of the measurement uncertainty related to a single or multiple data. On the whole, the uncertainty analysis may be divided into two parts:

- uncertainty in primary or direct measurements
- uncertainty in a result derived from primary measurements

A primary measurement is one that is not derived from any other, (e.g. voltage from a voltmeter, temperature from a thermometer, etc.) In this case the uncertainty is the symmetrical band around a measurement within which the true value should fall. For example, the temperature measurements, carried out in this activity given by means of T-type thermocouples, can be expressed as: $T = 300K \pm 0.5K$

The second type of uncertainties are related to measurement results that are obtained by properly combining the previous ones (e.g. mass flow rates, adiabatic effectiveness, heat transfer coefficients). Generally, these are the more common in an experimental activity and it is important to understand how the uncertainties associated to primary measurements can affect the final data. For the present study, the average experimental uncertainty has been computed following the method proposed by Kline and McClintock [93].

If G is the observed quantity of an experiment, that is a given function of n independent variables g_i, which in turn are influenced by a partial absolute uncertainty $\pm\Delta g_i$, it is straightforward to write the following equations:

$$G = f(g_1, g_2, ..., g_i, ..., g_n) \tag{3.14}$$

$$G \pm \Delta G = f(g_1 \pm \Delta g_1, g_2 \pm \Delta g_2, ..., g_i \pm \Delta g_i, ..., g_n \pm \Delta g_n) \tag{3.15}$$

where the overall uncertainty in the result ΔG is given by:

$$\Delta G = \sqrt{\left(\Delta g_1 \frac{\partial f}{\partial g_1}\right)^2 + \left(\Delta g_2 \frac{\partial f}{\partial g_2}\right)^2 + ... + \left(\Delta g_n \frac{\partial f}{\partial g_n}\right)^2} \tag{3.16}$$

For example, applying the equation reported above, it is possible to estimate the global uncertainty of the mass flow rate measurement. This is measured with orifices or calibrated nozzles, therefore, the global uncertainty is given by the combination of the partial uncertainties in the primary measurement of the apparatus geometrical dimensions, the relative pressure and the temperature.

The estimation of the uncertainties of the measured or calculated quantities are performed starting from the information given by the manufacturer of the instrumentation and applying the previous equations. Generally, datasheets reports the uncertainties usually with a level of confidence of 95% referring to a Gaussian distribution. The piezo-resistive relative pressure sensors, used to measure the static pressure in different locations of the test rig have an uncertainty of $\pm 7.0 Pa$, while the T-type thermocouples have an uncertainty level of about $\pm 0.5 K$.

The mass flow rates are measured using orifices and calibrated nozzles, according to the indication of the Ente Italiano di Normazione - UNI [94].

For PIV measurements, according to Westerweel [95], the uncertainty,

Table 3.1: Uncertainty analysis

Variable		Meas. Technique	Uncertainty	Units
d	Hole diameter	–	±2%	[–]
–	Geometrical dimensions	Caliber, ruler	±1%	[–]
T	Temperature	T-type thermocouples	±0.5	$[K]$
P	Pressure	P.S. DSA3217 1 psi	±7	$[Pa]$
P	Pressure	P.S. DSA3217 5 psi	±17	$[Pa]$
$\dot{m}_{cool}$	Cooling mass flow	Orifice/Calibrated nozzle	±5%	[–]
$\dot{m}_{main}$	Main mass flow	Orifice	±6%	[–]
$\dot{q}_{Joule}$	Joule heat	Agilent 34970A/Agilent N5763A	±4%	[–]
U	Velocity field	PIV	±10% (max)	[–]
HTC	Heat transfer coefficient	TLC technique	±10%	[–]
η_{ad}	Adiabatic eff.($\eta_{ad} > 0.8$)	PSP technique	±2%	[–]
η_{ad}	Adiabatic eff.($\eta_{ad} < 0.2$)	PSP technique	±10%	[–]

with a particle displacement varying from 5 and 15 pixels, is estimated between ±4% and ±10% (depending on the local velocity and on the chosen time delay between the two laser pulses). Uncertainty contributions due to the seeding particles not exactly following the flow motion have been neglected since the reduced particles dimensions keep Stokes number values below 10^{-3}.

Table 3.1 summarizes the contributions to the uncertainties for each parameter as well as the absolute or percentage error; all the experimental uncertainty estimates are based on a 95% confidence level.

Chapter 4

Experimental Apparatus

Contents

4.1 Three sector test rig 69
4.1.1 TSTR test conditions 76
4.2 Cold side test rig 79
4.2.1 CSTR test conditions 83
4.3 Test matrix 87

The present chapter reports in detail the experimental apparatus employed in this work. PIV, HTC measurements on liner hot side and adiabatic effectiveness tests are performed on the same three sector test rig, conveniently commissioned for each campaign (Section 4.1). Investigation on liner cold side is carried out on a dedicated experimental arrangement sharing some parts with the previous one (Section 4.2).

4.1 Three sector test rig

The experimental apparatus, depicted in Fig. 4.1, consists of a non reactive three sector planar rig installed in an open loop wind tunnel facility; the main characteristics of the rig are the three swirlers for lean-burn aero-engine and a complete liner cooling scheme, consisting of a slot injection, reproducing the exhaust dome cooling mass flow, and an effusion perforation on the

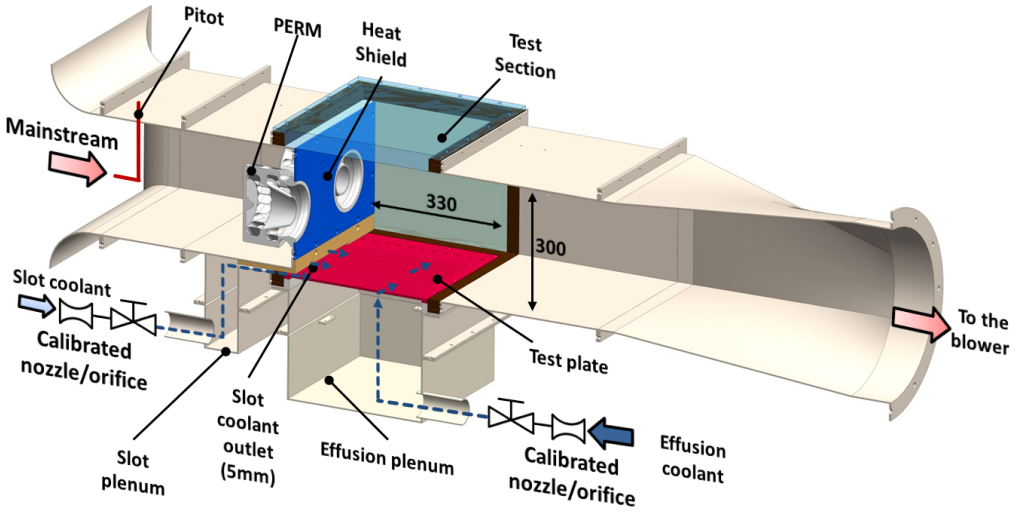

Figure 4.1: Cross sectional view of the three sector test rig

liner surface.

A $90kW$ centrifugal blower with a maximum flow capability of about $8400m^3/h$ is employed to drawn the mainstream; the flow rate is set up by guiding the motor speed between 300 and $1800rpm$.

Before entering into the test section, the main flow is swirled by a set of injectors fixed at a planar dome (Fig. 4.2). In an annular combustion chamber the burners are positioned regularly along the circumference, hence the flow field within combustion chambers can be considered periodical. To reproduce this periodicity and to lessen the effects of the lateral walls, three burners are installed in the test rig. The scaled up injectors reproduce the

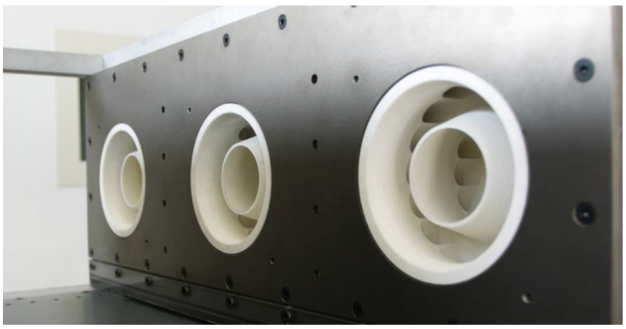

Figure 4.2: Perm injectors installed on the test rig

geometry of a Avio Aero PERM (Partially Evaporated and Rapid Mixing) swirler and are realized in plastic material using rapid prototyping technology. PERM injector is composed by two separate radial co-rotating swirlers used to impose angular momentum and a strong acceleration to two distinct inlet air flows. Models installed in the rig are manufactured without the fuel supply ducts; while on the real engine the primary fuel is fed by a central pressure atomizer and the secondary fuel is issued by internal channels creating a liquid film onto the internal nozzle surface. A more detailed description of PERM injection system is reported in Section 1.3.

The swirled air, coming from the injectors, enters into the central test section (about x=330mm, y=750mm, z=300mm) which reproduces an aero-engine lean combustor chamber scaled up with respect to the actual configuration to achieve a good resolution of the measurements in terms of flow field and spatial accuracy of the optical measurements. The top side of the test section (opposite side respect to the liner plate) is made of transparent PMMA (Poly-Methyl Methacrylate) in order to guarantee the correct optical access for the measurements.

During tests, the mainstream mass flow rate is imposed guiding the rotating speed of the centrifugal blower by means of an inverter; a Pitot tube,

Figure 4.3: Swirlers flow check experimental apparatus

located downstream of the rig inlet mouth, is used to estimate the main mass flow rate which is actually double checked by measuring the swirlers pressure drop and knowing their effective area. For each injector, a preliminary flow check was carried out in the dedicated test rig reported in Fig. 4.3. It consists of a 600 x 500 x 500mm plenum connected to a vacuum pump system used to draw air at ambient conditions through the swirler.

The multi-perforated test plate is housed on the bottom wall of the test section as it represents the inner liner of the combustor chamber. This component can be easily replaced in order to test different effusion schemes; during the whole experimental activity within the LEMCOTEC project, three different plates are investigated varying the holes inclination angle ($\alpha = 20°$, 30°, 90°), keeping constant all the other geometrical characteristics. In detail, the effusion geometry consists of a matrix of 1184 holes ($d = 1.65mm$) arranged in a 23 rows staggered configuration along the liner axis (Fig. 4.4). The streamwise and spanwise pitches are respectively $S_x = 12.6mm$ and $S_y = 9.9mm$ and the first row of holes is located about $0.22S_x$ after the slot injection, while last row of holes is located about $280mm$ downstream. Coolant feeding is supplied by a dedicated large plenum positioned underneath the liner.

Regarding the slot system, the coolant exit is located below the three swirlers; it has a constant height of $5mm$ and it extends between the axis of the two lateral swirlers. The slot system, used to generate film cooling in the very first part of the test plate, is fed by cooling air using a plenum chamber connected directly upstream the slot exit and provided with screens and flow straighteners.

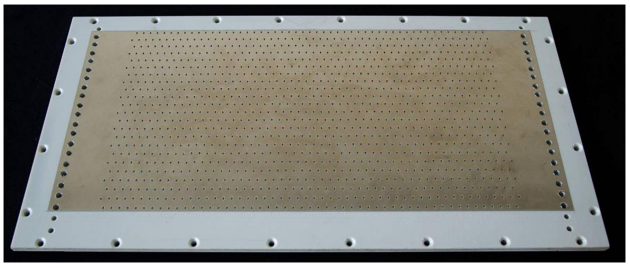

Figure 4.4: Effusion plate with Inconel foil

The slot and effusion flows are set up by throttling two distinct valves located on the cooling ducts. Both feeding lines are equipped with calibrated nozzles or orifices in order to measure the mass flow rates. A pressure scanner Scanivalve®DSA 3217 with temperature compensated piezoresistive relative pressure sensors (full scale values: $1psi$ and $5psi$) measures the static pressure in 10 different locations with a maximum uncertainty of $\pm 17Pa$ (level of confidence of approximately 95%). Regarding the pressure taps positioning:

- Three pressure taps are located upstream of the set of swirlers in the rig entrance region (P_{in}).
- Three pressure taps are positioned downstream of the test section in the main channel (P_{out}).
- Two pressure taps for each of the two coolant plenum (P_{slot} and P_{eff}).

Several T type thermocouples (uncertainty $\pm 0.5K$ with level of confidence of 95%), coupled with a dedicated reference joint, are connected to a data acquisition/switch unit (HP/Agilent® 34972A) and measured the mainstream and the coolant static temperatures.

Exhaustive information on CFD calculations to support the experimental apparatus design and rig scaling criteria are reported in [96].

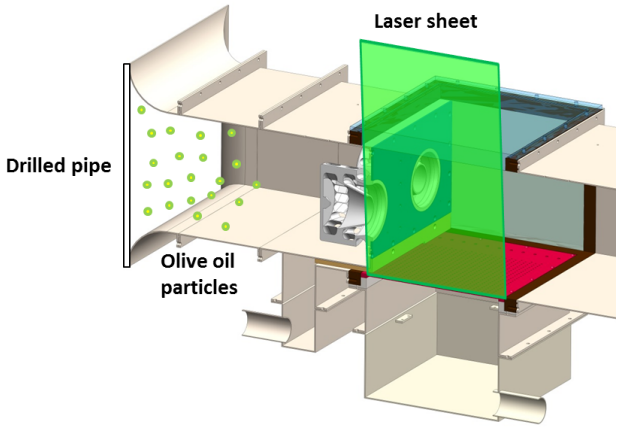

Figure 4.5: Sketch of PIV set-up

For PIV campaign, flow field measurements are performed on the plane orthogonal to the liner plate crossing the central swirler axis, as depicted in Fig. 4.5. The laser sheet was generated parallel to the test plate and is deviate by $90deg$ through a mirror inclined of $45deg$ installed above the upper transparent window of the test rig. The positioning of the camera/laser system is done using a traverse system with the help of a dedicated calibration device located inside the test section; the optical access is guarantee by one of the lateral PMMA window, while all the other walls of the test section are painted with opaque black coating to avoid reflections. The seeding necessary for the measurements was introduced upstream of the intake of the main inlet section, by means of a drilled pipe with 15 holes of $1mm$ in diameter. Olive oil particles with a mean diameter of about $1\mu m$ are provided by a Laskin nozzle.

For HTC measurements, the effusion plate is uniformly sprayed with TLC and the Inconel heating foil is connected to two copper bus bars positioned on the liner lateral sides. A DC power supply (Agilent® N5763A) electronically controlled is used to supply the required Joule heating for crystals activation. The illumination of the investigation surface is provided by two $18W$ LED tubes installed upon the top window of the test section. A picture of the test section with the TLC activated is reported in Fig. 4.6.

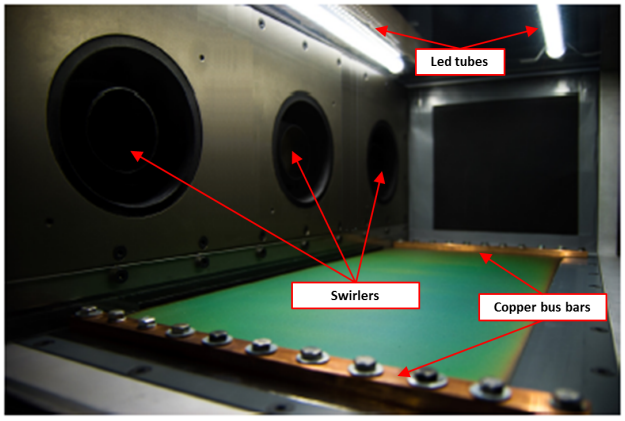

Figure 4.6: Test section set-up for HTC measurements. View of TLC activation for smooth liner [13]

To perform adiabatic effectiveness tests, the two cooling plenum chambers are fed with air or pure nitrogen, stored in a 6000 litres pressure tank ($\approx 6\ bar; 290\ K$), and the two distinct feeding ducts are both equipped with orifices in order to govern the coolant mass flow rates. The optical access for the camera and the illuminating system is obtained through the PMMA top window. The illuminator, equipped with a special lens for UV light, provides an uniform illumination spot of about $0.36m$ of diameter at $1m$ distance.

4.1.1 TSTR test conditions

Experiments under real engine conditions usually require huge efforts in the experimental set-up and also in the application of appropriate measurement techniques. A non-reactive planar rig, working at nearly atmospheric conditions, is assumed as an useful compromise in order to ensure comparability with the engine conditions and to provide high detailed results in terms of flow field and liner thermal performance. Considering mainstream flow, the test rig allows to replicate the real-engine pressure drop across the injectors, which is identified as the most significant parameter in the definition of the flow field inside the combustor; it is defined as:

$$\frac{\Delta P}{P} = \frac{P_{in} - P_{out}}{P_{in}} \tag{4.1}$$

where the subscript *in* indicates the region upstream of the set of swirlers and the subscript *out* a section downstream of the test plate. This parameter is directly linked to the mainstream Mach number and consequently to the reduced mass flow; during the entire experimental campaign it is maintained constant at the reference design value of 3.5% . The influence of the swirler pressure drop in terms of liner heat transfer was already studied in a previous work conducted on the test rig, pointing out an almost negligible effect of varying $\Delta P/P$ on the normalized Nusselt number [13] .

Still Regarding the main flow, drawn from the ambient at atmospheric condition, the other relevant parameter is represented by the Reynolds number Re_{main}, defined as:

$$Re_{main} = \frac{\dot{m}_{main} \cdot d_h}{A_{main} \cdot \mu_{air}} \tag{4.2}$$

where A_{main} is the cross section area of the test rig and d_h the hydraulic diameter used as reference length. Unfortunately, due to the necessity to work at atmospheric conditions and considering the maximum mass flow rate manageable by the blower, it is not possible to replicate the real engine mainstream Reynolds number. Anyway to obtain a Re_{main} value in fully

turbulent regime, the test model was designed with the maximum feasible scale considering the capability of the facility.

Focusing the attention to the cooling system, the most important dimensionless parameters characterizing the effusion scheme and affecting the HTC and adiabatic effectiveness distribution are identified in the pressure drop across the multi-perforated plate, the effusion holes Reynolds number and in the cooling device density ratio:

$$\Delta P/P_{eff} = \frac{P_{eff} - P_{out}}{P_{eff}} \tag{4.3}$$

$$Re_{eff} = \frac{\dot{m}_{eff} \cdot d}{A_{eff} \cdot \mu_{cool}} \tag{4.4}$$

$$DR = \frac{\rho_{cool}}{\rho_{main}} \tag{4.5}$$

the term P_{eff} is evaluated as the averaged static pressure measured in the effusion plenum located underneath the liner, while the effusion Reynolds number employs the holes diameter d as the reference length.

The adopted scaling criteria described for the main flow and the capability of the facility do not allow to reproduce all the parameters listed above. Also in this case, the main scaling parameter considered and replicated during tests is the effusion pressure drop.

The achieved holes Reynolds number is approximately equal to 4000, significantly below typical values above 25000 in actual engines, nevertheless Re_{eff} is expected to have a marginal impact on the measured thermal quantities, due to the negligible influence on the turbulent generation at hole outlets that could impact heat transfer and film covering especially in a limited region around holes.

Using air and nitrogen at ambient temperature for the cooling line, the

obtained density ratio at test condition is $DR \approx 1$; this value is below the actual combustor chamber conditions, typically around $DR = 2.5$. Concerning the influence of density ratio on film cooling performance, Andreini et al. [35] pointed out that velocity ratio, and thus the effusion pressure drop, is the driving parameter for the heat transfer phenomena, while regarding the effectiveness, results show that η_{ad} is less sensitive to the cooling flow parameters, especially at the higher blowing and velocity ratios.

These considerations are still valid also for the slot system, where the considered similitude parameter is represented by the slot coolant consumption W:

$$W = \frac{\dot{m}_{slot}}{\dot{m}_{main}} \cdot \frac{3}{2} \tag{4.6}$$

the coefficient 3/2 takes into account that the slot is located between the axis of lateral swirlers, covering only two of the three sectors of the test section. Slot Reynolds number is defined assuming as a reference length the slot height h:

$$Re_{slot} = \frac{\dot{m}_{slot} \cdot h}{A_{alot} \cdot \mu_{cool}} \tag{4.7}$$

at the engine reference condition, a slot Reynolds number value of about 3500 is achieved on the test rig. For sake of clarity, the test conditions are here summarized in Table 4.1.

Main flow	Effusion flow	Slot flow
Air	$N_2 - Air(PIV)$	$N_2 - Air(PIV)$
$T_{main} = 300K$	$T_{eff} = 300K$	$T_{slot} = 300K$
$Re_{main} = 160000$	$Re_{eff} = 0 - 4000$	$Re_{slot} = 0 - 3500$
$\Delta P/P = 3.5\%$	$\Delta P/P_{eff} = 0 - 1 - 2 - 3\%$	$W = 0 - 3\%$

Table 4.1: Flow conditions achieved on the TSTR

4.2 Cold side test rig

To perform the analysis of the heat transfer on the effusion liner cold side, a secondary test rig, strictly derived from the three sector apparatus, was designed. The experimental model, showed in Fig. 4.7, consists of a planar rig installed in an open loop wind tunnel reproducing the annulus of a lean combustor chamber, scaled up with respect to the engine geometry.The annulus channel is characterized by a constant cross section area (about 36mm x 520mm) and the test section with the effusion system has a length of 330mm in the axial direction.

The test rig allows the complete control of two separate flows: the bypass flow and the effusion coolant flow; the air is drawn from the ambient, thanks to a vacuum pump system (maximum capacity of 900m^3/h), and the mass flow rate is set up throttling two separated valves. Before entering into the central test section, the mainstream crosses honeycomb and a screen to set an uniform velocity. A passive turbulence generator (square grid mesh; 4mm bar thickness; 16mm grid pitch), located 64mm upstream the effusion plate,

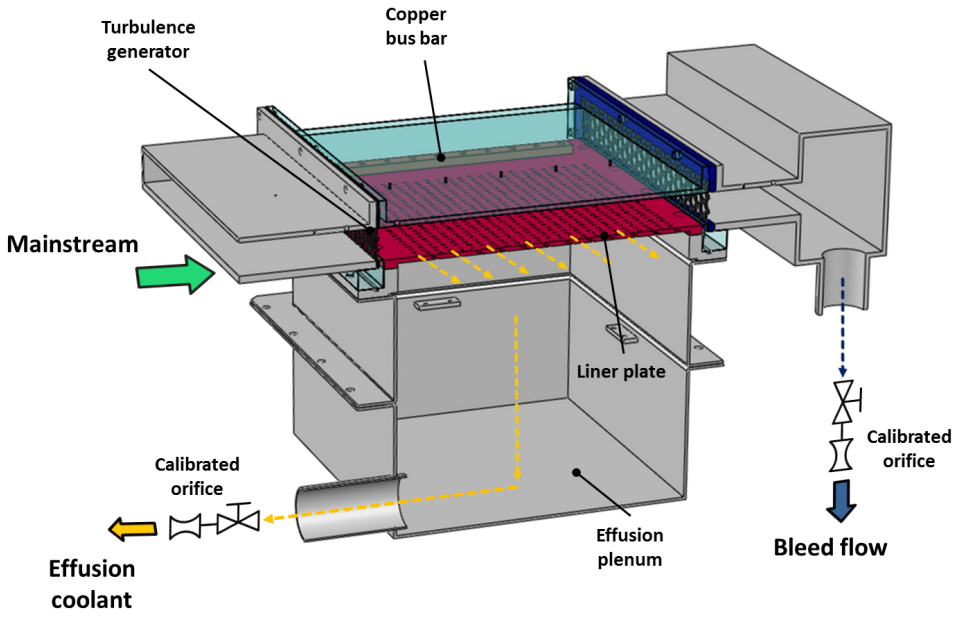

Figure 4.7: Cross sectional view of the cold side test rig

is used to achieve a turbulence level of 17% at the first row of holes [97] and a streamwise integral length scale of $7.5mm$.

The multi-perforated test plate is housed on the bottom wall of the test section and it represents the liner of the combustor chamber cold-side, the effusion flow is extracted through the perforation by a dedicated large plenum chamber located below the test plate and equipped with flow straighteners. The liner geometry and the relative plenum chamber are directly disassembled from the three sector test rig. The mass flow drawn from the ambient and not extracted by the perforation represents the bypass flow: at the end of the test rig it crosses a screen before entering into a plenum chamber connected to a dedicated line.

Heat transfer measurements are performed using the TLC steady state technique: the surface heat flux is generated by Joule effect with a thin Inconel Alloy sheet, $25.4\mu m$ thick, glued on the test plate with the same hole pattern of the effusion plate. The heating foil is electrically fed through two copper bus bars fixed near the lateral sides of the rig. For the measurements a thermochromic liquid crystal (TLC) solution with wide band characteristics (activation range from about $32°C$ to $53°C$) is used, they are thinned with water and sprayed with an air gun on the Inconel sheet (10 thin coats) after the application and the dry out of a black background paint. The top window of the test rig is made of transparent PMMA in order to have the correct optical accesses for the camera and illumination system used in the TLC technique.

The test rig is equipped with several static pressure taps and T-type thermocouples in the annulus channels and in the plenum chambers. Five equally distributed pressure taps measure the static pressure along the test section, they are used to estimate the coolant extracted from each row of holes; while 2 pressure taps monitor the pressure in the effusion plenum chamber. Static pressure measurements are performed using a Scanivalve®DSA 3217 Digital Sensor with a measurement range up to $5psi$. In the picture of Fig. 4.8 is possible to detect the locations of the thermocouples and the pressure taps; at the top of the image is visible one of the two copper bus bars, directly in contact with the Inconel foil; the central portion of the liner surface is

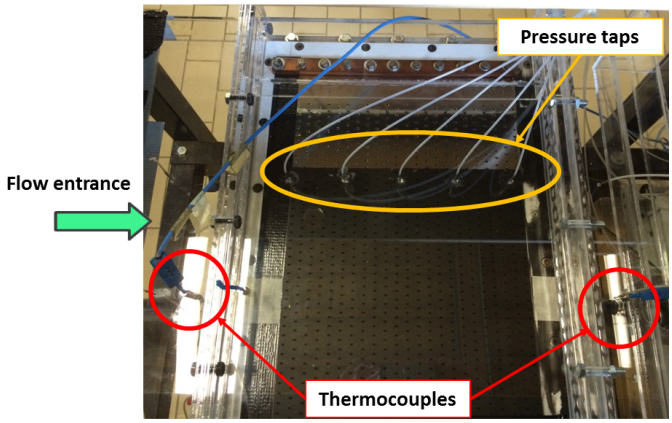

Figure 4.8: Top view of the annulus channel; location of pressure and temperature sensors

covered with black paint and TLC.

To support the design of the test model, a preliminary CFD investigation is performed with the aim to verify the occurring of an uniform coolant extraction through the effusion test plate. Computation is carried out using the commercial code Ansys CFX®15, employing two different turbulence models: $k-\epsilon$ and SST (Shear Stress Transport). As showed in Fig. 4.9, the flow streamlines tend to occupy uniformly the whole test section in the lateral direction, revealing a good response by the outlet plenum chamber in equalizing irregularly distributed pressures. Analogous results are carried out for both the two turbulence models employed.

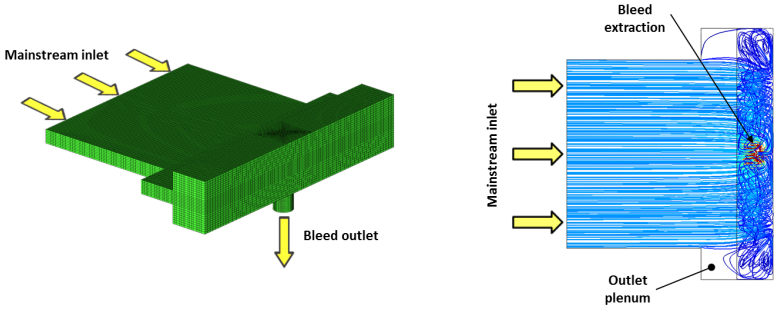

Figure 4.9: Hexa grid mesh (left). Top view of flow streamlines obtained with $k-\epsilon$ turbulence model (right)

The Thermochromic Liquid Crystals paint, the illumination system and the digital camera used to acquire the images are the same employed on the three sector test rig and the experimental set-up is conveniently arranged in order to replicate the optical condition of the calibration process.

4.2.1 CSTR test conditions

Investigation on liner cold side is carried out at ambient conditions, replicating typical engine values for some operating parameters. The air mass flow rate extracted from the multi-perforated plate is governed by the pressure drop across the effusion system:

$$\Delta P/P_{eff,CS} = \frac{P_{ann} - P_{eff}}{P_{ann}} \tag{4.8}$$

formulation shows a very similar form with respect to Equation 4.3 introduced for three sector test rig; comprehensibly, due to the reversed flow direction, in this case the static pressure measured in the effusion plenum chamber P_{eff} represents the downstream value of the system. While P_{ann} represent the averaged wall static pressure evaluated in the annulus channel. The total amount of air mass flow drawn by the pumps in the test section is governed by the ByPass Ratio (ByR), which defines the mass flow split between bleed and effusion flows. This parameter is defined as:

$$ByR = \frac{\dot{m}_{bleed}}{\dot{m}_{bleed} + \dot{m}_{eff}} \tag{4.9}$$

where with the subscripts $bleed$ and eff are indicated the respective mass flow rates evaluated in the two distinctly controlled ducts. To summarize the explored test conditions, the experimental flow conditions are reported in Tab. 4.2.

For each tested condition, a data analysis was conducted detecting across each row of holes an investigation area with a streamwise extension

$\Delta P/P_{eff,CS}$	ByR
0.5%	$0\% - 50\% - 65\% - 73\% - 78\% - 81\%$
2%	$0\% - 20\% - 40\% - 60\% - 70\%$
3%	$0\% - 20\% - 40\% - 60\% - 70\%$
4%	$0\% - 20\% - 40\% - 60\% - 75\% - 80\% - 84\%$

Table 4.2: Flow conditions imposed in the cold side HTC investigation

of S_x and a width of $3S_y$. Each investigation area is characterised by an annulus Reynolds number Re_{ann}, a working Suction Ratio parameter SR, and a spatially averaged Nusselt number Nu. These quantities for the $i-th$ row are defined below according to the sketch reported in Fig. 4.10:

$$Re_{ann;i} = \frac{U_{ann;i} \cdot \rho \cdot d_h}{\mu_{air}} \tag{4.10}$$

$$SR_i = \frac{U_{eff;i}}{U_{ann;i}} \tag{4.11}$$

$$Nu_i = \frac{HTC_{ave;i} \cdot d_h}{\lambda_{air}} \tag{4.12}$$

where $U_{ann;i}$ is the velocity of the annulus flow upstream the $i-th$ row, $U_{eff;i}$ the velocity in the effusion holes of the $i-th$ row while the $HTC_{ave;i}$ is the average heat transfer coefficient of the investigation area. In the equations 4.10 and 4.11 the velocity of the annulus flow and effusion flow are estimated starting from the pressure distribution along the annulus channel and assuming a constant discharge coefficient of the holes. The effects on heat transfer due to coolant extraction are carried out in terms of the enhancement factor parameter EF defined as:

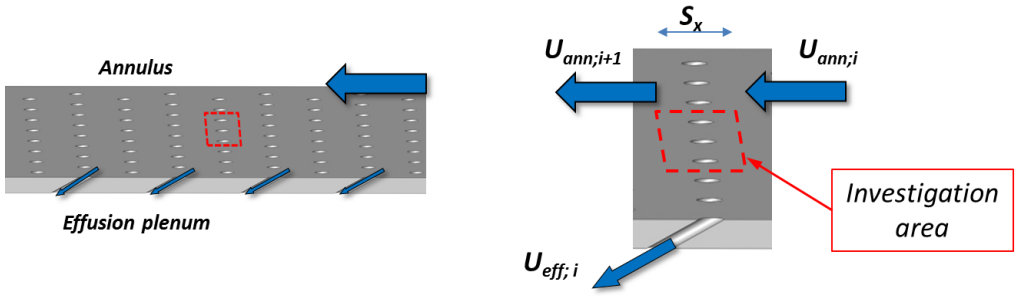

Figure 4.10: Investigation areas used in the HTC post-processing procedure

$$EF_i = \frac{Nu_i}{Nu_{0;i}} \tag{4.13}$$

where $Nu_{0;i}$ represents a reference averaged Nusselt number calculated from the Colburn correlation for fully developed flow:

$$Nu_{0;i} = \frac{0.023 \cdot Re_{ann;i}^{0.8} \cdot Pr^{0.3} + 0.023 \cdot Re_{ann;i+1}^{0.8} \cdot Pr^{0.3}}{2} \tag{4.14}$$

An analysis of the results based on definition of different parameters for each investigation areas allows to decouple the behaviour of each row of holes from its streamwise location and main flow parameters $\Delta P/P_{eff,CS}$ and ByR, and hence to explore the effect of local parameters (i.e. Re_{ann} and SR) on HTC. Fig 4.11 highlights the range of test points investigated during the whole experimental campaign and the respective real engine operating conditions. Distribution refers to the working condition of the rows of holes

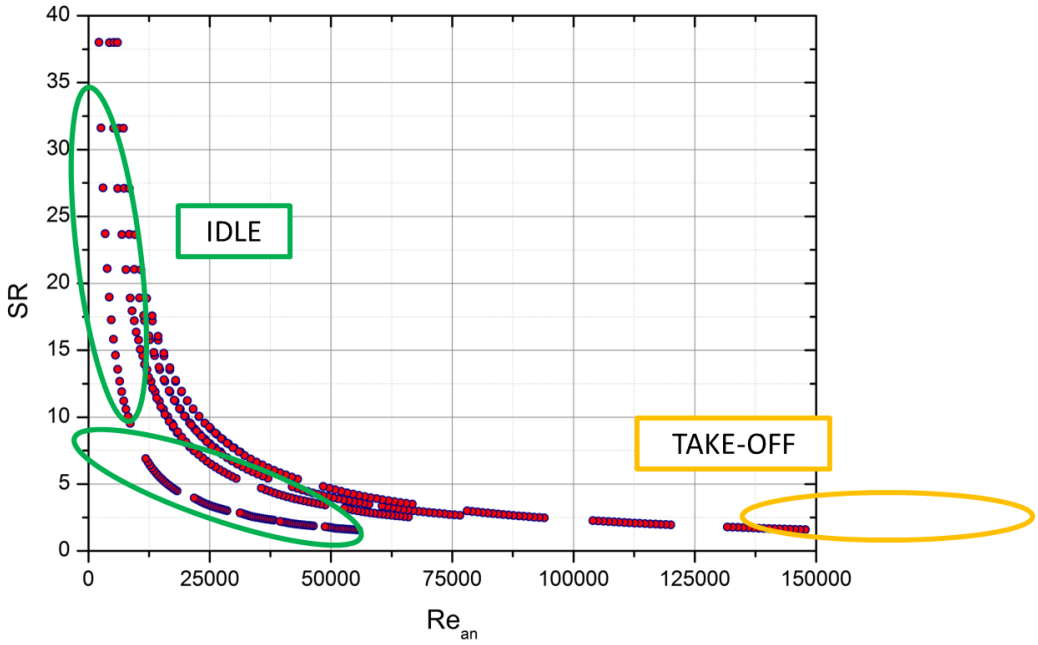

Figure 4.11: Tested SR values as a function of Reynolds number.

excluding in the analysis the first and last three rows of the test plate which are affected by boundary effects in the TLC measurements. Regarding the SR parameter, a maximum value of about 38 is detected in the case of no bleed flow. Higher annulus Reynolds numbers ($\sim$ 145000) are achieved for $\Delta P/P_{eff,CS} = 4\%$ with the higher bleed mass flow rate.

4.3 Test matrix

Several experimental campaigns are already performed on the three sector test rig in the first part of LEMCOTEC project. The activity reported in this work represents a continuation of the studies carried out by the author's research group on a simplified configuration employing a smooth liner plate [13] and on a reference effusion geometry characterized by an inclination angle of $30deg$ [70],[71].

Past studies reported in literature (Section 2.3) have highlighted a significant enhancement, at uniform mainstream conditions, of the film effectiveness decreasing the holes inclination angle up to very slanted configuration; this is due to tilted injection that tends to maintain the coolant jets attached to the test plate, assuring a good film covering. To investigate the behaviour of low α effusion system under realistic flow conditions, a test plate with an inclination angle of $20deg$ is designed. Feasibility of HTC measurements with TLC steady state technique on this geometry is prevented by manufacturing constraints on plastic material and Inconel sheet perforation with extremely high inclination angle. For this reason the component is realized in metallic material and holes are obtained by means of Electrical Discharge Machining (EDM).

The other configuration taken into deeply consideration in this activ-

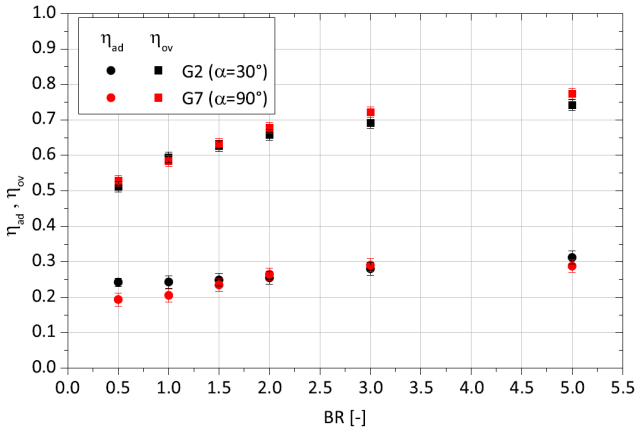

Figure 4.12: Spatially averaged overall and adiabatic effectiveness distributions [58]

ity is an effusion liner with orthogonal coolant injection. Motivation of this choice derived from outputs achieved by author's research group within the forerunner European project KIAI (Knowledge for Ignition, Acoustics and Instabilities): a very interesting behaviour is pointed out by Andreini et al. [58] in an experimental campaign focused on the evaluation of the thermal performance of multi-perforated liners by means of adiabatic and overall effectiveness measurements at uniform mainstream conditions.

As highlighted in Fig. 4.12 an $\alpha = 90deg$ geometry (indicated as $G7$) showed similar film covering performance to a corresponding inclined configuration ($G2$), even more, despite reduced heat sink effect contribution the perpendicular array achieved better thermal efficiencies at high blowing ratio conditions. This behaviour of the perpendicular array is ascribed to the low mainstream heat transfer coefficient augmentation and to the higher heat transfer coefficient inside hole due to the entrance effects. As pointed out by the authors, one of the main issues affecting the comparison is precisely the absence of a mainstream 3D flow field, which is expected to deeply interact with the coolant jets with high penetration typical of $90deg$ holes angle.

Regarding the campaign on the cold side test rig, investigation has involved the engine reference geometry ($\alpha = 30deg$) allowing to completely characterize the performance of such cooling scheme.

The test matrix of the whole activity conducted at isothermal conditions is hence reported in Table 4.3. With the symbol "O" are identified tests carried out in a previous phase of the work on the three sector test rig [96], [13], [70],[71], while the symbol "V" labels campaigns properly performed during the activity reported in the present dissertation.

Geometry	Type of Measurements			
	Flow Field	HTC hot side	HTC cold side	Film covering
Smooth plate	O	O		
$30deg$	O	O	**V**	O
$20deg$				**V**
$90deg$	**V**	**V**		**V**

Table 4.3: Test matrix

Chapter 5

Experimental Results

Contents

5.1 Flow field of PERM injector 92
5.2 Hot side heat transfer 100
5.2.1 Geometries comparison: impact of the injection angle on heat transfer 105
5.3 Film cooling effectiveness 109
5.3.1 90*deg* liner configuration 109
5.3.2 20*deg* liner configuration 114
5.3.3 Geometries comparison: impact of the injection angle on film covering 118
5.4 Cold side heat transfer 122
5.5 Concluding remarks 127

Results from the extensive experimental survey carried out at isothermal conditions on the Three Sector Test Rig and on the Cold Side Test Rig are showed in this chapter. The adoption of several measurement techniques allowed to accomplish an accurate characterization of the liner cooling system and to deepen the knowledge on the impact of the injection angle on an effusion scheme.

PIV results show typical flow structures of a lean aero-engine combustion chamber and analyse the interaction effects between the mainstream swirled

flow and the cooling system. Despite this cold flow field is not fully representative of the flow inside the combustor, the PIV investigation supports meaningfully the study of the thermal behaviour of the liner and supplies a severe benchmark test for CFD calculations.

Heat transfer coefficient and adiabatic effectiveness distributions are applicable with fair confidence to the engine conditions, providing reliable information for the preliminary design of the cooling system and suggesting possible geometry optimizations.

5.1 Flow field of PERM injector

Flow field results for the plane orthogonal to the liner crossing the central swirler are here reported in terms of velocity maps and 1D profiles. Experimental survey is performed employing the $90deg$ effusion plate under three different test conditions; a direct comparison with the $30deg$ results is showed in order to evaluate the flow field modifications varying α.

The bi-dimensional maps show the magnitude of the velocity measured on the investigation plane normalized with respect to the maximum values achieved at the reference condition with no coolant injection. The space coordinates x is made non-dimensional with the streamwise pitch S_x while the orthogonal direction z is normalized with respect to the exit diameter of the PERM injector indicated as D. Figures report only almost the entire bottom half of the investigation plane since the flow field generated by the injector is proven to be symmetric with respect to its axis. Attention is focused on the initial part of the liner ($x/S_x < 17$) where the interaction phenomena between the mainstream and coolant flows are prevalent. Due to reflection issues, the velocity distributions are achieved with a minimum distance from the liner equal to $2mm$. To clarify the position of the swirler, a sketch of the injector itself is included on the left side of the pictures.

Fig. 5.1 illustrates the flow field with no coolant injection obtained imposing the reference pressure drop across the swirlers of 3.5%. The high velocity annular jet exiting from the swirler is opened by a large central Re-

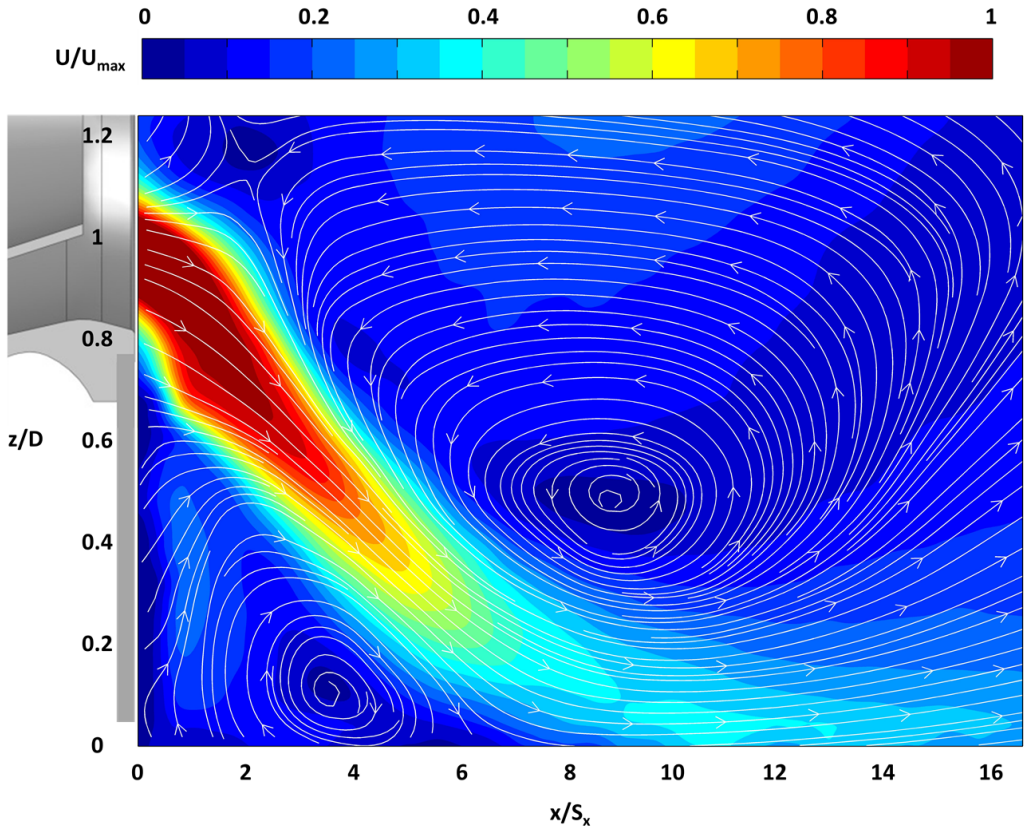

Figure 5.1: PERM flow field with no coolant injection ($\Delta P/P_{eff} = 0\%$ and $W = 0\%$)

circulation Zone (RCZ) produced by the vortex breakdown; the center of rotation of this structure can be clearly detected at $x/S_x \approx 9$ and $Z/D \approx 0.5$. Presence of wide regions of recirculating flow confirms the achievement of $S_N > 0.6$ condition [17].

The jet structure, characterized by a significant tangential expansion, impinges on the liner wall generating a stagnation point at about $x/S_x = 6$; an angle of about $40deg$ between the jet main direction and the heat shield is observed. A typical corner recirculation vortex, with clockwise rotation direction, is established in the region underneath the jet limited by the liner wall and the heat shield. This flow structure leads to negative velocity components in x direction at the liner surface, near the slot exit.

The enabling of the effusion system, by means of an imposed pressure drop across the liner of $\Delta P/P_{eff} = 3\%$, leads to the attainment of the ve-

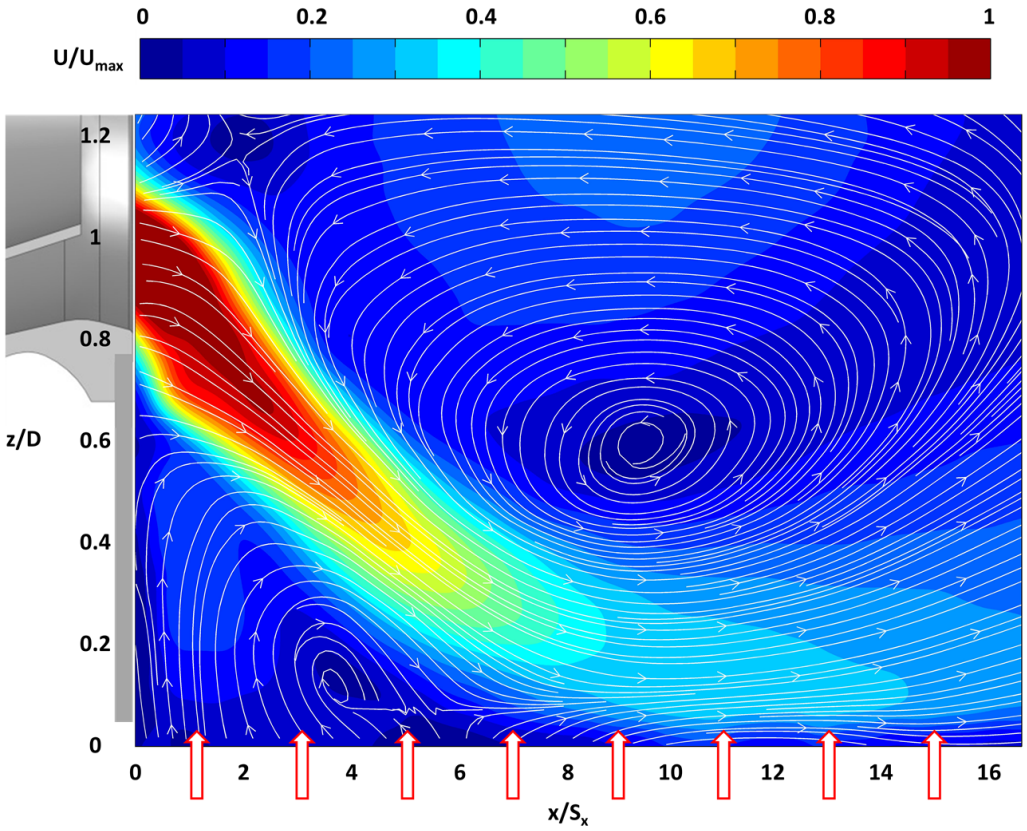

Figure 5.2: PERM flow field with only effusion coolant injection ($\Delta P/P_{eff} = 3\%$ and $W = 0\%$)

locity maps of Fig. 5.2. Minor discrepancies are detected in the the main recirculation region, while the high penetration of the coolant jets with orthogonal injection tends to lift up the jet structure, reducing the expansion angle of the swirling jet and moving slightly downstream the impinging region on the liner surface. The corner recirculating vortex observed in the no cooling condition is still well recognizable. Nevertheless, near the heat shield, the perpendicular effusion array is responsible of strong velocity components in z direction, forewarning a not ideal behaviour in terms of liner film covering.

Fig. 5.3 shows the flow field for the reference cooling condition with both the effusion and the slot systems activated: the liner pressure drop is set at a value of $\Delta P/P_{eff} = 3\%$ and the slot coolant consumption is im-

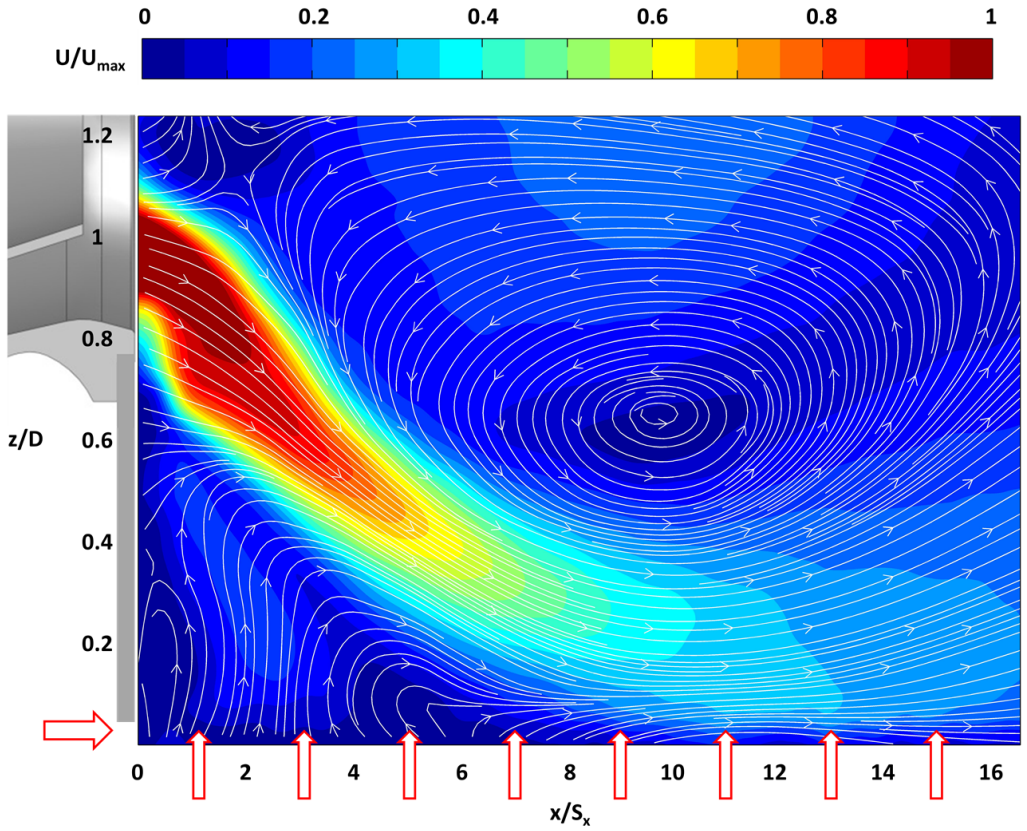

Figure 5.3: PERM flow field with effusion and slot coolant injection ($\Delta P/P_{eff} = 3\%$ and $W = 3\%$)

posed at $W = 3\%$. Slot coolant seems to have no enough axial momentum to prevail on orthogonal effusion jets and is early lifted up, generating a low velocity region established near the heat shield underneath the swirled jet. At the same time the clockwise rotating corner vortex is demolished by the interaction between effusion and slot coolant flows. The high velocity jet is further lifted up by the cooling system and consequently a minor expansion of the swirling mainstream flow is achieved, this leads to an increased angle with the heat shield of about $50deg$. The location of the center of the inner recirculation zone is moved to $x/S_x \approx 10$ and $Z/D \approx 0.7$ and also the stagnation region produced by the impinging jet is moved downstream up to $x/S_x \approx 7.5$.

These aspects are underlined by the graphs of Fig. 5.4, where four

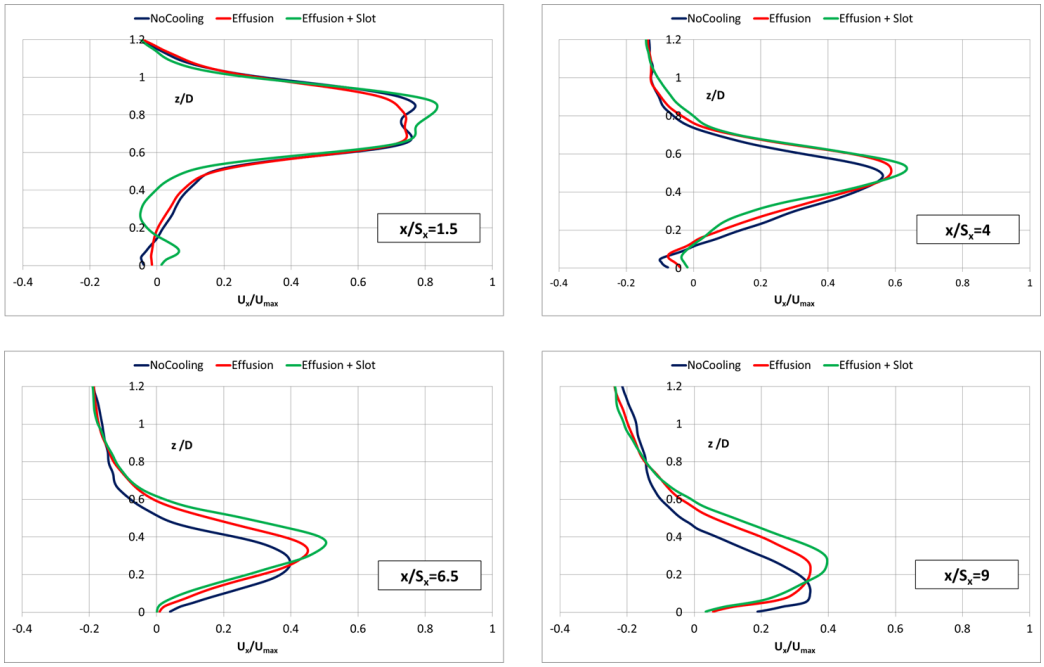

Figure 5.4: Axial velocity profiles for various streamwise locations

distributions of the normalized velocity components in the streamwise direction are respectively extracted at $x/S_x = 1.5$, $x/S_x = 4$, $x/S_x = 6.5$ and $x/S_x = 9$. Enabling first the effusion system and then also the slot, the progressive lifting of the jet, corresponding to a reduction in the aperture angle, is noticeable in all the positions: the maximum of U_x is increased in value and is moved towards higher z/D. The wide reverse flow region is highlighted by negative velocity components approaching the centre of the test section.

The effects of the slot can be observed only in the initial part of the liner ($x/S_x = 1.5$) with positive velocity components near the liner, in the other hand the clockwise rotating corner vortex leads to negative U_x at the wall, this effect is particularly present without cooling, due to more coherent structure of the vortex. Downstream of the jet stagnation region ($x/S_x = 9$) high axial velocities in proximity of the test surface are achieved in absence of coolant injection.

Focusing the attention on the corner vortex region, a direct comparison

between the just presented flow field ($\alpha = 90deg$) and the normalized velocity maps achieved with the $30deg$ configuration [70] is reported in Fig. 5.5. As it is reasonable to expect, minor discrepancies can be noticed as far the main recirculation region and the impingement jet are concerned. On the other hand strong modifications of the flow field are observed in the corner region and in proximity of the liner. With the only effusion system activated, a slanted injection leads to the generation of two counter rotating vortex structures underneath the jet. For $W = 3\%$ condition, in contra-position to the early lifting of the coolant produced by the orthogonal array, the slot flow is clearly dragged and energized by the inclined effusion coolant injection generating a region with moderated velocity near the wall.

These effects are clearly highlighted by the streamwise velocity component profiles of Fig. 5.6. As a general result, similarly shaped curves are

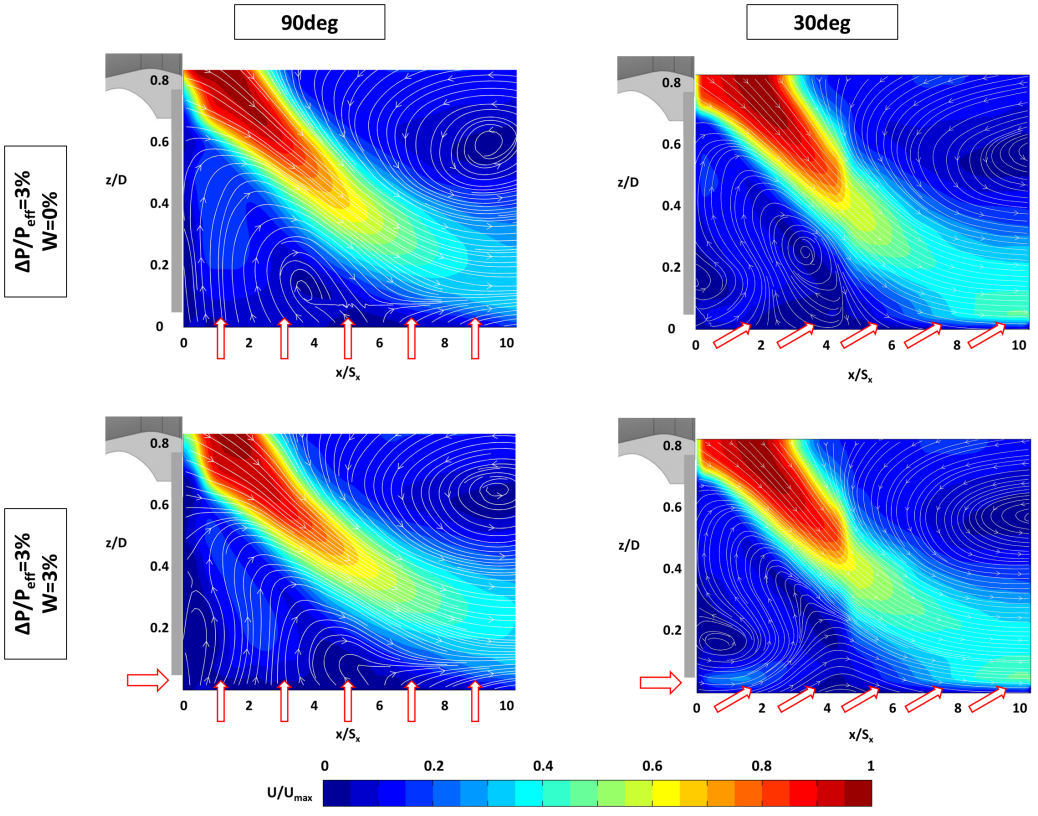

Figure 5.5: Flow field comparison varying the holes injection angle

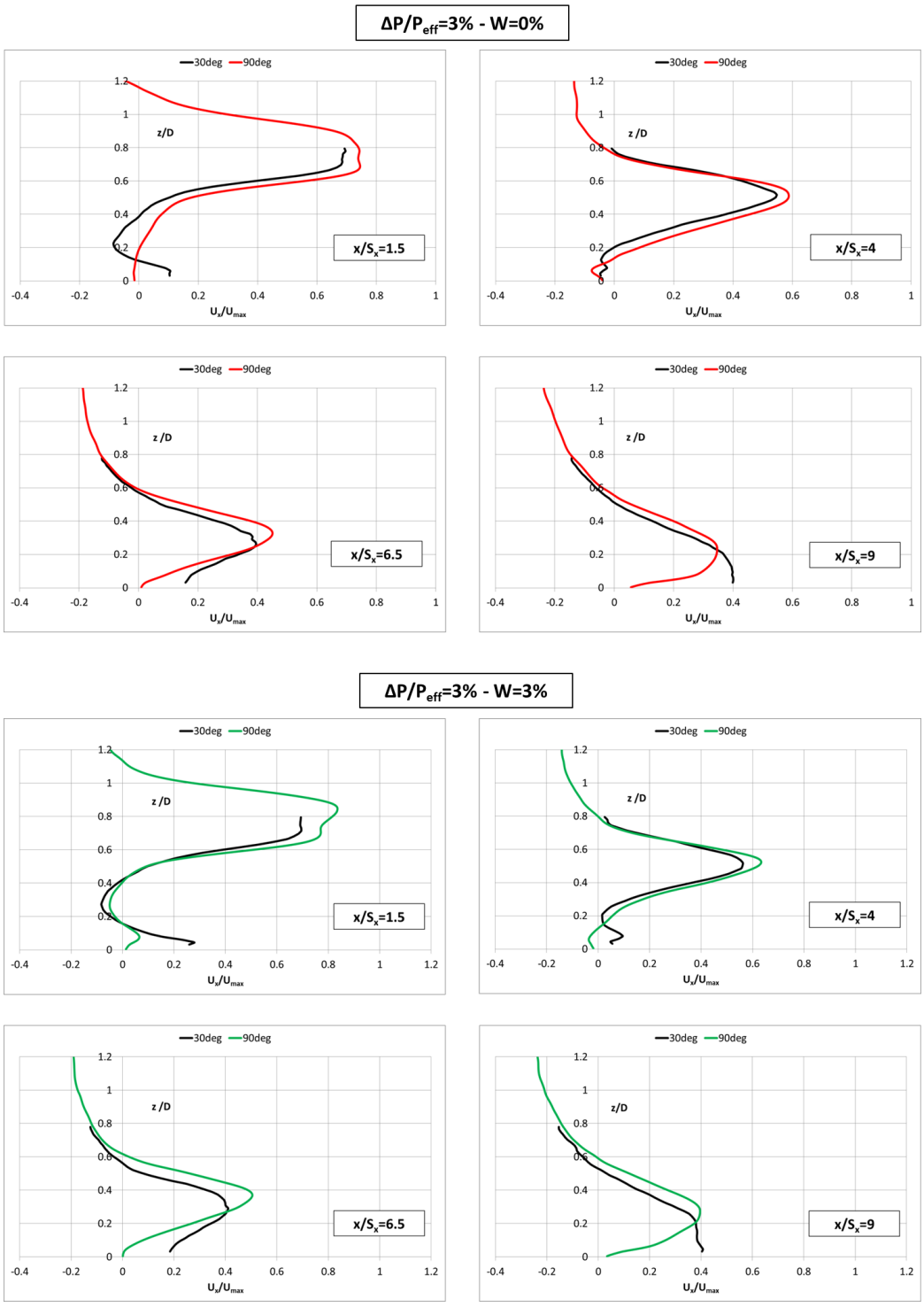

Figure 5.6: Axial velocity profiles: Impact of the injection angle

obtained in the regions more distant from the test surface ($z/D > 0.4$), while the $90deg$ geometry provides reduced U_x near the liner with respect to $30deg$. The slot generates a moderate axial velocity in the inclined configuration and its effects are visible up to $x/S_x = 4$, while in the $90deg$ test plate the effusion normal injection early destroys the slot axial jet.

5.2 Hot side heat transfer

As discussed in Section 4.3, heat transfer measurements on the liner hot side are performed on the plate with $\alpha = 90deg$. In the context of the previous European Project KIAI, one of the outcome of the test campaign performed by UNIFI was that the effusion geometry with normal injection showed a significant reduction of the heat transfer coefficient respect to the reference $30deg$ geometry: the present experimental activities allowed to deepen this behaviour in a more representative flow field condition.

It's worth to notice that the analysis of the HTC results must be coupled with adiabatic effectiveness outputs, in order to understand if the cooling system actually provides a reduction of the heat load on the gas side surface, in addition to the contribution offered by the heat removed through forced convection inside the perforation and on the liner cold side.

Several levels of effusion coolant mass flow rates are investigated, setting $\Delta P/P_{eff}$ to the values of 1%, 2% and 3%. The impact of slot cooling is also explored. The swirlers pressure drop is maintained constant at the reference value of 3.5% for the whole experimental survey.

The investigation area is represented by the portion of the liner belonging to the central sector pitch of the test section. Results report the heat transfer coefficient distributions normalized by means of a reference HTC_0, evaluated as the spatially averaged value achieved on a smooth liner without coolant injection [13]. For a better understanding, the bi-dimensional map referring to this flow condition is showed in Fig. 5.7.

The 2D distribution points out the presence of an elliptic area where the heat transfer coefficient reaches the peak values. This zone, located between $5 < x/S_x < 9$, corresponds to the location of the stagnation point of the impinging jet and of the following strong acceleration of the flow near the wall, as highlighted by the velocity distribution results. A slight shift of this peak region to the right side of the center of the test section is coherent with the sense of rotation of the three swirlers. Low heat transfer values are registered in the other zone of the test plate.

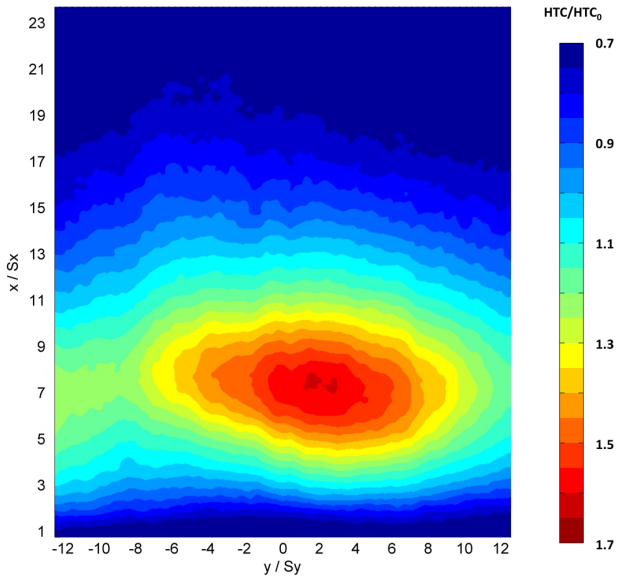

Figure 5.7: Heat transfer coefficient distribution on the smooth liner geometry ($\Delta P/P_{eff} = 0\%$ and $W = 0\%$)

To explore the influence of the effusion pressure drop on the liner heat transfer, three different cooling conditions are tested in absence of slot coolant injection. Maps, illustrated in Fig. 5.8, conserve the peak region just described for the reference geometry and reveal a more uniform HTC distribution on the whole test plate. In proximity of $y/S_y = -12$, the effects of the lateral swirler imping jet can be also observed. A limited enhancement in heat transfer is observed increasing the effusion pressure drop, with a slightly more substantial impact detected approaching the exit of the test section. Circumscribed peak values are visible immediately downstream of the holes coolant injection in the region near the stagnation region.

The system behaviour is confirmed by the laterally averaged trends displayed in Fig. 5.9. For a better understanding of the 1D trends, spatially averaged values estimated across each peak are also reported. Mean calculation is performed over regions with streamwise widths approximately equal to S_x, extending from the x location of each detected HTC peak to the following one. In the initial part of the liner no modifications are observed, with also the heat transfer peak location that remains unaltered. An increase of effusion mass flow moderately promotes the heat transfer for $x/S_x > 9$, this

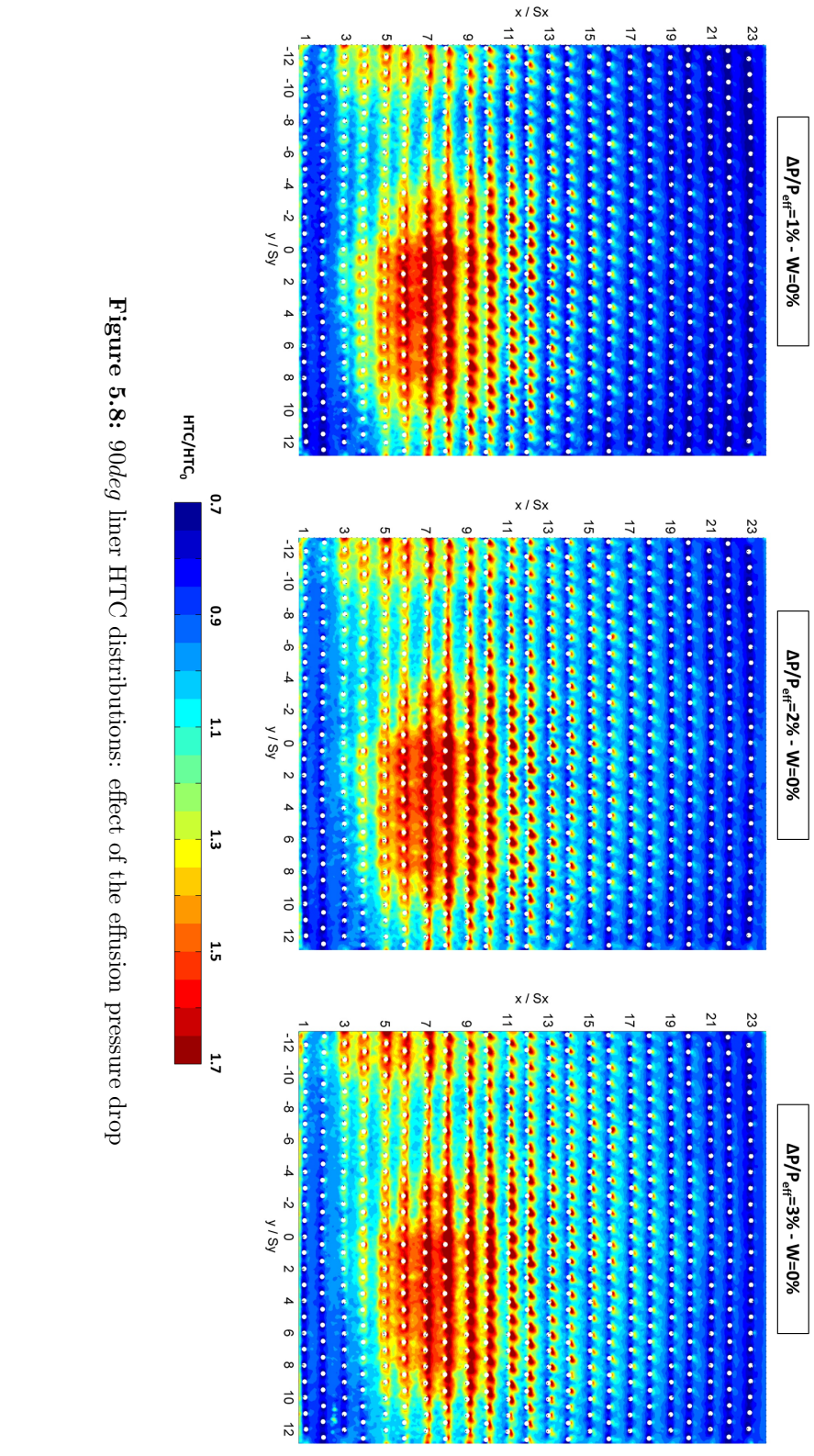

Figure 5.8: 90*deg* liner HTC distributions: effect of the effusion pressure drop

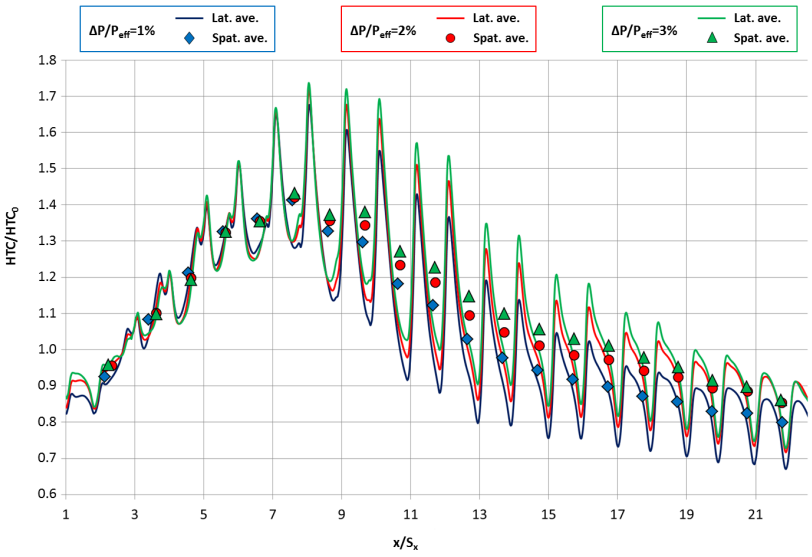

Figure 5.9: Laterally averaged HTC distributions varying the effusion mass flow rate ($W = 0\%$)

behaviour can be ascribed to the acceleration of the impinging jet near the wall in the region downstream of the stagnation point, which results in high axial velocity gradients that tend to drag the coolant injected by the holes, limiting the jets penetration.

In order to consider the injection of coolant from the slot realized on the heat shield, the bi-dimensional distribution achieved imposing the reference cooling condition ($\Delta P/P_{eff} = 3\%$ and $W = 3\%$) is showed in Fig. 5.10right. For a direct comparison, the map with the same effusion pressure drop and the slot system disabled is again reported (Fig. 5.10left).

As a general result, also in this case the map main characteristics are not subjected to severe modifications. The presence of the slot coolant causes a brief enhancement in heat transfer just in the very first part of the plate $x/S_x < 2$, due to initially high slot coolant jet momentum. From this point an overall reduction of the heat transfer is visible up to mainstream jet impinging region. Moving to the final portion of the liner, the effect of the slot tends to be negligible, as already pointed out by the flow field investigation.

Impact of the slot system is evaluated also through the laterally aver-

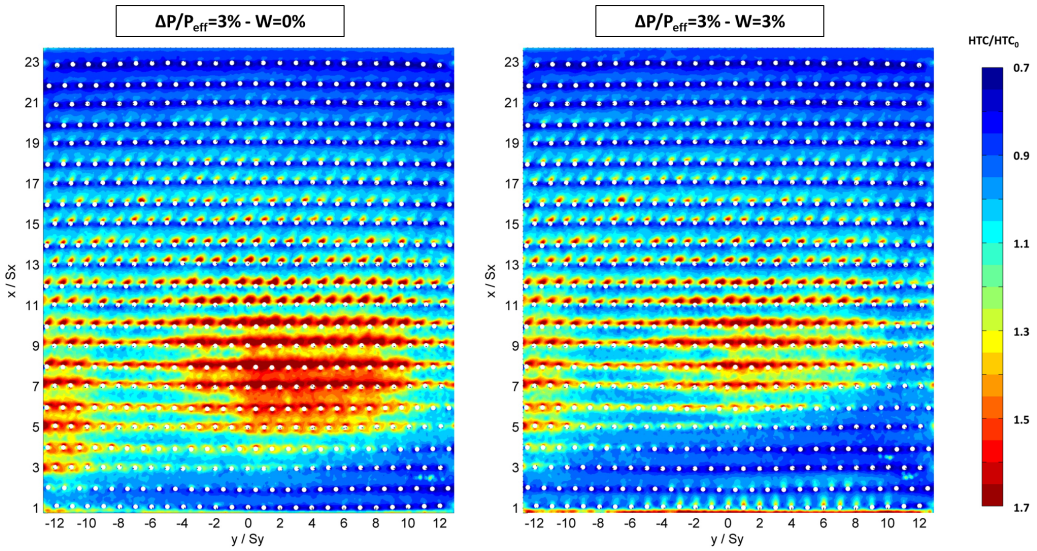

Figure 5.10: 90*deg* liner HTC distributions: impact of slot cooling

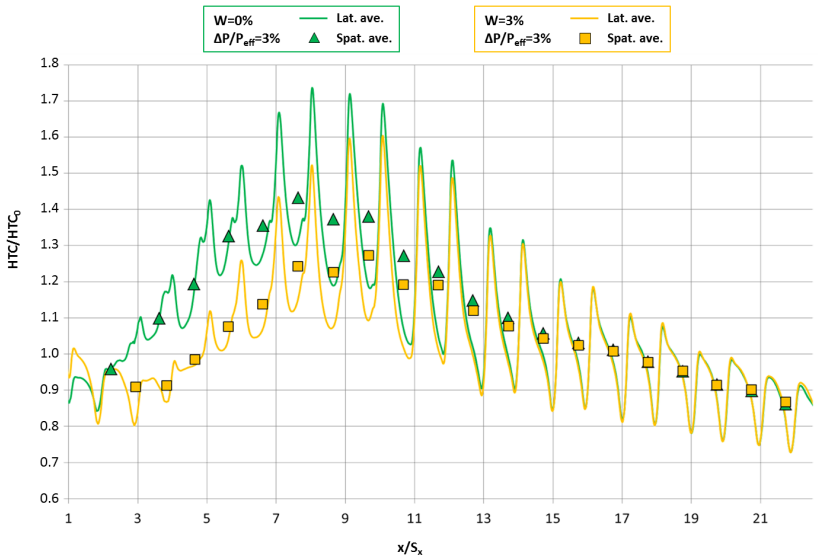

Figure 5.11: Laterally averaged heat transfer coefficient distributions: impact of slot cooling ($\Delta P/P_{eff} = 3\%$)

aged trends of Fig. 5.11. The slot coolant inhibits the heat transfer up to $x/S_x \approx 11$, with a maximum difference of about the 20% with respect the system operating with only the effusion injection. As expected the peak location due to the mainstream jet impingement is moved slightly downstream, consistently with the reduction of the jet aperture angle observed by means of PIV.

5.2.1 Geometries comparison: impact of the injection angle on heat transfer

The uniform injection of coolant from the effusion array and the mixing with the main flow near the wall is governed by complex and unsteady structures, which are expected to lead to a general enhancement of the heat transfer with respect to the smooth plate baseline case with no coolant injection. The previously introduced results for $90deg$ are hence compared with the HTC distributions evaluated for the smooth liner [13] and the $30deg$ geometry [71].

Fig. 5.12 reports the laterally averaged trends for the three investigated

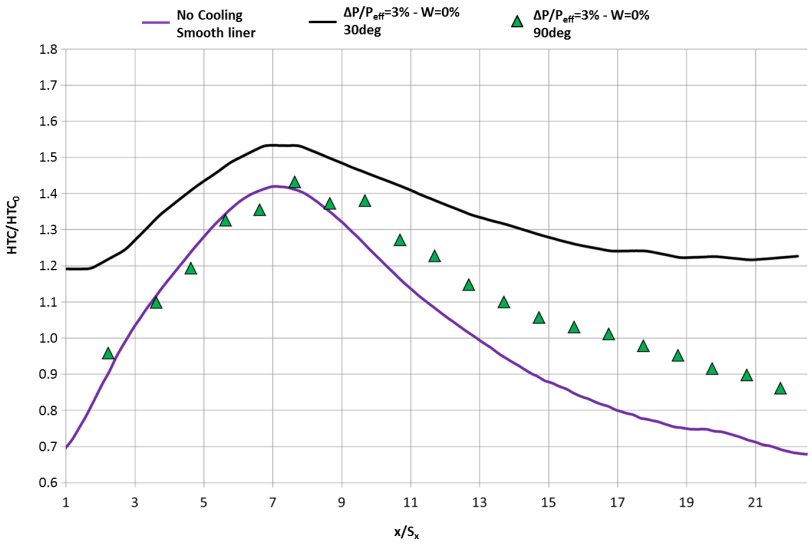

Figure 5.12: Laterally averaged heat transfer coefficient distributions: impact of the holes injection angle ($\Delta P/P_{eff} = 3\%$ and $W = 0\%$)

test plates, the smooth liner distribution refers to the no-cooling condition, whose HTC bi-dimensional map is reported in Fig. 5.7, while for the two multi-perforated plate the effusion pressure drop is set at the 3%. Slot cooling is comprehensibly disabled for all the three tests.

In the first part of the liner upstream of the jet impingement ($x/S_x < 7$) the $90deg$ reveals an analogous behaviour with respect the baseline configuration. In this region the low velocity main flow field seems to facilitate the jet penetration provided by the orthogonal injection, entailing a negligible effect on the liner thermal balance. Downstream of the stagnation point, the interaction between the accelerating main flow, with high axial velocity components, and the effusion coolant appears more intense near the wall leading to a general increase of the heat transfer coefficient. A slight shift of the HTC peak is also observed.

The $30deg$ configuration supplies a significant enhancement of the heat transfer on the whole liner with respect to the $90deg$ liner. The minimum gap between the two effusion schemes is located in the proximity of the jet impingement region, corresponding to the HTC peak: here the flow field structures generated by the impingement of the swirler jet are predominant with respect to the impact of the effusion injection. In the initial part of the liner, the slanted injection leads to the development of strong mixing phenomena, promoting the heat transfer and leading to a 70% HTC increase. This behaviour, coupled with an expected moderate adiabatic effectiveness in this region, emphasize the necessity of a slot system to improve the film covering and consequently to reduce the heat load.

In order to highlight the different impact of the slot system on the three configurations, the slot enhancement factor curves are showed in Fig. 5.13. 1D trends are evaluated as the ratio between the laterally averaged HTC distributions achieved in presence and in absence of the slot coolant injection. For the $30deg$ geometry, the slot injection has a limited impact on the liner heat transfer, registering an almost constant trend around the unit value. On the other hand, for the smooth liner and the normal injection plate, the slot has a similar impact on the heat load with a significant reduction (-20%) of heat transfer at about $x/S_x = 4$. Results confirm previously stated findings:

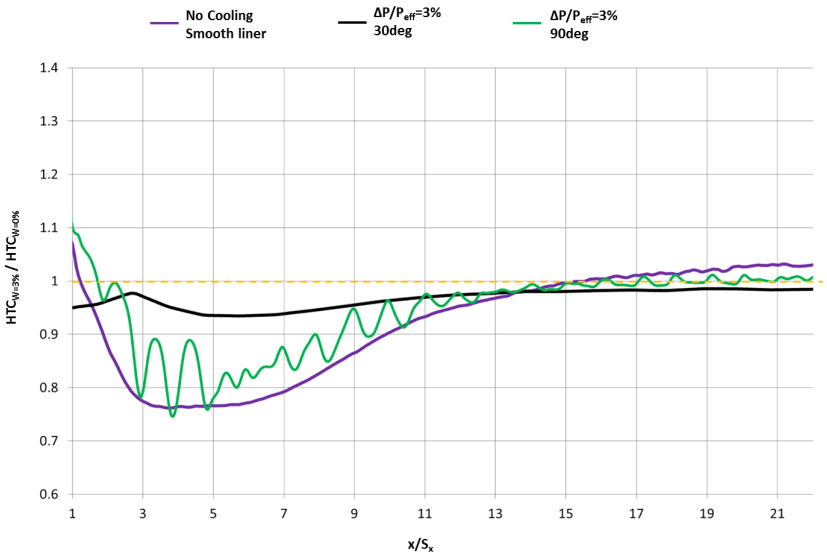

Figure 5.13: Laterally averaged HTC distributions: impact of slot injection

the effusion system with inclined angle governs the flow field near the wall reducing the impact of the slot system, while the normal holes, generating high penetrating coolant jets, move the vortical structures, generated by the mainstream and coolant interactions, far from the plate surface with the consequence of reducing the heat transfer enhancement and hence to obtain an effect of the slot system close to the behaviour registered in the smooth plate configuration. For $x/S_x > 13$ effect of the slot is negligible, with all the three curves tending asymptotically to 1.

To support the validity of the survey, a comparison of the results with works performed by the author's research group within previous European Research Projects is reported in Fig. 5.14. The heat transfer enhancement factor parameter EF, evaluated as the ratio between HTC values achieved in presence and in absence of cooling, is selected to highlight the effect of the effusion injection on heat transfer. In the works considered for the comparison, heat transfer measurements are carried out with uniform mainstream conditions (no swirled gas flow) and employing effusion cooling schemes with the same hole perforation of the present campaign. In detail, data reported by Facchini et al. [98] are obtained within the NEWAC project exploiting

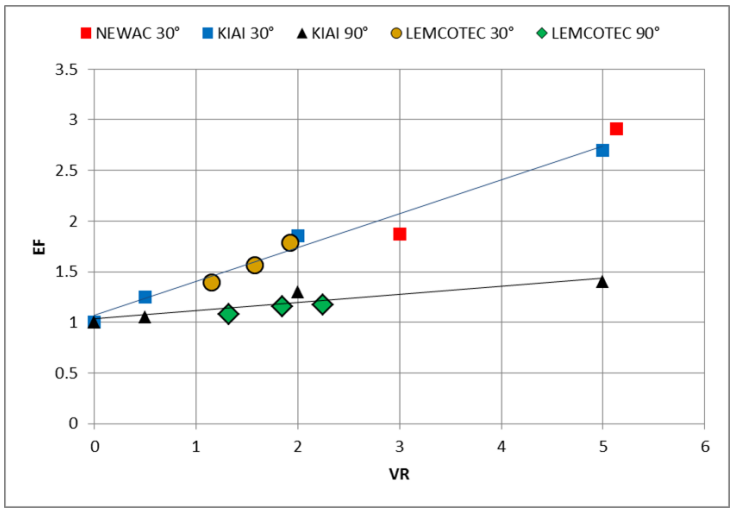

Figure 5.14: HTC results comparison within different experimental campaign

the well-known steady-state TLC technique on a $30deg$; while a coupled experimental/numerical approach is employed by Andreini et al. [58] on two cooling geometries ($\alpha = 30deg, 90deg$) investigated within the KIAI project.

In order to provide a meaningful comparison, for the present work, EF data are calculated near the test section exit ($x/S_x = 22$) where the influence of the swirling main flow in proximity of the liner wall is minimum. VR values are evaluated considering an uniform coolant extraction provided by the effusion liner alongside the entire plate.

For all the three levels of effusion mass flow rate, both the two geometries show good agreement with previous results, confirming the increase in the heat transfer augmentation enhancing the velocity ratio. As expected, orthogonal injection data points lie on a less sloped line, due the higher penetration of normal jets that moves the interaction with the mainstream, and therefore the related vortical structures responsible of a greater convection, far from the plate surface.

5.3 Film cooling effectiveness

In the present activity, the experimental investigation aimed to estimate the adiabatic effectiveness using PSP technique is carried out on the two liner configurations identified with holes inclination angles of $90deg$ and $20deg$. Tests are conducted imposing the swirlers pressure drop at the reference condition of $\Delta P/P = 3.5\%$. Effusion mass flow rates are set on the basis of multi-perforated plates pressure drop: three conditions are investigated corresponding to $\Delta P/P_{eff} = 1\%, 2\%, 3\%$. For each geometry, one test with slot cooling enabled is carried out in concurrence of the maximum level of effusion injection.

All the results reported in this work are normalized by means of a reference value $\eta_{ad,0}$, representing the spatially averaged adiabatic effectiveness value obtained for the reference cooling condition employing the $30deg$, with both the cooling systems activated. The investigation area is the same of the HTC maps, as well as the non-dimensionalization of the axis.

5.3.1 $90deg$ liner configuration

In Fig. 5.15 are depicted the adiabatic effectiveness maps obtained for the $90deg$ plate varying the effusion pressure drop with the slot system disabled.

As a general results, the distributions are characterized by a central region ($5 < x/S_x < 9$) with low effectiveness, that corresponds to the zone with high heat transfer values. Here the coolant traces are subjected to a strong lateral spreading, prompted by the unsteady flow structure and by the high turbulence level generated by the impingement of the swirler jet. Downstream of this region, superposition effects allow to achieve a significant, rather uniform, film covering in the final part of the liner, where the flow field near the wall is less affected by the mainstream.

Thanks to the high resolution of the results it is possible to observe that coolant is slightly deviated towards the right hand side of the test section, this tendency is coherent with the sense of rotation impressed to the main flow by the three swirlers. In the first part of the geometry for $x/S_x < 6$

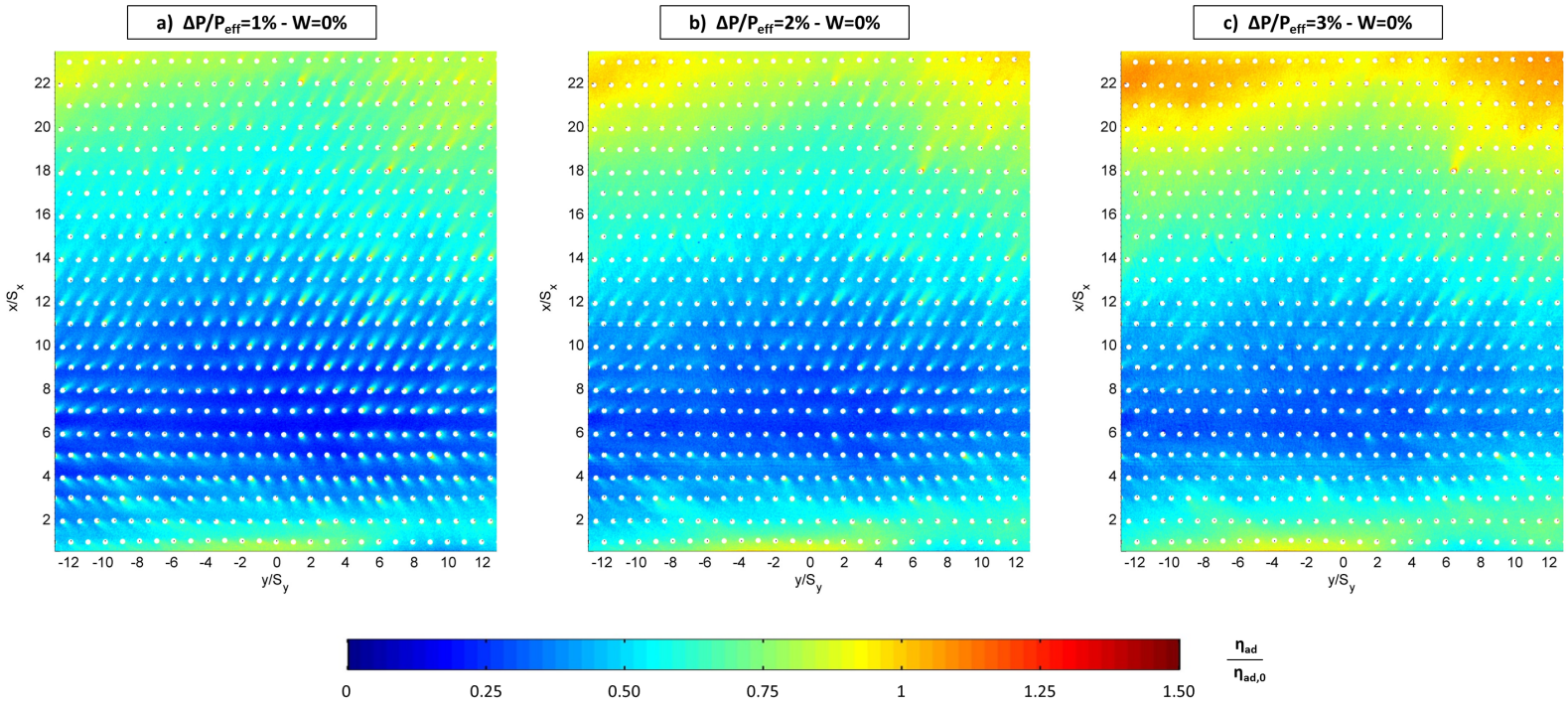

Figure 5.15: 90*deg* adiabatic effectiveness maps: effect of the effusion pressure drop

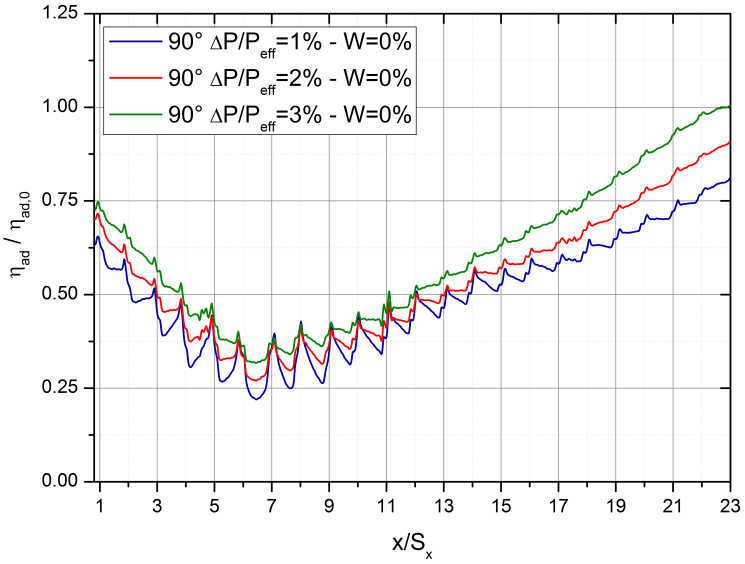

Figure 5.16: Laterally averaged adiabatic effectiveness distributions: impact of effusion pressure drop ($W = 0\%$)

coolant traces are directed in the opposite way with respect the streamwise direction, achieving film covering upstream of the injection. This peculiar behaviour is due to the action of the corner vortex structure observed during the PIV test campaign, which lead to negative axial velocity components near the liner.

A moderate impact of increasing the effusion pressure drop is highlighted on almost the whole liner and is confirmed by the laterally averaged trends of Fig. 5.16. A spatially mean enhancement up to 20% is achieved increasing the pressure drop from 1% to 3%.

Maps of Fig. 5.17 allow to appreciate the effect of the slot injection in terms of film covering and its interaction with the effusion array. The first 2D distribution (Fig. 5.17a) is obtained in absence of effusion flow, plugging the holes array on the cold side, in order to avoid air ingestion, and imposing the reference slot coolant consumption $W = 3\%$: impact of the slot cooling, in term of film protection, is very intense but is, however, confined in a limited region at the liner inlet ($x/S_x < 2$). The slot generates a non-symmetric film

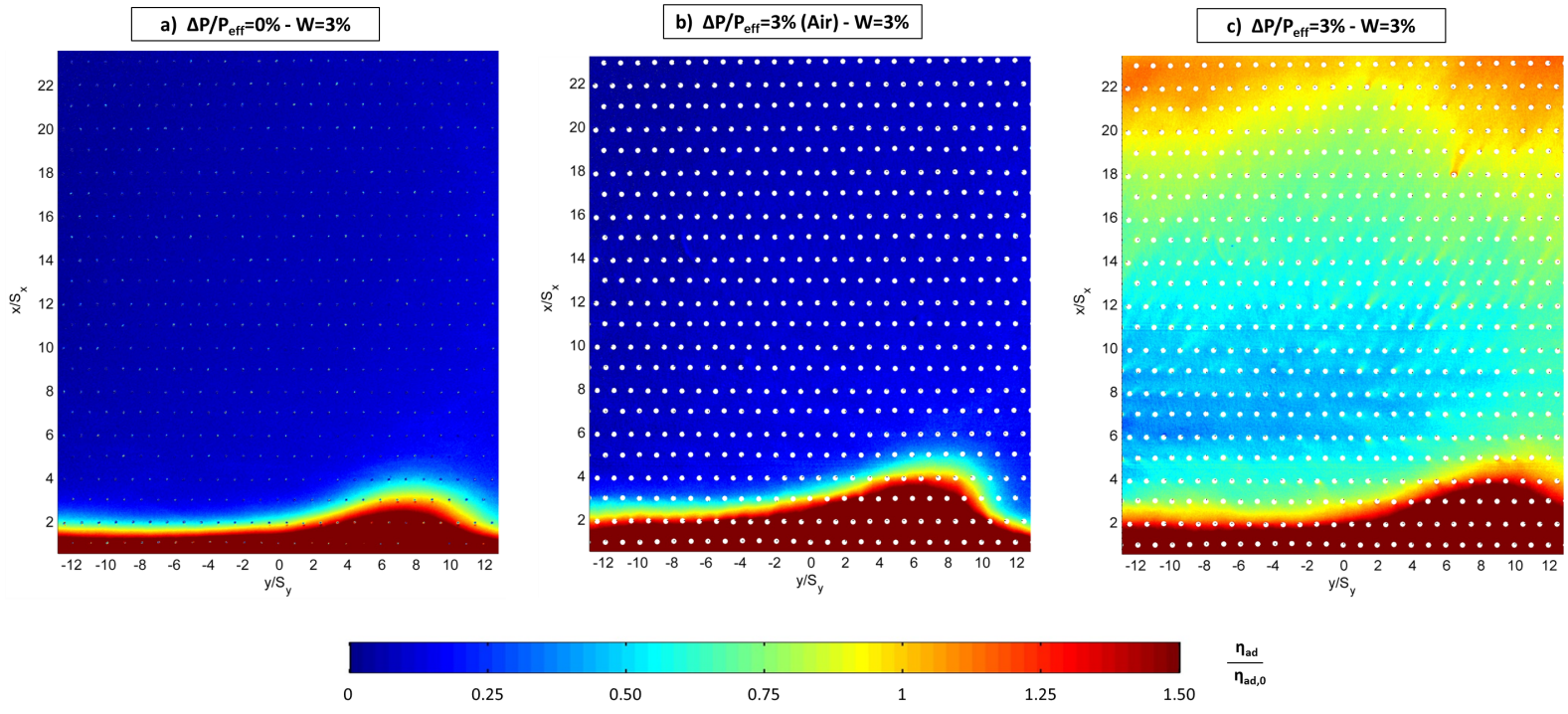

Figure 5.17: 90*deg* adiabatic effectiveness maps: impact of slot cooling

distribution in tangential direction, in agreement with the test section flow field near the wall, registering high η_{ad} values up to the 3rd row on the right side of the liner ($6 < y/S_y < 9$).

Distribution reported in Fig. 5.17b is useful to decouple the slot contribution from the effusion flow. Test is performed at the reference cooling conditions ($\Delta P/P_{eff} = 3\%$ and $W = 3\%$) but using Nitrogen only for the slot coolant, while air is employed to feed the effusion system. This set up allows to estimate only the slot contribution to film protection, but taking into account the fluid dynamic effect of the liner perforation. An advantageous effect on the cooling system is observed with a moderate increase of the extent of slot covering region: effusion array seems to be able to rather energize the coolant flow structure exiting from the slot.

The last map (Fig. 5.17c) is carried out at the same flow conditions of test *b*, but employing typical Nitrogen injection for both the cooling lines. Same extension of the high film protection region produced by the slot is achieved, furthermore coolant exit is less affected by the test section flow field with a more constant behaviour alongside the y direction.

Laterally averaged trends of Fig. 5.18 clearly confirm the capability of the effusion system fed with air (*red line*) to energize the slot coolant and to shift downstream its protection, although not directly concurring to film covering. This effect is detectable up to $x/S_x \approx 5$, thereafter the slot film layer is completely destroyed by the main flow field. No differences are observed for $x/S_x < 2.5$ changing the effusion supply from air to Nitrogen (*yellow line*), highlighting the predominant role of the slot in the very first part of the liner. Downstream of this point, contribution of the effusion takes the control of the film performance, however the presence of the slot system leads to a general enhancement in η_{ad} with respect to the test with only the effusion active (*green line*), this effect is progressively decreased approaching the liner exit.

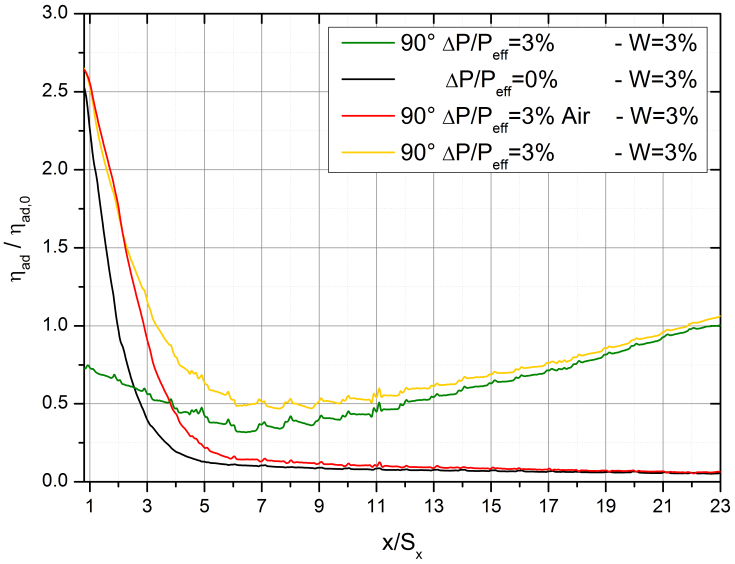

Figure 5.18: Laterally averaged adiabatic effectiveness distributions: impact of slot cooling

5.3.2 $20deg$ liner configuration

Deep modifications in the liner film covering are observed moving from an orthogonal injection to an highly inclined configuration such as the $20deg$ plate. Analogously to previous geometry, the impact of the effusion pressure drop on the cooling performance, with the slot disabled, is investigated and results are presented by means of normalized η_{ad} in Fig. 5.19.

Well-known low protection area is established in the jet impingement region also for this configuration. The $\Delta P/P_{eff}$ increase leads to a general and diffused enhancement in film protection. For the first rows of holes, the limited jet penetration of the lower VR condition drives to more intense coolant traces. On the other hand, in the stagnation region, high VR cooling jets are the only able to resist to the coolant washing action promoted by the impinging mainstream flow. Thanks to the strong exploitation of superposition effect, extremely high values are obtained at the test section exit for the maximum effusion mass flow rate.

As usual, the laterally averaged trends are also reported. Fig. 5.20

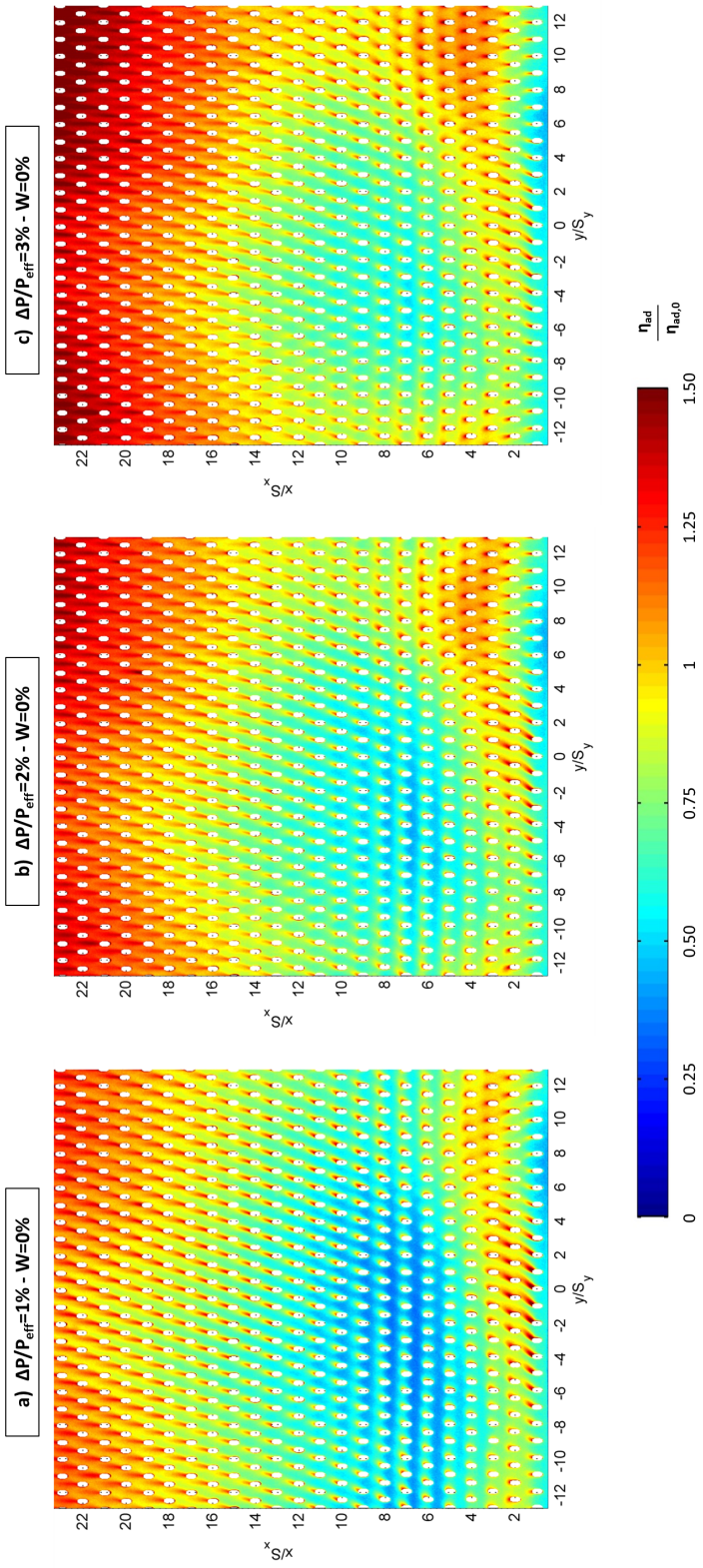

Figure 5.19: $20deg$ adiabatic effectiveness maps: effect of the effusion pressure drop

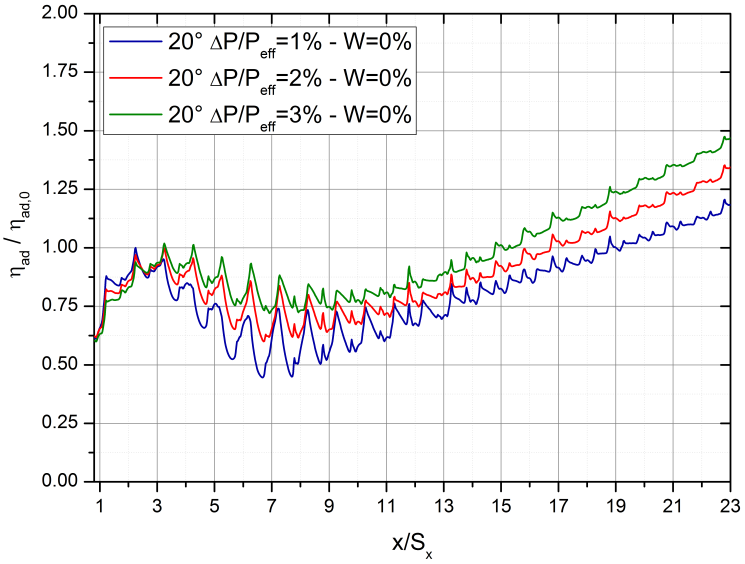

Figure 5.20: $20deg$ laterally averaged η_{ad} distributions: impact of effusion pressure drop ($W = 0\%$)

confirms aforementioned findings and clearly highlights the adiabatic effectiveness reversal behaviour up to $x/S_x = 2.5$, while downstream the $\Delta P/P_{eff} = 3\%$ curve achieves higher and more uniform values.

The beneficial effect of effusion cooling on slot injection denoted by the orthogonal array is amplified by the tilted injection of the $20deg$ plate as showed in Fig. 5.21. Employing the same set-up with air feeding the effusion system and Nitrogen the slot plenum, Fig. 5.21b highlights a significant lengthening of the high film covering region. Furthermore the map results less affected by the main flow field, with a more uniform distribution alongside the y direction. Fig. 5.21c shows all the potential of the $20deg$ configuration, almost the entirely liner surface registers a good film protection: in this case slot injection is providential in the first part of the liner, where high inclined holes with elevated VR values have proven to be subjected to a strong penetration.

Not particular differences with respect to $90deg$ are observed in terms of trends shaping in the 1D distributions of Fig. 5.22. Slot reinforces its predom-

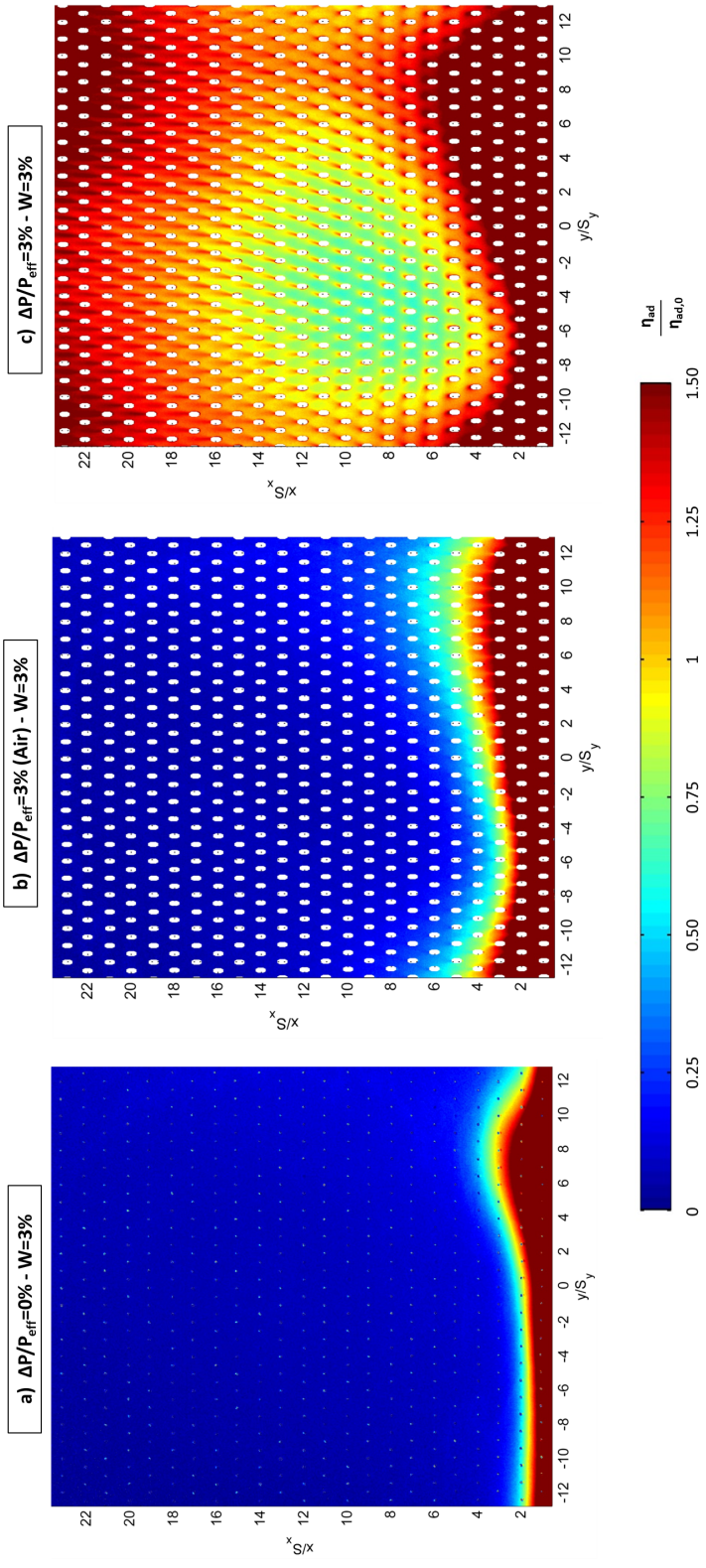

Figure 5.21: 20*deg* adiabatic effectiveness maps: impact of slot cooling

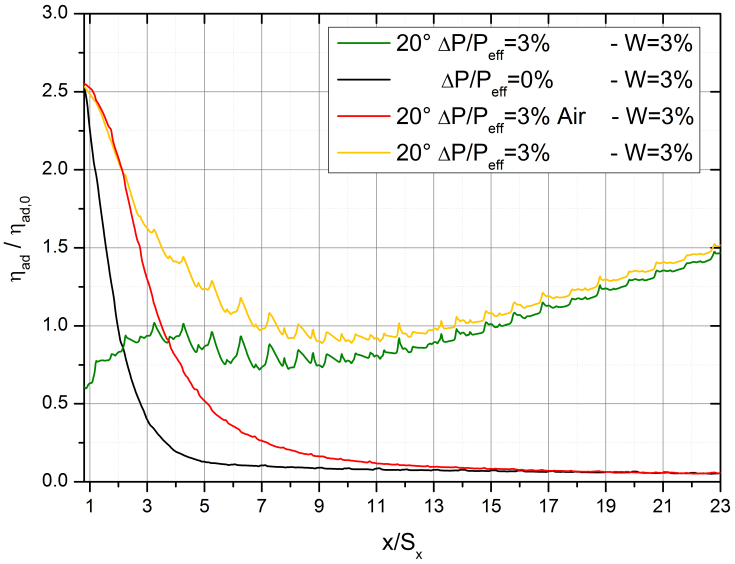

Figure 5.22: Laterally averaged adiabatic effectiveness distributions: impact of slot cooling

inant role in the early regions of the liner, with the augmented momentum supplied by the slanted injection, while at high x/S_x values an almost negligible effect is addressed.

5.3.3 Geometries comparison: impact of the injection angle on film covering

To finalize the adiabatic effectiveness analysis, a direct comparison of the results for the three liner geometries investigated within the LEMCOTEC project is reported. Fig. 5.23 show the 2D maps achieved under two different cooling conditions: only effusion injection set at $\Delta P/P_{eff} = 3\%$ and reference cooling condition with both the systems enabled ($\Delta P/P_{eff} = 3\%$ and $W = 3\%$).

All maps are characterized by the non-symmetric central region with low effectiveness, corresponding to the stagnation region of the impinging jet

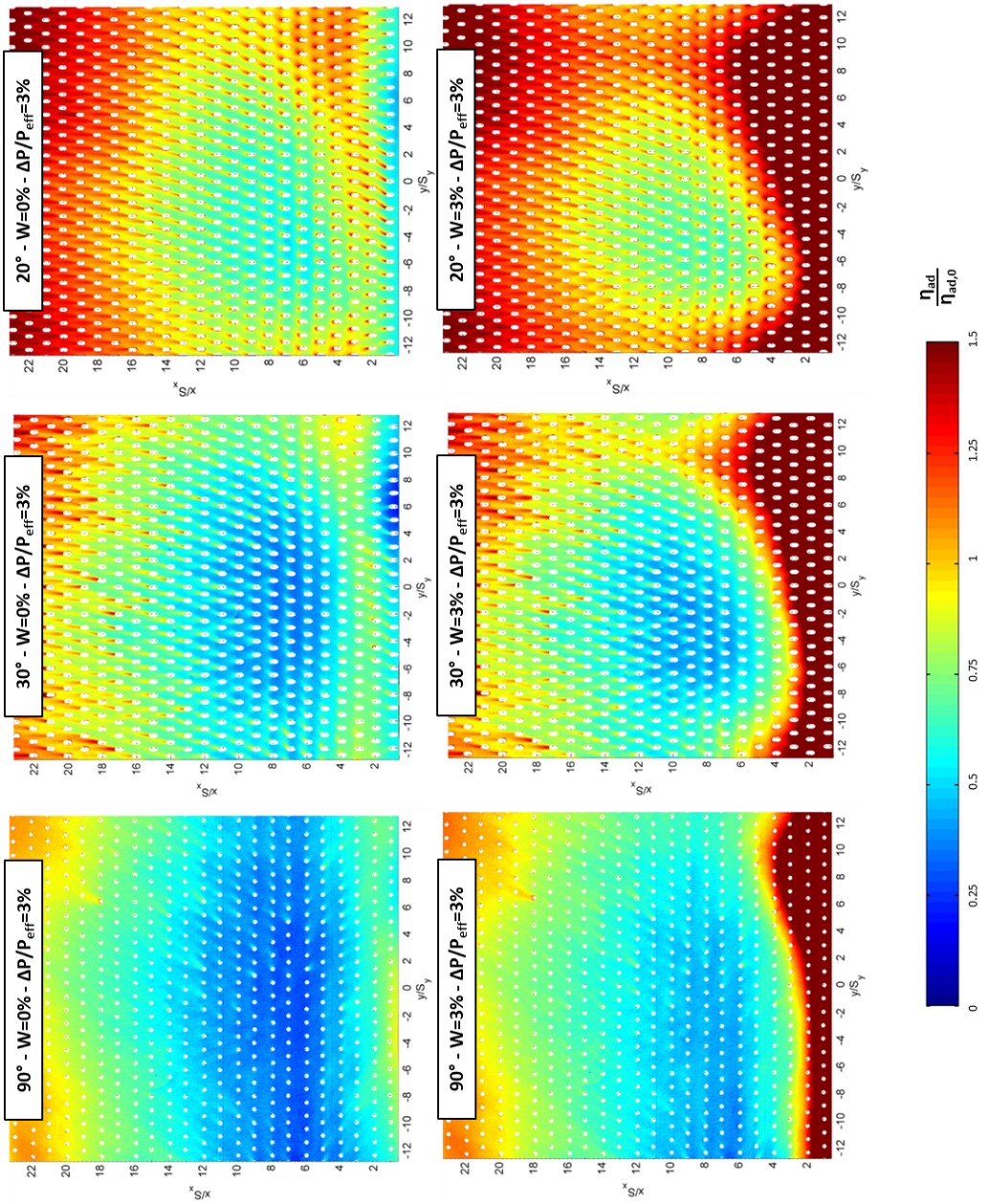

Figure 5.23: Adiabatic effectiveness maps: geometries comparison varying cooling conditions

highlighted by the PIV measurements. It is also worth to notice that probably part of the coolant is entrapped in the dome recirculation structures and is responsible of generating a strike with high effectiveness between about $y/S_y = 7$ and $y/S_y = 11$.

As expected, the best film covering is achieved by the geometry with the lower inclination angle, where the coolant slant injection is capable to limit jet penetration and exploit superimposition effects. Thanks to the high resolution of the results is possible to appreciate the different shaped traces, with longer and more defined coolant imprints for $20deg$ geometry, and partially for $30deg$ inclined holes, while for the perpendicular array coolant traces appear less coherent and more susceptible to mainstream flow field.

The importance of using the slot system to start the film protection is clearly stated in the bottom distributions with an high film protection region obtained for $x/S_x < 3$. The role of slot cooling is appreciable up to the jet stagnation point, while approaching the liner plate exit its effect is almost negligible.

For a more quantitative analysis, the laterally averaged distributions of adiabatic effectiveness are reported in Figure 5.24. Taken for granted the increase in film covering varying the effusion pressure drop from 1% to 3%, similarly shaped curves are obtained for all the tested conditions. Minimum adiabatic effectiveness values are clearly detected in the jet stagnation region ($x/S_x \approx 7$) due to the high turbulence level generated by impingement phenomena that tends to destroy the film covering and to lift up the effusion flow. Downstream, superimposition effect leads to an almost linear growth of η_{ad} allowing to guarantee sufficient film protection also for low effusion mass flow rates.

Results confirm the superiority of the $20deg$ geometry in almost all the liner, with the gap versus the other configurations that tends to increase enhancing the $\Delta P/P_{eff}$. With respect to $30deg$ angle, a mean gain of about 30% is achieved in terms of averaged effectiveness by the most inclined injection. In the very first part of the liner ($x/S_x < 2$) good results are obtained by the $90deg$ configuration due to the presence of reverse flow near the liner, that leads to upstream film covering produced by the first rows of holes. In

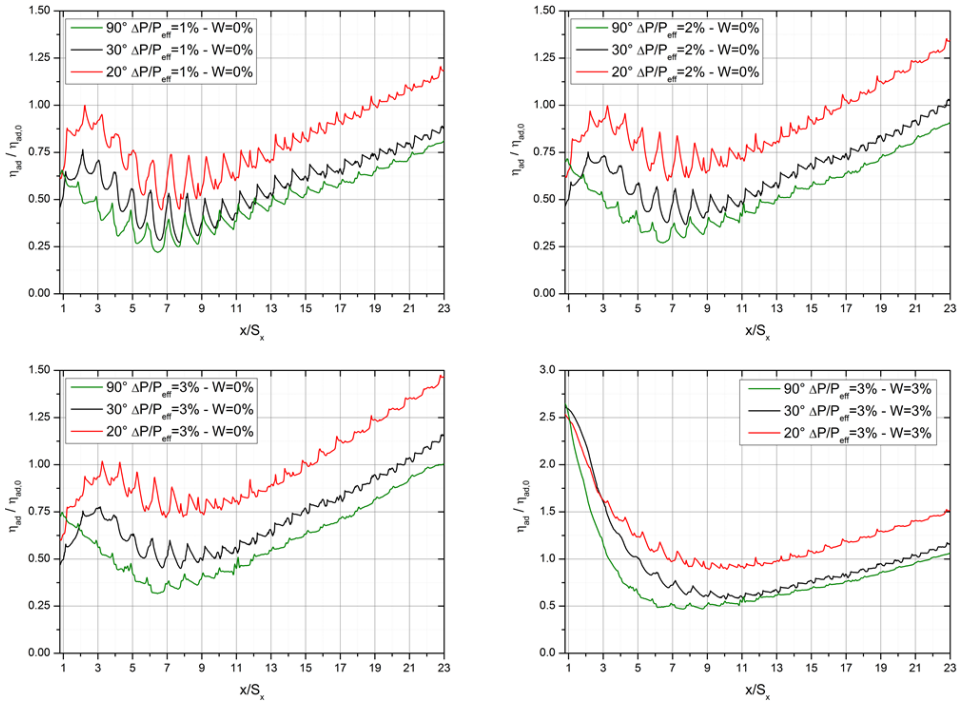

Figure 5.24: Laterally averaged η_{ad} distributions: comparing different geometries

this short initial region the $30deg$ configuration is particularly suffering at high VR conditions with an averaged decay in $\eta_{ad}/\eta_{ad,0}$ up to 15% with respect the orthogonal perforation.

Distributions concerning the test with slot coolant injected, report approximately unitary values at the liner entrance with the $30deg$ plates showing the best results up to $x/S_x = 3$. The differences between the film protection generated by the $30deg$ and $90deg$ inclination angle are high in the first part of the liner ($x/S_x < 9$), while downstream the values are almost comparable. A considerable increase in film protection is achieved by the $20deg$ geometry: for $x/S_x > 10$ a nearly constant gap of about $\eta_{ad}/\eta_{ad,0} = 0.4$ is maintained with respect the other configurations.

5.4 Cold side heat transfer

The above-discussed results, deriving from the experimental investigation performed on the three sector test rig, show a significant impact of the combustion chamber flow field and of the holes injection angle on an effusion cooling scheme. New multi-perforated plates with $\alpha = 90deg$ and $\alpha = 20deg$ are analysed and compared to the LEMCOTEC project $30deg$ reference configuration. To assess a complete characterization of this geometry a supplementary survey is carried out on a dedicated test rig, focusing to the measurements of the annulus cold side heat transfer coefficient. Results are here presented by means of Nusselt number maps and 1D distributions, in addiction a data reduction is employed in order to propose a correlation for the prediction of the cold side heat transfer enhancement factor EF.

Fig. 5.25 shows Nusselt number maps for the five different ByR conditions reported in Table 4.2 in case of a pressure drop across the liner equal

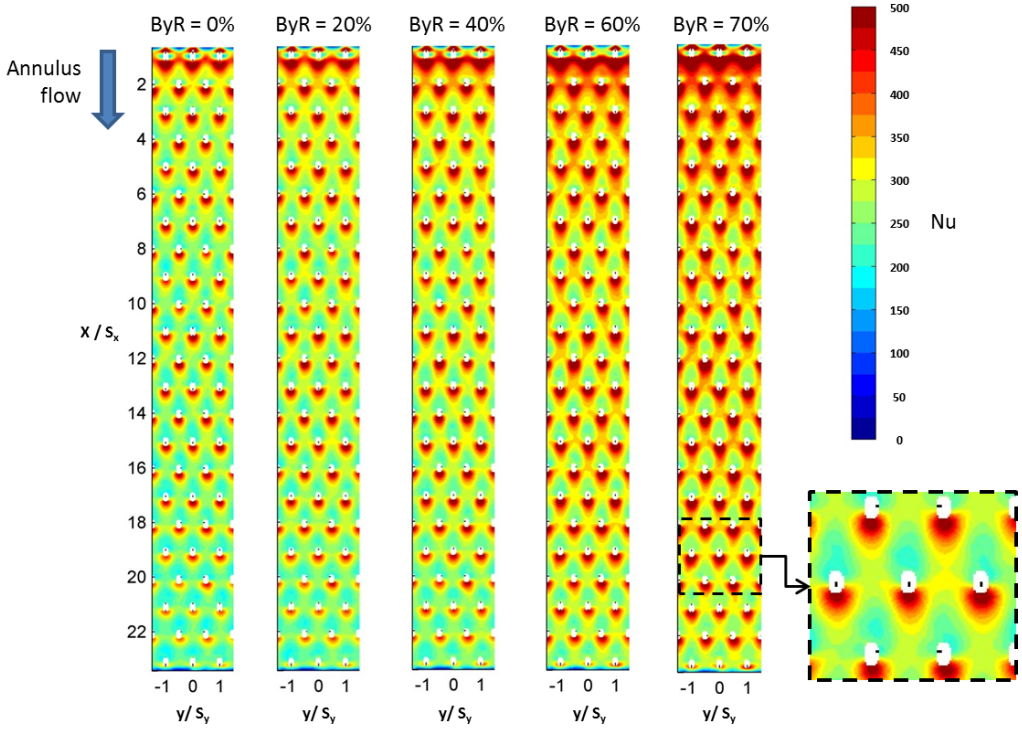

Figure 5.25: Nusselt number maps varying the ByPass ratio($\Delta P/P_{eff} = 3\%$)

to $\Delta P/P_{eff} = 3\%$. The reported area of interest concerns of a central longitudinal portion of liner with a width of $3S_y$ and includes all the 23 rows of holes. Immediately downstream of the plate inlet, maps reveal slight edge effects where an incomplete activation of the TLC is registered.

As a general result, Nusselt number distributions reveal peaks immediately downstream of the effusion holes. This effect can be attributed to local impingement phenomena generated by the annulus flow which, due to the coolant extraction, deviates in proximity of the cooling holes and generates a stagnation region. This phenomena has been already documented in the open literature for isolated hole as reported by Byerley et al. [76]. Maps indicate also that rising the level of bypass flow inside the annulus channel causes an homogeneous increase of the heat transfer coefficient. This is mainly due to an increase of Reynolds number of the flow inside the annulus moving from $Byr = 0\%$ to $ByR = 70\%$.

The zoomed view of Fig. 5.25 shows a moderate increase of heat transfer coefficient also in the areas located between the consecutive stagnation regions and inclined with respect to the main flow direction. This effect can be attributed to the interaction of the coolant extract by adjacent holes and promoted by the staggered position of the effusion array.

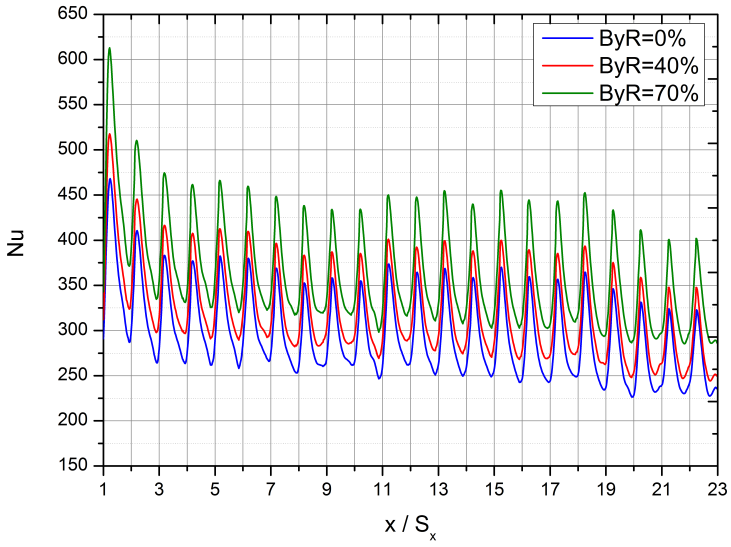

Figure 5.26: Nusselt number 1D distributions varying $ByR(\Delta P/P_{eff} = 3\%)$

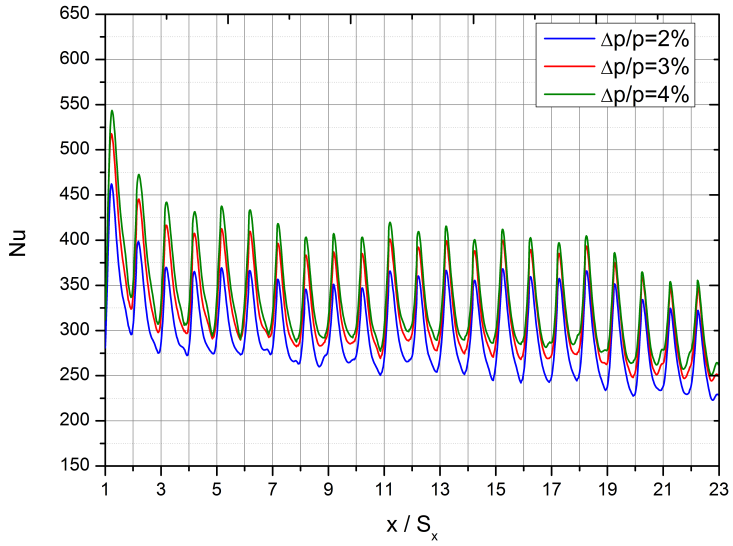

Figure 5.27: Nusselt number 1D distributions varying $\Delta P/P_{eff}$ ($ByR = 40\%$)

In Fig 5.26 the lateral averaged Nusselt number distributions are reported for three of the five conditions investigated at $\Delta P/P_{eff} = 3\%$. Trends confirm the presence of relevant peak values of Nusselt number immediately downstream of the extraction and lower values upstream. The shape of the curves are not affected by the level of the bypass flow. For all the three conditions, an almost constant behaviour is observed between the different rows of holes in the range from $x/S_x = 3$ to $x/S_x = 18$. Thereafter Nu tends to slightly decrease approaching the plate exit.

To understand the role of the effusion pressure drop on the Nusselt number distribution, in Fig 5.27 are depicted the laterally averaged Nusselt number distributions achieved with a constant value of $ByR = 40\%$ for three different values of the pressure drop across the liner. An enhancement in $\Delta P/P_{eff}$ parameter leads to a general increase of the heat transfer coefficients due to the increase of annulus Reynolds number. Moreover, the pressure drop produces and increase of the ratio between higher and lower Nusselt number values across each row of holes.

In order to provide a global view of the results, Fig. 5.28 reports all the test points in terms of spatially averaged EF calculated row by row as a function of local SR. The trends clearly reveal that the pressure drop, which

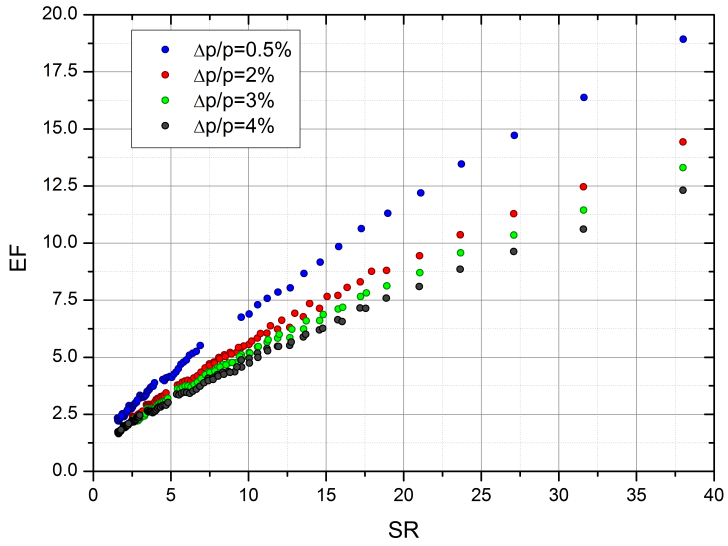

Figure 5.28: Enhancement Factor as a function of SR

in turns can be related to the annulus Reynolds number, reduces the EF for all the SR tested. Recalling that the reference Nusselt number Nu_0 used to define the EF parameter is directly proportional to $Re^{0.8}$, the plot indicates that the relation between Nusselt and Reynolds number is characterised by an exponent less than 0.8 as confirmed in the technical literature also for other heat transfer augmentation scheme such as pin fins and impingement.

Finally, approaching $SR = 0$ (no coolant extraction), distributions tend to $EF = 1$ condition, pointing out an experimental Nusselt number extremely close to those obtained with Colburn correlation.

Effects of the extraction of the coolant from the annulus provide a significant contribute to the liner thermal management, it's hence fundamental in the preliminary design of an effective effusion cooling scheme taking into deep account this aspect. For this reason, a possible correlative approach is proposed, exploiting a data reduction strategy for all the test conditions. In detail, the results are re-casted in terms of area averaged EF calculated row by row as a function of the local value of the Reynolds number and the Suction Ratio.

From the analysis of the results, it can be assumed the following relation-

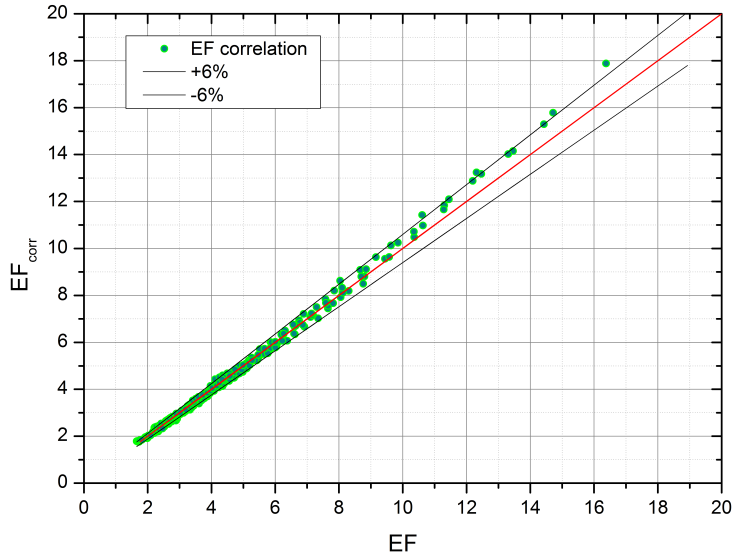

Figure 5.29: Enhancement factor correlation

ship with the main flow parameters:

$$EF = 1 + a \cdot Re^b \cdot SR^c \tag{5.1}$$

The expression is equal to 1 when no coolant extraction phenomena is observed, i.e. Suction Ratio equal to zero.

Using a least square mean method approach to the whole set of experimental data, the values of the fit parameters reported in Eq. 5.1 assume the following values:

$$a = 166.5 \quad b = -0.47 \quad c = 0.40 \tag{5.2}$$

95% of the experimental data are fit by the proposed correlation within ±6% and with an average error of 2.5% (Fig. 5.29). The expression confirms a significant reduction of the EF when Reynolds number increases and a strong dependence with the Suction Ratio parameter. No extrapolation of presented equation is feasible, rather its use may be significant only within the selected range of input parameters.

5.5 Concluding remarks

The extensive experimental survey allows to obtain a broad data set useful to deepen the knowledge of a combustor liner thermal balance and to support possible cooling scheme optimizations. In spite of cold non-reactive conditions, PIV investigation revealed a good capability to catch lean combustors flow field, highlighting all typical flow structures generated by the swirlers [30]. Furthermore tests were performed replicating main similarity parameters for the cooling system, allowing to scale with reasonable accuracy the HTC and η_{ad} results to engine conditions in order to support the preliminary design of advanced cooling schemes.

To summarize the thermal performance of the investigated liner configurations and to combine the results in terms of heat transfer augmentation factor (Section 5.2) and film covering (Section 5.3), the laterally averaged trends of $NHFR$ are reported in Fig. 5.30 for the $90deg$ and the reference $30deg$ effusion plates. $NHFR$ represents a powerful parameter to evaluate the reduction of heat flux across the external cooled surface with respect of the baseline situation, however it can not be used to perform a proper comparison between different effusion arrangements because it does not take into account the contributions of heat sink effect and of the coolant extraction on the liner cold side, which play both a significant role in lowering the metal temperature.

$$NHFR = 1 - \frac{HTC_{main}}{HTC_0}\left(1 - \eta_{ad} \cdot \theta\right) \tag{5.3}$$

The dimensionless temperature θ is calculated using temperature values representative of a real lean-burn combustor, obtaining $\theta = 1.2$.

Regarding the curves without slot injection, the effect of the effusion pressure drop appears to be negligible alongside the whole liner for the $90deg$ plate. Also the $30deg$ registers three similar distributions, except for the entrance region and the zone $12 < x/S_x < 18$. Here, despite the effusion pressure drop is able to enhance the film covering, the increase of adiabatic

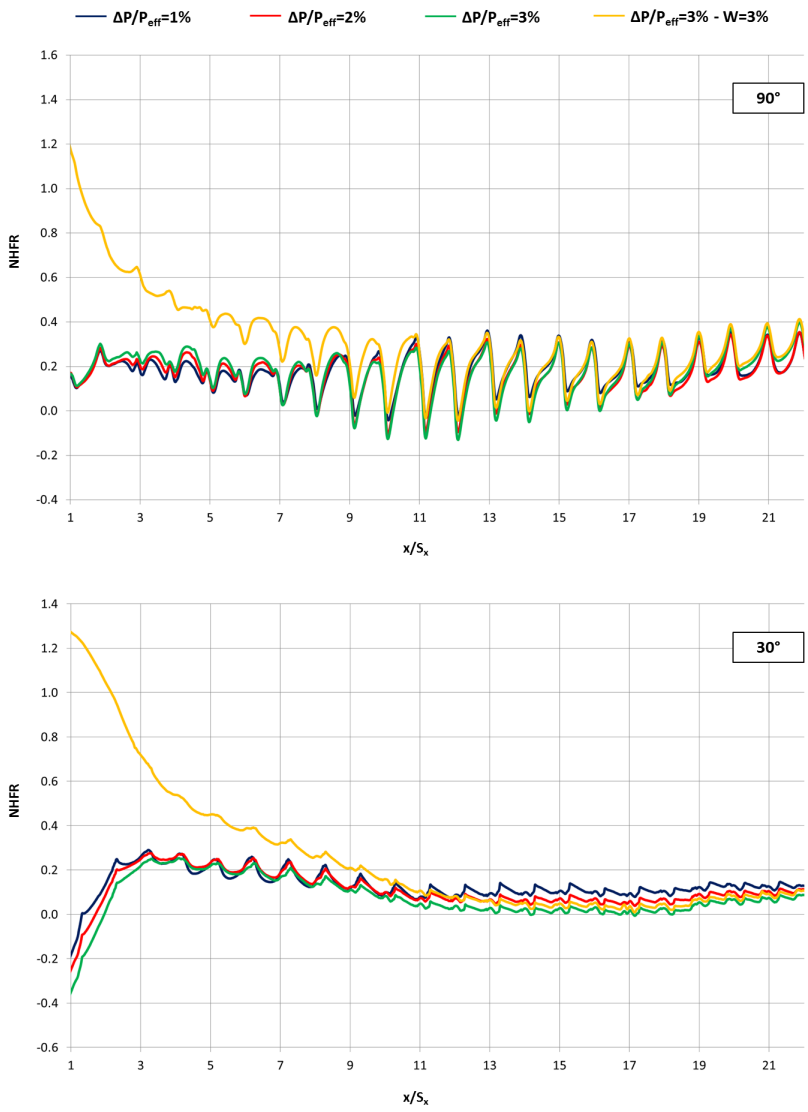

Figure 5.30: Net Heat Flux Reduction distributions for different cooling conditions

effectiveness is not sufficient to compensate the increase of the heat transfer coefficient on the liner surface resulting in a reduction of $NHFR$ parameter moving from $\Delta P/P_{eff} = 1\%$ to $\Delta P/P_{eff} = 3\%$. It's worth to notice that for the inclined geometry, an increased effusion mass flow rate leads even to negative values for $x/S_x < 2$, producing a counter-productive augmentation of surface heat load.

The benefits produced by the use of the slot system to start and improve

the film covering at the inlet of the combustor liner are clearly showed by the $NHFR$ distributions. Values greater than 1, thanks to the high film protection, are reached in the first part of the liner and reduction effect with respect to only effusion injection is protracted up to the 10th rows for both the geometries.

At this point of the work, some conclusive considerations worth to be spent on the performance of the effusion system. Results confirm the absolute requirement of slot coolant injection to guarantee the development of film cooling protection in the first part of the liner. In this region coolant superposition effects are not already arisen and the main flow field, deeply affected by the corner-vortex interactions, obstructs the attainment of an efficient wall cooling by means of the only effusion array. Extending the axial endurance and providing a more uniform film covering on lateral direction represent two essential targets in the improvement process of the slot system. As a general result, effusion coolant injection has proven to have a beneficial effect on slot structure development, energizing and dragging downstream of the coolant flow structure; nevertheless in the very first part of the liner for $x/S_x < 3$ the predominant role is firmly possessed by the high momentum slot jet allowing to eventually reduce the perforation porosity in order to save coolant for other zones of the liner or for the own slot.

The central part of the liner where the the swirling jet impacts the surface is emerged as the most critical region for the cooling scheme. High values of heat transfer coefficient are registered in this area, furthermore the slot coolant is not able to coherently reach it and the high turbulence levels generated by the impinging jet tend to destroy the effusion film covering. An optimization of the liner design must take into account this critical zone: possible solution to keep low the temperature of the component is to enhance the heat sink effect and the cold side heat transfer by increasing the holes porosity maintaining constant the hole diameter, obviously this modification leads to an increase of coolant air requirement.

Approaching the exit of the liner a less critical situation is present, with the inclined holes able to supply a particularly remarkable film protection

thanks to superimposition effect.

Measurements of the cold side heat transfer has highlighted the importance of this contribution in the liner thermal management. In the last years, several authors proposed different methods to enhance the HTC on the annulus side, such as double skin tile cooling or impingement-effusion cooling systems ([99, 100, 101, 102]): all the proposed strategies lead to an increase of the pressure loss on the annulus side and hence to a reduction of the effective pressure drop across the effusion perforation. Following this approach an optimization of the cooling liner based on the results achieved with $\alpha = 30deg$ configuration is reported by author's research group in [103]. In this case, the adoption of a generic optimized scheme with enhancement of the effusion cold side heat transfer allows to reduce the metal temperature of approximately $6 - 8\%$ compared to the standard effusion configuration. Moreover, the coolant amount required is decreased by about 20%, as a consequence of the reduced pressure drop across the perforation. On the other hand, geometries involving a double-wall construction leads to severe penalties in terms of engine weight, manufacturing complexity and costs; to try to partially overcome these issues nowadays one of the most interesting approach is represented by addictive manufacturing.

Chapter 6

Effusion Performance with Reactive Conditions

Contents

6.1 Experimental apparatus 135
6.2 Test conditions 144
6.3 Preliminary results 146

In recent years, Additive Manufacturing (AM) field has been object of continuously increasing interest by aeronautics industry. In particular, methods such as Direct Metal Laser Sintering (DMLS), which employed innovative and robust metal alloys, have showed interesting potentiality in the possible manufacturing of static components subjected to high temperatures such as some of the parts in the combustion chamber. Rapid prototyping technique allows to realize very complex geometries, impossible to be manufactured by traditional methods, greatly broadening the degrees of the design freedom. AM special characteristics meets in full the main future challenges of the aero-engines industry such as components lead time decrease and weight reduction, which in turns leads to lesser fuel consumption and lower emission levels, and by reducing component lead time.

In the context of the technological project IMPACT-AE (Intelligent Design Methodologies for Low PollutAnt CombusTors for Aero-Engines), cofunded by European Commission in the Frame Work 7, Avio Aero and the

University of Florence as its partner, set the goal of developing new design methodologies for combustor components, manufactured by rapid prototyping, and their validation by testing on a combustion chamber sector, specifically designed and manufactured.

Additional goals of the experimental survey are the aerodynamic characterisation of the combustor, through the assessment of the aerodynamic pressure losses and the air-flow split, and the definition of combustion performance, identifying the ignition and stability idle conditions and characterizing the combustor behaviour during the commutation procedure between pilot and main stage.

Activity reported in present dissertation deals with a preliminary experimental survey performed as a part of the commissioning phase of the combustor rig and mainly focused to verify the correct integration in the facility test cell and to establish the convenient operating procedures. Nevertheless, some interesting outputs and useful information can be derived from these first results.

6.1 Experimental apparatus

A cross-sectional sketch of the experimental test rig, called VALIDATOR, is reported in Fig. 6.1, with indication of the main features. It consists of a linear three sector combustion chamber equipped with effusion cooled liners. The rig allows to test under representative flow conditions and in a relevant environment the cooling system and sets the goal to provide a wide database in terms of metal temperature that can be used to validate the thermal design of the hardware. Key components of the test section, such as the injectors and the liner walls, are fabricated using DMLS and their validation at an high TRL level can represent an important step toward the future implementation of laser sintering manufacturing methodologies in the engine design process.

The combustor rig is directly connected through flanged interfaces to the test facility and is characterized by a modular layout in order to allow the potential replacement of the test components. Air required for the test campaign is delivered by two screw compressors with a maximum flow rate

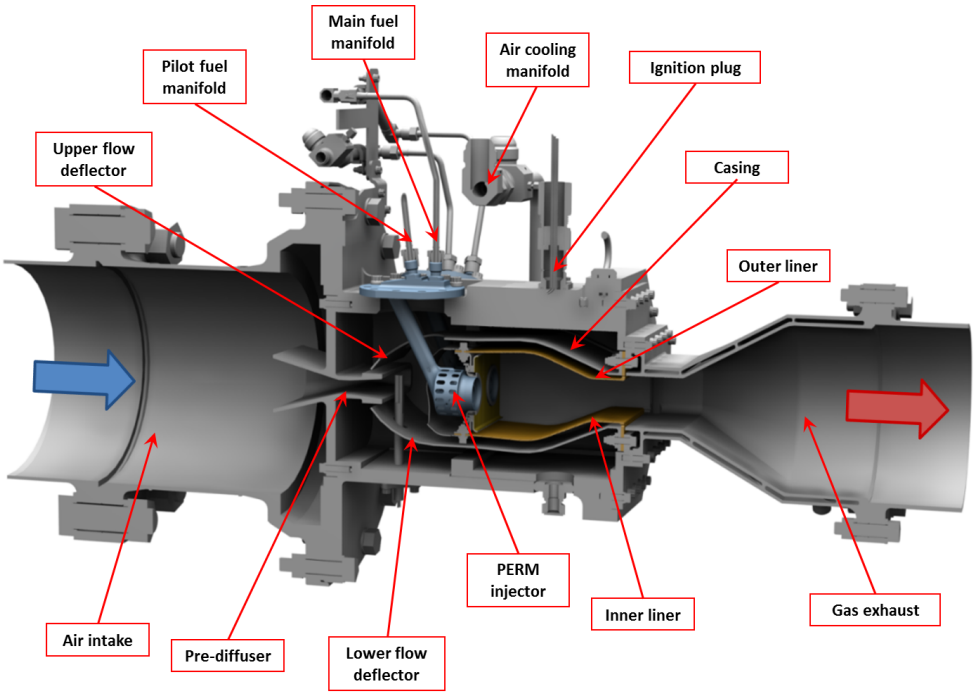

Figure 6.1: Cross sectional view of the reactive combustor rig

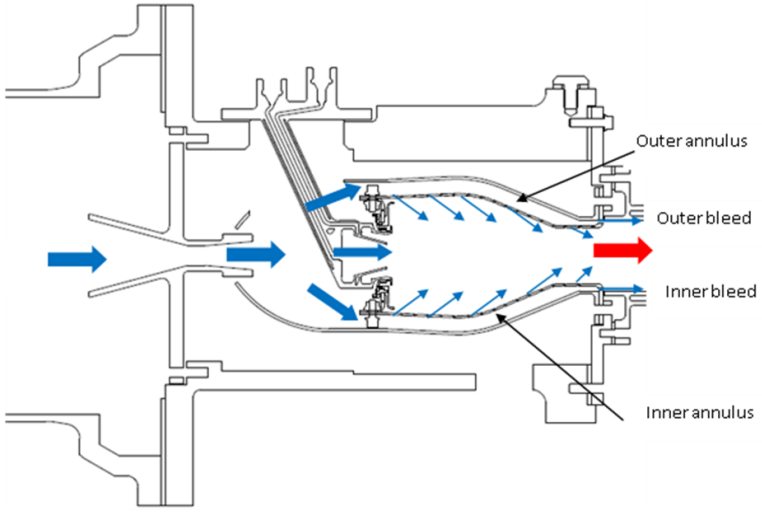

Figure 6.2: Air flow distribution across the combustor

capability equal to $1kg/s$ at a maximum pressure of $10bar$. Before to be sent to a $600kW$ electric heater, which has the task of raising the temperature up to the target value, air crosses a dryer to remove humidity, and a $2m^3$ vessel to dump pressure fluctuations; finally compressed, heated-up air mass flow is admitted in the test rig by means of a large intake duct. The desired air mass flow rate and pressure conditions for the tests are set up throttling several valves located along the lines: one modulating valve is present at the intake of each compressor, one globe valve is located upstream the heater for the control of the mainstream and a back pressure control valve is installed at the combustor exit to set the pressure in the chamber. Mainstream mass flow rate is measured by means of a calibrated orifice (standard EN ISO 5167-1).

As illustrated in Fig. 6.2, air coming from the pre-diffuser is split up by the liner. One part of the airflow enters in the annulus to fed the effusion cooling system, while the mainstream flow is injected in the chamber through the swirler with the combustible.

Analogously to the experimental campaign conducted at isothermal conditions, the set of swirlers is composed of three PERM (Partially Evaporating and Rapid Mixing) injectors, in this case, the components are realized by DMLS and are comprehensibly equipped with the fuel adduction lines (Fig. 6.3). PERM concept is based on a double swirler airblast atomizer

Figure 6.3: PERM injector fabricated by rapid prototyping (courtesy of Avio Aero)

developed in order to achieve partial evaporation inside the inner duct and rapid mixing within the combustor. It is composed by two separate radial co-rotating swirlers used to impose angular momentum on two distinct inlet air flows; finally an outer and an inner nozzles accelerate the swirled flows before they enter into the combustion region. The primary fuel is supplied by a central pressure atomizer (*pilot*), while the secondary fuel (*main*) is issued by internal channels creating a liquid film onto the internal nozzle

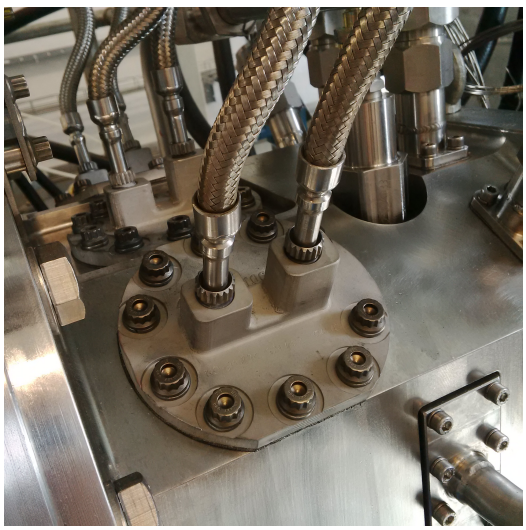

Figure 6.4: Combustor fuel manifolds

surface that separates the two co-rotating swirling flows. A picture of the fuel manifolds connected to the three injectors installed in the combustor rig is reported in Fig. 6.4.

The dedicated skid fuel reported in Fig. 6.5 has been realized to feed the two distinct lines. Fuel mass flow rates are measured by means of Coriolis mass flow-meters and are regulated acting on two automatic control valves. A volumetric gear pump has the task to convey the combustible to the skid fuel from an intermediate tank, which is in turns supplied by a self-priming pump that collects the fuel Jet-A1 stored outside the facility in three underground storage tanks with a capacity of $500l$ each. The fuel lines are also connected to a Nitrogen tank in order to perform before and after the ignition a purge of the feeding channels. In addition, Nitrogen is injected in case of emergency to extinguish the flame.

The other parts of the chamber manufactured by Direct Metal Laser Sin-

Figure 6.5: Test cell skid fuel

tering are the effusion cooled inner and outer liners, a picture of the tested component is showed in Fig. 6.6. The effusion system is consistent with real engine geometry in terms of wall thickness and cooling holes pattern: hole diameter, hole inclination angle and streamwise and spanwise holes pitch are directly derived from a representative cooling configuration. Each of the two liner is equipped with 30 K-type thermocouples directly embedded within the plate, in order to continuously check the metal temperature. From the combustor annulus two air bleeds are arranged according to the scheme of Fig. 6.2.

The heat shield protecting the combustor dome is cooled by an impingement system, while the temperature of the side walls of the chamber is lowered by forced convection on the cold side by means of a dedicated air cooling network. For the thermal management of the exhaust duct, a water jacket solution is implemented, coupled with a set of four radial water spray nozzles, which thanks to the injected liquid evaporation, considerably reduce the hot gases temperature, safeguarding the integrity of the back-pressure valve and the chimney stack.

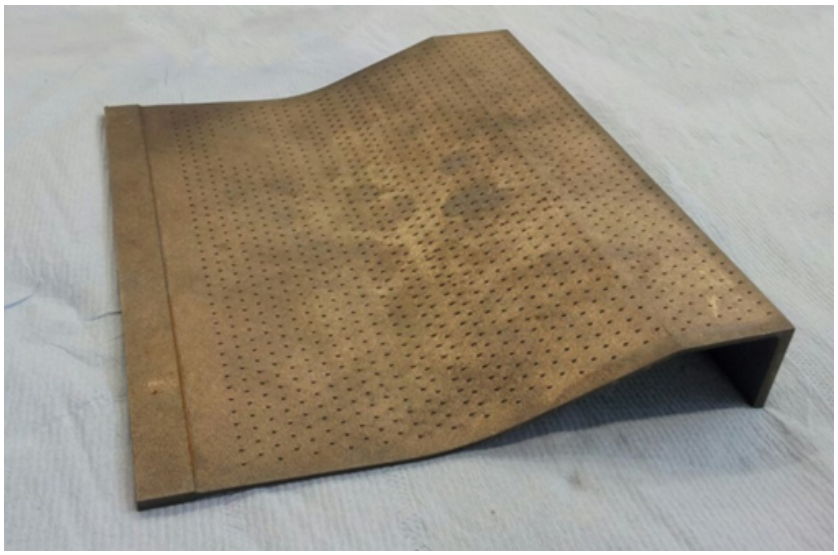

Figure 6.6: Effusion liner (courtesy of Avio Aero)

To perform an optical survey of the flame during the operation, the combustor rig is equipped with an high temperature borescope, which allows to inspect and analyse areas that otherwise would be inaccessible to standard remote viewing instruments. The component is designed for use at operating temperatures up to $2000°C$ and is provided of a closed-loop water cooling system. A CCD digital camera Sony XCD-SX90CR is connected to the high temperature borescope and permits to acquire videos with a resolution of 1280 x 960 pixel, operating with a frame rate of $20 fps$. The flame detector optical apparatus is installed in the rig outlet duct as showed in Fig. 6.7. Furthermore, the test rig is equipped with a wide range of measurement instrumentation and with a large number of sensors, in order to efficiently govern the rig operating conditions:

Pressure measurement

- One total pressure rake is installed immediately downstream the prediffuser exit. The rake achieves the pressure value at three different radial locations, allowing the evaluation of the inlet stream characteristics.

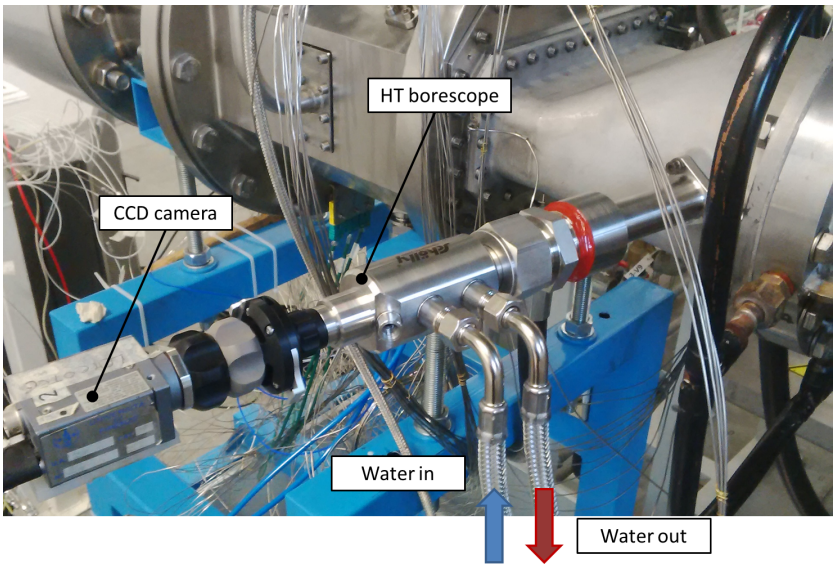

Figure 6.7: Flame detector optical device

- Two static pressure probes are placed on the cowl, on upper and lower walls, in line with the central injector.
- Four static pressure are installed to evaluate the combustion chamber pressure, two on the upper liner and two on the lower liner, at two different axial position.
- Two static pressure probes are positioned in the annulus, one in the upper and the other in the lower channel, in order to evaluate the annulus flow distribution.
- Two static pressure taps monitor the pressure drop through air cooling network of the chamber lateral walls.
- One PCB probe for unsteady pressure measurement is placed in the chamber, aiming to detect turbulent fluctuations and combustion instability.

Pressure measurements are carried out employing three 9116 NetScanner®System acquisition modules, covering overall a pressure range from $5psi$ to $250psi$. Each scanner integrates 16 silicon piezo-resistive pressure sensors, which provide a guaranteed system accuracy of up to $\pm 0.05\%$ of the full scale.

Temperature measurement

- One RTD temperature sensor is positioned in the inlet air intake.
- One rake with three total temperature probes is located at the diffuser exit, aimed at characterizing the inlet flow.
- Three static temperature probes are placed along each annulus channel at three different axial position, in order to evaluate gas thermal raising along the liner.
- Twelve thermocouples will be placed on the rig lateral walls, at 3 axial locations, to monitor thermal behaviour of the air-cooled lateral walls.

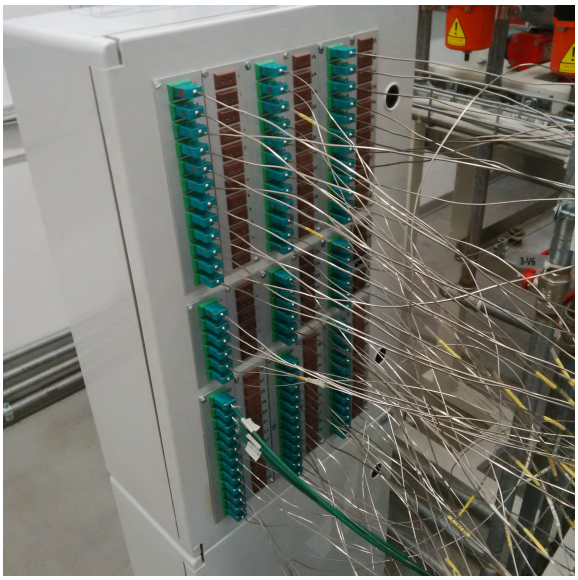

Figure 6.8: Reference cold junction with 90 K-type thermocouples connected

- Three RTD temperature sensors are employed to manage the water cooling closed-loop network, one detector measures the water inlet temperature, while the other two sensors are designated to check the temperatures in the hot water return lines respectively of the rig water jacket and of the high-temperature boroscope cooling system.
- Four metal thermocouples will monitor thermal behaviour of the water cooled exhaust hot-gas duct.
- Two thermocouples are placed on the external casing at different axial positions.
- Thirty thermocouples are braze-welded on each of the two liners, 10 axial locations in line with the central injector, aimed to monitor thermal distribution and peaks.
- Three metal thermocouples are located on the central heat shield at different circumferential position ($0deg$, $120deg$ and $240deg$).

Consistently to test operating range, thermocouples of type K are selected, according to manufacturer data the guaranteed accuracy is $\pm 0.75\%$. Tem-

peratures measurement management is performed using two data acquisition/switch units Agilent 34970A, employing five multiplexer modules of 20 channels each (Agilent 34901A). A dedicated thermally insulated reference cold junction is coupled to the units in order to achieve a constant well-known temperature value for a correct compensation (Fig. 6.8). The temperature of this reference junction is measured by means of two RTD Pt100 sensors with an accuracy of $0.1K$.

6.2 Test conditions

The experimental campaign is performed imposing several operating conditions ranging among combustor typical engine values. Temperature and pressure values of the mainstream mass flow rate at the inlet of the combustor $\dot{m}_{in}$ are evaluated immediately downstream the pre-diffuser exit and are indicated respectively as T_{in} and P_{in}. Analogously to tests conducted during previous atmospheric experimental campaign, the main flow is set acting on the pressure drop across the injectors:

$$\frac{\Delta P}{P} = \frac{P_{in} - P_{out}}{P_{in}} \tag{6.1}$$

The mainstream flow number is hence evaluated as:

$$\dot{m}_{in,rid} = \frac{\dot{m}_{in} * \sqrt{T_{in}}}{P_{in}} \tag{6.2}$$

Regarding the liquid fuel Jet-A1, two distinct parameters are used to indicate the fuel air ratio of the Pilot and the Main fuel line; these parameters are defined using the total mass flow at the rig inlet:

$$FAR_{pilot} = \frac{\dot{m}_{pilot}}{\dot{m}_{in}} \tag{6.3}$$

$$FAR_{main} = \frac{\dot{m}_{main}}{\dot{m}_{in}} \tag{6.4}$$

In this preliminary phase of the experimental campaign five different operating points are selected to investigate the combustor behaviour; each acquisition is achieved when steady condition are reached and it is identified with a test ID varying from A to E. In Table 6.1 a summary of the explored operating conditions is reported. First three tests (A, B, C) are representative of diffusive flame operating conditions, increasing the temperature of the

$TestID$	$T_{in}[K]$	$P_{in}[bar]$	$\Delta P/P[\%]$	FAR_{pilot}	FAR_{main}
A	464	3.6	4.0	0.042	0.000
B	478	3.5	3.4	0.033	0.000
C	518	4.3	2.7	0.038	0.000
D	508	4.3	2.7	0.020	0.020
E	559	2.8	5.0	0.004	0.009

Table 6.1: Reported operating points

pre-heated main-flow and varying the Fuel Air Ratio of the pilot line. Test D and E are obtained travelling towards a premixed flame regime with mass flow rates split for the main fuel line respectively equal to 50% and 70%.

6.3 Preliminary results

The main outcome of the experimental campaign is represented by a large database of wall temperatures which will be useful to validate numerical methodology in a QDRV approach (Quick Design and Rapid Validation). Discrete temperature values are reported in terms of the ratio T/T_{in} where T represents the metal temperature measured by the thermocouples. According to the scheme of Fig. 6.9, ten axial measurement locations are arranged on each liner, while three different positions are taken into account in the spanwise direction.

Fig. 6.10 reports the temperature distribution along the combustor centreline both for the outer liner (top) and the inner liner(bottom) for the five test conditions previously listed in the test matrix. The shape of the trends for all the test points is characterized by a local maximum located between the 5th and the 7th measurement station, which is positioned just upstream the combustor contraction. As it is reasonable to expect, the maximum temperature respect to the inlet value is reached by the tests conducted at higher value of overall fuel air ratio (A, C and D), while the colder operating points

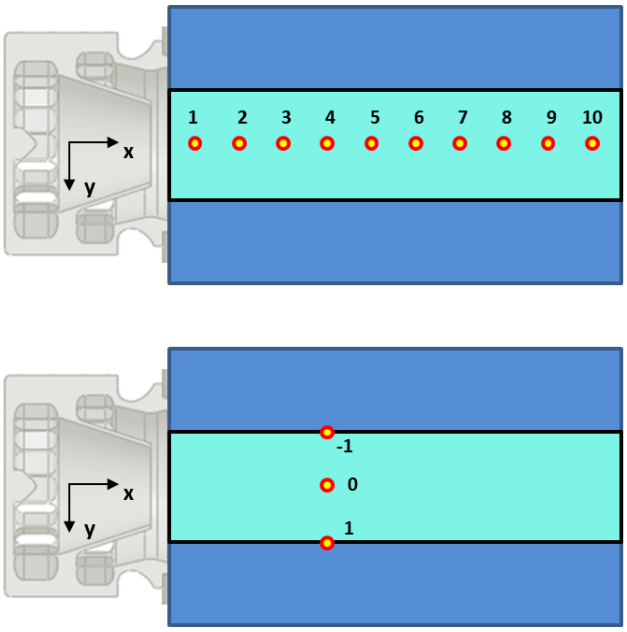

Figure 6.9: Thermocouples location on the liner surface

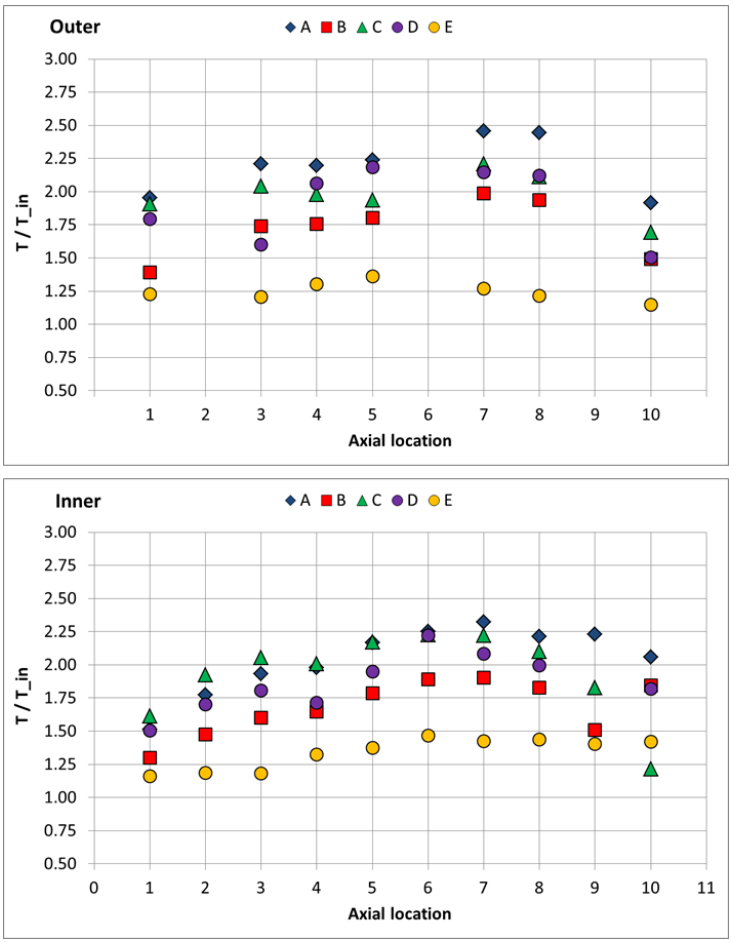

Figure 6.10: Metal temperature distributions in the streamwise direction. Outer liner: top. Inner liner: bottom

are those identified with B and, especially, E.

To analyse the effects of different flame regimes, it is interesting to compare the trends of test A, B and C with respect to those with an higher contribution of the main premixed fuel line (D and E). For diffusive flame conditions the temperature peak is established in concurrence of the 7th rows of thermocouples near the cross section contraction. The test points with a reduced contribution of the pressure atomizer show a more uniform temperature trend along the centreline moving from the first station to the last one; the temperature peak is moved upstream up to the 5th axial location. This behaviour is ascribable to the fact that the flame with only pilot fuel presents

a more extended axial propagation, while the more lean conditions have a well-defined and confined flame near the dome, this aspect is confirmed and well documented by the video acquisitions.

The two liners present metal temperature similar trends, with just slightly more uniform distributions obtained on the inner liner. For both surfaces, the maximum temperatures are achieved in the test A, with a peak value on the outer liner close to 2.5 times the inlet temperature, underling severe thermal working conditions for the combustor walls with a thermal load close to the maximum allowable.

The thermocouples installed on the liners allow also to monitor the temperature on lateral direction, Fig. 6.11 shows for all the test conditions the

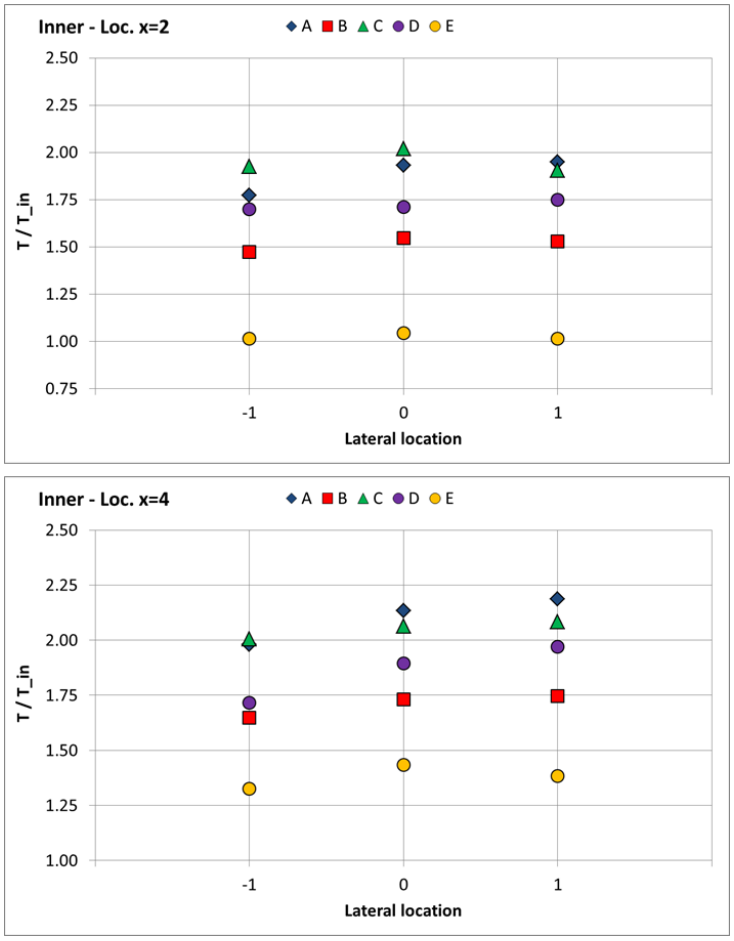

Figure 6.11: Metal temperature distributions in the spanwise direction on the outer liner

lateral temperature distribution for the measurement axial stations number 2 and 4 on the inner liner. As a general result, minor discrepancies are highlighted in the y direction for both the distributions. For the axial station 4, a slightly temperature increasing tendency is observed moving towards the right side of the test section, this behaviour is congruent with the swirler geometry rotation direction and the results obtained on the atmospheric three sector test rig.

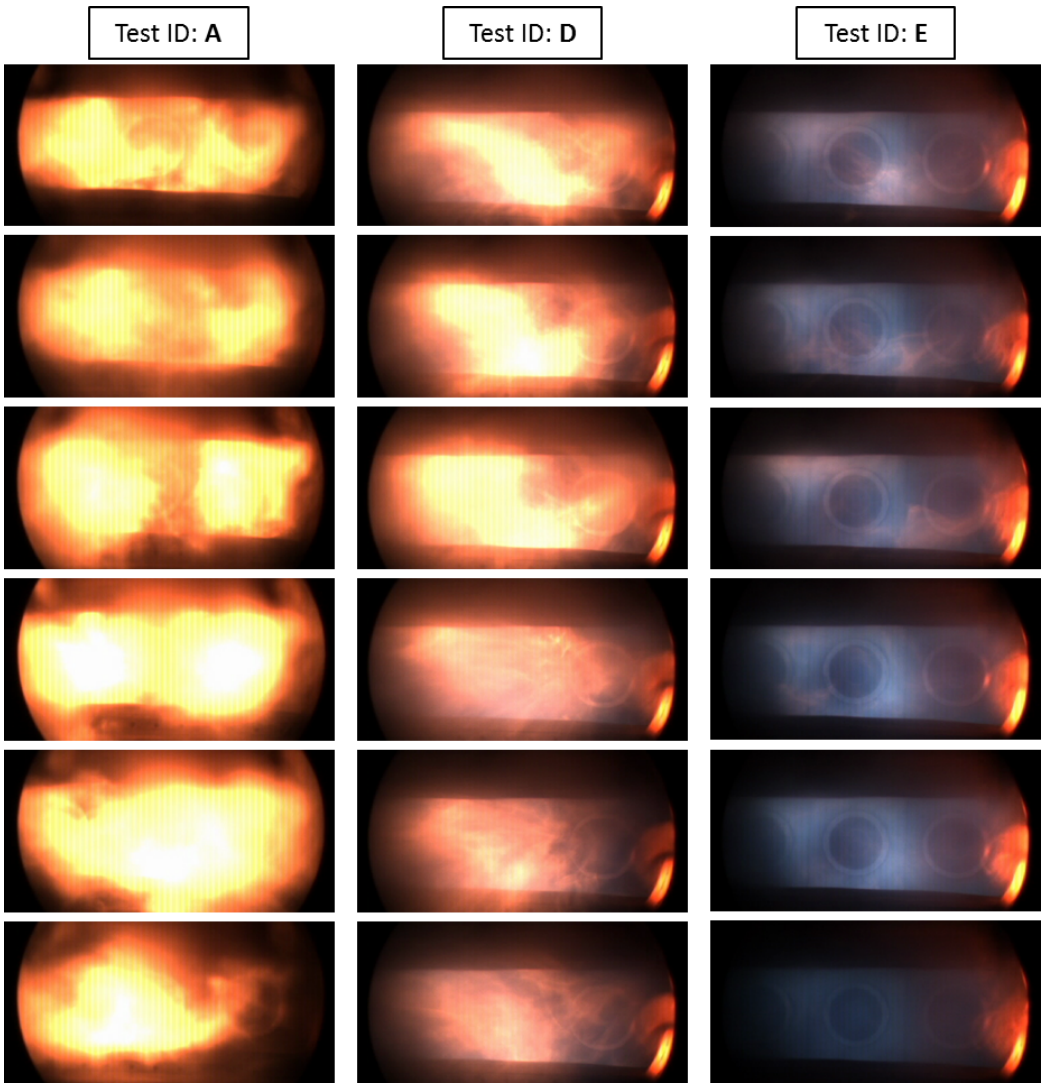

Figure 6.12: Flame video snapshots

During the operation of the VALIDATOR rig, a high-temperature boroscope is employed to record the flame behaviour using a standard CCD camera operating at $20fps$. The boroscope is placed in the exhaust duct and inclined to cover with a single image the entire dome. As an example of the acquisitions in Fig. 6.12 are reported 6 consecutive frame extracted by the video for test ID A, D and E which have appreciable differences in the imposed fuel air ratio.

As it is possible to observe, the condition with the higher pilot fuel injection has a strong light emission from the flame in the red region, displaying unsteady fluctuation and sparks of ignited droplets that reach the combustor contraction. The complete analysis of the video shows the mutual interaction between the adjacent swirlers and a randomly release of high intensity light pulses swirled up in the chamber.

Increasing the main fuel mass flow split, more stable operating conditions are achieved. The flame takes on a typical blue colouration and is confined in the first part of the chamber, solidly anchored to the injectors.

As reported in the present section, the main components manufactured by DMLS are exposed to high thermal load (close to maximum admissible metal temperature), in realistic operating conditions for several hours. Since one of the main objective of the campaign is to verify the potential of rapid prototyping technique in the combustors design, a visual inspection of the hardware is conducted at the end of this preliminary investigation. For this reason the VALIDATOR rig is disconnected from the test facility and the pictures of Fig. 6.13 are acquired.

The visual inspection shows good conditions for injectors and liners, no significant damages are observed and no passages blockages are highlighted, both in the fuel feeding lines and in the effusion cooling holes. However to better quantify the status of the hardware a metallographic analysis must be planned focussing on the regions that are subjected to the higher temperatures.

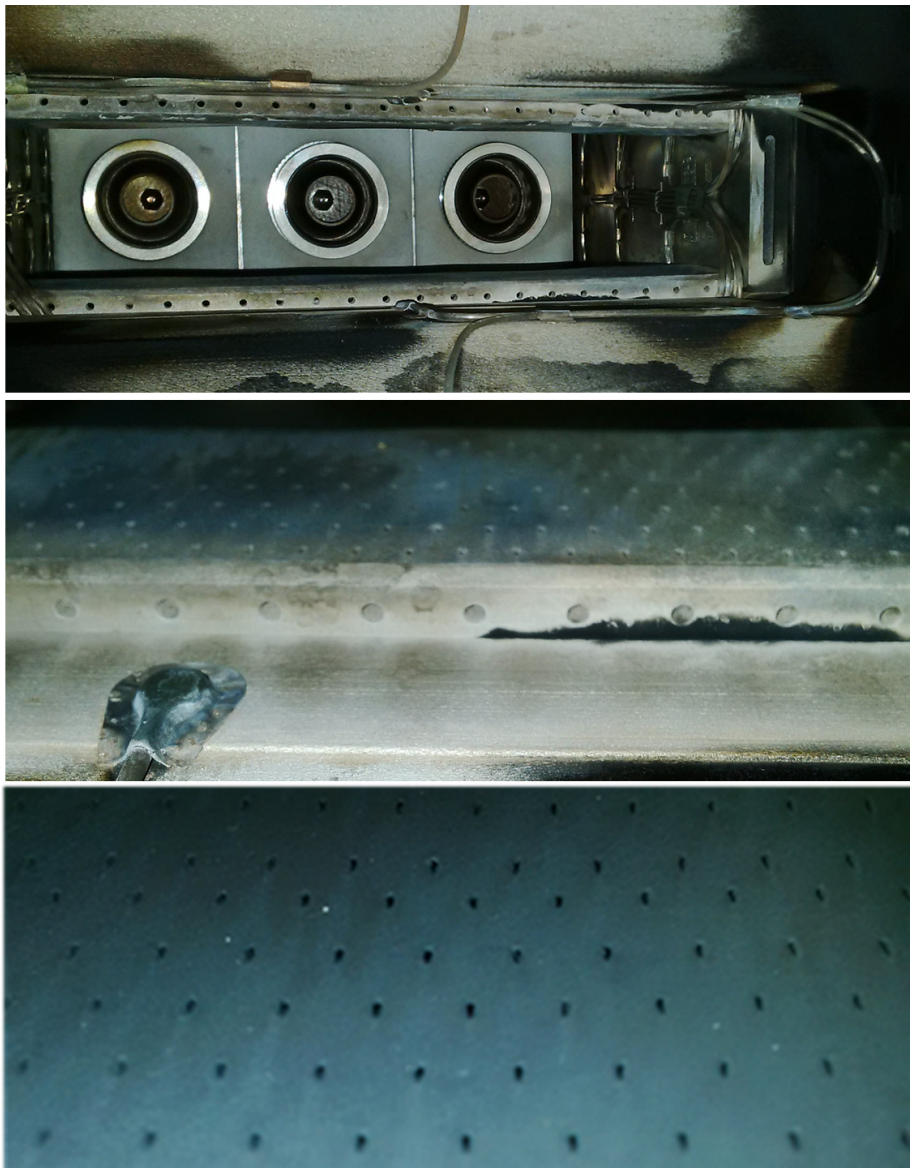

Figure 6.13: DMLS components final inspection (courtesy of Avio Aero)

Conclusions

The research activity performed during the Ph.D. course and reported in present dissertation has been set up to deepen the knowledge and draw guidelines for the thermal design of liner effusion cooling system. The study has been carried out within the framework of the European Research projects LEMCOTEC and IMPACT-AE, working together with the industrial partners Avio Aero.

Over the last years, the design of aero-engine combustors has experienced significant technological advances in the reduction of emissions, mainly with the objective of fulfilling legislative requirements regarding NO_x production. Nowadays, lean burn combustion systems are considered the most promising technology in order to concurrently meet the emissions reduction targets and guarantee a reliable and efficient combustion process; on the other hand, the high amount of air introduced directly in the combustion zone through the injection system leads to a drastic reduction of the availability of coolant for combustor cooling.

For lean burn swirl stabilized combustor architectures, current state-of-art of liner cooling technology is represented by effusion systems. This is a very efficient cooling strategy based on the use of multi-perforated walls, where metal temperature is lowered by the combined protective effect of coolant film and heat removal through forced convection inside each hole and on the annulus side.

Open literature review showed that effusion cooling has been subject of attention for many years, however the majority of works deals with cooling systems analysis under uniform mainstream conditions. Nevertheless, lean

combustor flow field is characterized by high intensive recirculation zones and strong interactions with the liner surface. For this reason, an extensive experimental investigation was carried out on different effusion cooling geometries under realistic flow conditions, generated by innovative PERM injectors.

The greater part of the results presented in this thesis was accomplished in a non-reactive planar three sector test rig, equipped with an effusion plate, reproducing the combustion chamber inner liner, and a slot system for starter film cooling that simulates the exhaust dome cooling mass flow. One of the main objective of the survey was to asses the impact of the effusion holes inclination angle, which was recognized as the most affecting geometrical parameter. Three different configurations have been tested on the three sector test rig characterized by $\alpha = 30deg$ (i.e. baseline geometry), $\alpha = 90deg$ and $\alpha = 20deg$.

Different measurement techniques were employed during the activity: a standard 2D Particle Image Velocimetry was performed on the plane orthogonal to the liner, crossing the central swirler, in order to catch the test section flow field and to highlight the interaction phenomena between swirling main flow field and the coolant flows. A steady state technique, employing Thermocromic Liquid Crystals as surface temperature detector, has been implemented to evaluate the Heat Transfer Coefficient on both the liner hot and cold side. Pressure Sensitive Paint technique has been able to provide detailed adiabatic effectiveness distributions allowing to detect the most critical regions for film covering.

PIV investigation highlights typical flow structures of a lean-burn combustion system, an expanding swirled flow with high tangential momentum jet was observed at the exit of the injector, leading to the generation of a large central recirculation zone essential for flame stabilization. Without coolant injection, a corner vortex was established underneath the jet; this structure has proven to be deeply altered in case of slot cooling activation. As a general result, the liner with perpendicular array seems to be affected by an excessive coolant jets penetration, while slanted $30deg$ geometry was

capable to generate a coherent coolant structure near the wall at the slot exit.

The heat transfer measurements on the liner hot side points out a central elliptical area with high HTC values generated by the interaction of the impinging swirled flow and the liner wall. The increase of effusion mass flow rate produces a limited enhancement in HTC for the $90deg$ plate, while the slot injection considerably inhibits the heat transfer in the first part of the liner. The $30deg$ configuration shows the higher HTC values alongside the entire liner, for this geometry a nearly negligible impact of the slot was observed. Regarding the liner cold side, the extraction of the coolant from the annulus leads to a significant enhancement of the Nusselt number which strongly contribute to the heat protection mechanism.

Adiabatic effectiveness maps show a deep impact of the injection angle on the effusion system performance. As expected, the more tilted geometry ($20deg$) leads to the best film protection, revealing a better opposition to the coolant layer destruction caused by the impinging swirled jet and showing an advantageous exploitation of superimposition effects thanks to the limited penetration of the cooling jets. Furthermore the slanted injection of effusion coolant has a beneficial impact on the slot system, extending more downstream its effects.

Possible optimizations of the cooling system were suggested by the analysis of the results. The design of an effusion array with variable porosity represents a suitable solution to correctly arrange the coolant extraction. The introduction of a double wall concept to enhance the heat transfer on the plate cold side could be an interesting feature in the central region of the liner, characterized by high heat flux and critical film covering, due to the strong coolant layer deterioration produced by the impinging gas flow.

To increase the TRL (Technology Readiness Level) of the survey, an analogous test case, consisting of a planar three sector chamber equipped with effusion cooled liners, was tested under reactive conditions in a specifically developed rig. Main goals were to validate the cooling configuration under representative operating conditions and to identify design criteria for the

development of combustor components manufactured with rapid prototyping technique. Several operating points were investigated in a preliminary experimental phase, varying the inlet flow conditions, the overall Fuel Air Ratio and the mass flow split between pilot and main fuel feeding lines. An extensive database of liner metal temperatures was acquired by means of a large number of thermocouples installed in the rig. During the test, the liners were subjected to temperatures very close to allowable limit; different thermal distributions were pointed out moving from diffusive to premixed flame behaviour.

In accordance with the actual scenario of modern aero-engine combustors, the thorough investigation carried out in this study aims to contribute to the comprehension of effusion cooling behaviour within lean burn combustion chamber, extending available experimental data. Obviously, the analysis on this topic was not completed and a deeper understanding is mandatory to increase the confidence for a reliable design. In this context, the implementation of proposed cooling system optimization strategies represents a feasible goal for future investigations. In addition, the reactive facility developed within this work must be further exploited, as well as the potentiality of addictive manufacturing methods in aero-engine field.

Bibliography

[1] D. Ballal and J. Zelina. Progress in aeroengine technology (1939-2003). *Journal of Aircraft*, 41:43–50, 2004.

[2] ICAO International Civil Aviation Organization. 2015: Air transport yearly monitor. Technical report, 2015.

[3] IATA International Air Transport Association. Press release no.: 55. Technical report, 2015.

[4] A.H. Lefebvre. *Gas Turbine Combustion*. Taylor & Francis, 1998.

[5] Flightpath 2050 Europe's Vision for Aviation. Report of the high level group on aviation research. Technical report, European Commission, 2011.

[6] R. Pavri and G.D. Moore. Ger-4211 - gas turbine emissions and control. Technical report, GE Energy Services, 2001.

[7] Y. Zeldovich, D. Frank-Kamenetskii, and P. Sadovnikov. *Oxidation of Nitrogen in Combustion*. Publ. House of the Acad of Sciences of USSR, 1947.

[8] M. Khosravy. Review of the new combustion technologies in modern gas turbines. In *Progress in Gas Turbine Performance*. InTech, jun 2013. doi: 10.5772/54403.

[9] G.J. Micklow, S. Roychoudhury, H.L. Nguyen, and M.C. Cline. Emissions reduction by varying the swirler airflow split in advanced gas tur-

bine combustors. *Journal of Engineering for Gas Turbines and Power*, 115(3):563–569, July 1993. ISSN 0742-4795.

[10] C.L. Ford, J.F. Carrotte, and A.D. Walker. The impact of compressor exit conditions on fuel injector flows. *Journal of Engineering for Gas Turbines and Power*, 134:111504–111504, 2012. doi: 10.1115/1.4007025.

[11] Y. Huang and V. Yang. Dynamics and stability of lean-premixed swirl-stabilized combustion. *Progress in Energy and Combustion Science*, 35 (4):293–364, 2009. ISSN 0360-1285.

[12] A.H. Lefebvre. Airblast atomization. *Progress in Energy and Combustion Science*, 6(3):233–261, jan 1980. doi: 10.1016/0360-1285(80) 90017-9.

[13] A. Andreini, G. Caciolli, B. Facchini, A. Picchi, and F. Turrini. Experimental investigation of the flow field and the heat transfer on a scaled cooled combustor liner with realistic swirling flow generated by a lean-burn injection system. *Journal of Turbomachinery*, 137(3):031012, oct 2014. doi: 10.1115/1.4028330.

[14] A. Peschiulli, N. Zarzalis, L. Bucchieri, and I. Da Costa. Perm injection system development and perm injection system validation. In *European Workshop on New Aero Engine Concepts*, 2010.

[15] S. Marinov, M. Kern, K. Merkle, N. Zarzalis, A. Peschiulli, F. Turrini, and O.N. Sara. On swirl stabilized flame characteristics near the weak extinction limit. In *Volume 2: Combustion, Fuels and Emissions, Parts A and B*. ASME International, 2010. doi: 10.1115/gt2010-22335.

[16] ACARE Advisory Council for Aeronautical Research in Europe. Strategic research agenda. Technical report, ACARE, 2000.

[17] D.G. Lilley. Swirl flows in combustion: a review. *AIAA Journal*, 15 (8), 1977.

[18] B.T. Vu and F.C. Gouldin. Flow measurements in a model swirl combustor. *AIAA Journal*, 20(5):642–651, may 1982. doi: 10.2514/3.51122.

[19] D.L. Rhode, D.G. Lilley, and D.K. McLaughlin. Mean flowfields in axisymmetric combustor geometries with swirl. *AIAA Journal*, 21:pp. 593–600, 1983.

[20] R.D. Brum and G.S. Samuelson. Two-component laser anemometry measurements of non-reacting and reacting complex flows in a swirl-stabilized model combustor. *Experiments in Fluids*, 5:pp. 95–102, 1987.

[21] N. Syred, T. O'Doherty, and D. Froud. The interaction of the precessing vortex core and reverse flow zone in the exhaust of a swirl burner. *Proceedings of the Institution of Mechanical Engineers, Part A: Journal of Power and Energy*, 208:pp. 27–36, 1994.

[22] A. Spencer, D. Hollis, and J. Carrotte. PIV measurements of combustor turbulence fields. In *Volume 2: Turbo Expo 2007*. ASME International, 2007. doi: 10.1115/gt2007-28050.

[23] A. Spencer, D. Hollis, and S. Gashi. Investigation of the unsteady aerodynamics of an annular combustor using PIV and LES. In *Volume 3: Combustion, Fuels and Emissions, Parts A and B*. ASME International, 2008. doi: 10.1115/gt2008-50277.

[24] M. Gnirß and C. Tropea. Simultaneous PIV and concentration measurements in a gas-turbine combustor model. *Experiments in Fluids*, 45(4):643–656, jun 2008. doi: 10.1007/s00348-008-0518-0.

[25] B. Wurm, A. Schulz, and H.J. Bauer. A new test facility for investigating the interaction between swirl flow and wall cooling films in combustors. In *Volume 3: Heat Transfer, Parts A and B*. ASME International, 2009. doi: 10.1115/gt2009-59961.

[26] G. Li and E.J. Gutmark. Effects of swirler configurations on flow structures and combustion characteristics. In *Volume 1: Turbo Expo 2004*. ASME International, 2004. doi: 10.1115/gt2004-53674.

[27] B. Wurm, A. Schulz, H.J. Bauer, and M. Gerendas. Impact of swirl flow on the cooling performance of an effusion cooled combustor liner. *Journal of Engineering for Gas Turbines and Power*, 134(12):121503–121503, October 2012. ISSN 0742-4795. doi: 10.1115/1.4007332.

[28] M. Kern, S. Marinov, P. Habisreuther, N. Zarzalis, A. Peschiulli, and F. Turrini. Characteristics of an ultra-lean swirl combustor flow by LES and comparison to measurements. In *Volume 2: Combustion, Fuels and Emissions, Parts A and B*. ASME International, 2011. doi: 10.1115/gt2011-45300.

[29] M. Berrino, F. Satta, M. Ubaldi, P. Zunino, S. Colantuoni, and P. Di Martino. Experimental characterization of the flow-field downstream of an innovative ultra low NOx injection system. In *Volume 4A: Combustion, Fuels and Emissions*. ASME International, jun 2014. doi: 10.1115/gt2014-25459.

[30] A. Andreini, B. Facchini, L. Mazzei, L. Bellocci, and F. Turrini. Assessment of aero-thermal design methodology for effusion cooled lean burn annular combustors. In *Volume 5C: Heat Transfer*. ASME International, jun 2014. doi: 10.1115/gt2014-26764.

[31] A.R. Wadia. Advanced combustor liner cooling technology for gas turbines. *Defence Science Journal*, 38(4):363–380, jan 1988. doi: 10.14429/dsj.38.5870.

[32] R. Colladay. Importance of combining convection with film cooling. In *10th Aerospace Sciences Meeting*. American Institute of Aeronautics and Astronautics (AIAA), jan 1972. doi: 10.2514/6.1972-8.

[33] G.C. Oates. *Aircraft Propulsion Systems Technology and Design*. American Institute of Aeronautics and Astronautics (AIAA), jan 1989. doi: 10.2514/4.861499.

[34] K.M.B. Gustafsson and T.G. Johansson. An experimental study of surface temperature distribution on effusion-cooled plates. *Journal of Engineering for Gas Turbines and Power*, 123:308–316, 2001.

[35] A. Andreini, G. Caciolli, B. Facchini, L. Tarchi, D. Coutandin, A. Peschiulli, and S. Taddei. Density ratio effects on the cooling performances of a combustor liner cooled by a combined slot/effusion system. In *Volume 4: Heat Transfer, Parts A and B*. ASME International, jun 2012. doi: 10.1115/gt2012-68263.

[36] V. Bellucci, P. Flohr, and C. Paschereit. Impedance of perforated screen with bias flow. *AIAA Paper*, pages 2002 – 2437, 2002.

[37] J. Rupp, J. Carrotte, and A. Spencer. Interaction between the acoustic pressure fluctuations and the unsteady flow field through circular holes. *Journal of Engineering for Gas Turbines and Power*, 132(6):061501–061501, March 2010. ISSN 0742-4795. doi: 10.1115/1.4000114.

[38] R. J. Goldstein. Film cooling. *Advances in Heat Transfer*, 7:321–379, 1971.

[39] E.R.G. Eckert. Analysis of film cooling and full-coverage film cooling of gas turbine blades. *Journal of Engineering for Gas Turbines and Power*, 106(1):206–213, January 1984. ISSN 0742-4795. doi: 10.1115/1.3239536.

[40] B. Sen, D. L. Schmidt, and D. G. Bogard. Film cooling with compound angle holes: Heat transfer. *Journal of Turbomachinery*, 118:800–806, 1996.

[41] G.B. Kelly and D.G. Bogard. An investigation of the heat transfer for full coverage film cooling. In *Volume 5: Turbo Expo 2003, Parts A and B*. ASME International, 2003. doi: 10.1115/gt2003-38716.

[42] D.E. Metzger, D.I. Takeuchi, and P.A. Kuenstler. Effectiveness and heat transfer with full-coverage film cooling. *Journal of Engineering for Power*, 95:180–184, 1973.

[43] R. E. Mayle and F. J. Camarata. Multihole cooling film effectiveness and heat transfer. *Journal of Heat Transfer*, 97, 1975.

[44] M.E. Crawford, W.M. Kays, and R.J. Moffat. Full-coverage film cooling-part i: Comparison of heat transfer data for three injection angles. *Journal of Engineering for Power*, 102(4):1000–1005, October 1980. ISSN 0742-4795. doi: 10.1115/1.3230334.

[45] M.E. Crawford, W.M. Kays, and R.J. Moffat. Full-coverage film cooling-part ii: Heat transfer data and numerical simulation. *Journal of Engineering for Power*, 102(4):1006–1012, October 1980. ISSN 0742-4795. doi: 10.1115/1.3230335.

[46] G.E. Andrews, A.A. Asere, M.L. Gupta, M.C. Mkpadi, and A. Tirmahi. Full coverage discrete hole film cooling: The influence of the number of holes and pressure loss. In *Volume 4: Heat Transfer Electric Power Industrial and Cogeneration*. ASME International, jun 1990. doi: 10.1115/90-gt-061.

[47] G.E. Andrews, F. Bazdidi-Tehrani, C.I. Hussain, and J.P. Pearson. Small diameter film cooling hole heat transfer: The influence of the hole length. In *Volume 4: Heat Transfer Electric Power Industrial and Cogeneration*. ASME International, jun 1991. doi: 10.1115/91-gt-344.

[48] G.E. Andrews, I.M. Khalifa, A.A. Asere, and F. Bazdidi-Tehrani. Full coverage effusion film cooling with inclined holes. In *Volume 4: Heat Transfer Electric Power Industrial and Cogeneration*. ASME International, jun 1995. doi: 10.1115/95-gt-274.

[49] S.V. Ekkad, D. Zapata, and J.C. Han. Heat transfer coefficients over a flat surface with air and co2 injection through compound angle holes using a transient liquid crystal image method. *Journal of Turbomachinery*, 119(3):580–586, July 1997. ISSN 0889-504X. doi: 10.1115/1.2841161.

[50] S.V. Ekkad, D. Zapata, and J.C. Han. Film effectiveness over a flat surface with air and co2 injection through compound angle holes using a transient liquid crystal image method. *Journal of Turbomachinery*, 119(3):587–593, July 1997. ISSN 0889-504X. doi: 10.1115/1.2841162.

[51] M. Martiny, A. Schulz, and S. Wittig. Full-coverage film cooling investigations: adiabatic wall temperatures and flow visualization. *ASME Conference Proceedings*, 95(WA/HT-4), 1995.

[52] M. Martiny, A. Schulz, and S. Wittig. Mathematical model describing the coupled heat transfer in effusion cooled combustor walls. In *Volume 3: Heat Transfer Electric Power Industrial and Cogeneration*. ASME International, jun 1997. doi: 10.1115/97-gt-329.

[53] R.F. Martinez-Botas and C.H.N. Yuen. Measurement of local heat transfer coefficient and film cooling effectiveness through discrete holes. In *Volume 3: Heat Transfer; Electric Power; Industrial and Cogeneration*. ASME International, may 2000. doi: 10.1115/2000-gt-0243.

[54] Y. Lin, B.Song, B. Li, G.Liu, and Z. Wu. Investigation of film cooling effectiveness of full-coverage inclined multihole walls with different hole arrangements. In *Volume 5: Turbo Expo 2003, Parts A and B*. ASME International, 2003. doi: 10.1115/gt2003-38881.

[55] J. J. Scrittore, K. A. Thole, and S. W. Burd. Investigation of velocity profiles for effusion cooling of a combustor liner. *Journal of Turbomachinery*, 129(3):518, 2007. doi: 10.1115/1.2720492.

[56] P. Ligrani, M. Goodro, M. Fox, and H.K. Moon. Full-coverage film cooling: Film effectiveness and heat transfer coefficients for dense and sparse hole arrays at different blowing ratios. *Journal of Turbomachinery*, 134(6):061039, 2012. doi: 10.1115/1.4006304.

[57] V.U. Kakade, S.J. Thorpe, and M. Gerendas. Effusion-cooling performance at gas turbine combustor representative flow conditions. In *Volume 4: Heat Transfer, Parts A and B*. ASME International, jun 2012. doi: 10.1115/gt2012-68115.

[58] A. Andreini, B. Facchini, A. Picchi, L. Tarchi, and F. Turrini. Experimental and theoretical investigation of thermal effectiveness in multiperforated plates for combustor liner effusion cooling. *Journal of Turbomachinery*, 136(9):091003, mar 2014. doi: 10.1115/1.4026846.

[59] Z. Huang, Y.B. Xiong, Y.Q. Liu, P.X. Jiang, and Y.H. Zhu. Experimental investigation of full-coverage effusion cooling through perforated flat plates. *Applied Thermal Engineering*, 76:76–85, feb 2015. doi: 10.1016/j.applthermaleng.2014.11.056.

[60] J. Krawciw, D. Martin, and P. Denman. Measurement and prediction of adiabatic film effectiveness of combustor representative effusion arrays. In *Volume 5B: Heat Transfer*. ASME International, jun 2015. doi: 10.1115/gt2015-43210.

[61] G. Wang, G. Ledezma, J. DeLancey, and A. Wang. Experimental and numerical investigations of effusion cooling for high pressure turbine components: Part 1 - experimental study with PSP. In *Volume 5B: Heat Transfer*. ASME International, jun 2016. doi: 10.1115/gt2016-56398.

[62] T. Jackowski, A. Schulz, H.J. Bauer, M. Gerendás, and T. Behrendt. Effusion cooled combustor liner tiles with modern cooling concepts: A comparative experimental study. In *Volume 5B: Heat Transfer*. ASME International, jun 2016. doi: 10.1115/gt2016-56598.

[63] K.R. Vinton, S. Nahang-Toudeshki, L.M. Wright, and A. Carter. Full coverage film cooling performance for combustor cooling manufactured using DMLS. In *Volume 5B: Heat Transfer*. ASME International, jun 2016. doi: 10.1115/gt2016-56504.

[64] J. C. Vogel and J. K. Eaton. Combined heat transfer and fluid dynamic measurements downstream of a backward-facing step. *International Journal of Heat and Mass Transfer*, 107:922–929, 1985.

[65] E.V. Shisnova, P.S. Roganova, S.I. Grabarnika, and V.P. Zabolotskya. Heat transfer in the recirculating region formed by a backward-facing step. *International Journal of Heat and Mass Transfer*, 31:1557–1562, 1988.

[66] F. Maiuolo, B. Facchini, L. Tarchi, and D. Coutandin. Experimental investigation on the effects of a large recirculating area on the perfor-

mance of an effusion cooled combustor liner. *Journal of Engineering for Gas Turbines and Power*, 134:041505–1–9, 2012.

[67] S. Patil, S. Abraham, D. Tafti, S. Ekkad, Y. Kim, P. Dutta, H.K. Moon, and R. Srinivasan. Experimental and numerical investigation of convective heat transfer in a gas turbine can combustor. *Journal of Turbomachinery*, 133, 2011. doi: 10.1115/1.4001173.

[68] S. Patil, T. Sedalor, D. Tafti, S. Ekkad, Y. Kim, P. Dutta, H.K. Moon, and R. Srinivasan. Study of flow and convective heat transfer in a simulated scaled up low emission annular combustor. *Journal of Thermal Science and Engineering Applications*, 3, 2011. doi: 10.1115/1.4004531.

[69] B. Wurm, A. Schulz, H.J. Bauer, and M. Gerendas. Cooling efficiency for assessing the cooling performance of an effusion cooled combustor liner. In *Volume 3B: Heat Transfer*. ASME International, jun 2013. doi: 10.1115/gt2013-94304.

[70] A. Andreini, R. Becchi, B. Facchini, L. Mazzei, A. Picchi, and F. Turrini. Adiabatic effectiveness and flow field measurements in a realistic effusion cooled lean burn combustor. *Journal of Engineering for Gas Turbines and Power*, 138(3):031506, sep 2015. doi: 10.1115/1.4031309.

[71] A. Andreini, B. Facchini, R. Becchi, A. Picchi, and F. Turrini. Effect of slot injection and effusion array on the liner heat transfer coefficient of a scaled lean-burn combustor with representative swirling flow. *Journal of Engineering for Gas Turbines and Power*, 138(4):041501, oct 2015. doi: 10.1115/1.4031434.

[72] T. Behrendt, T. Lengyel, C. Hassa, and M. Gerendas. Characterization of advanced combustor cooling concepts under realistic operating conditions. In *Volume 4: Heat Transfer, Parts A and B*. ASME International, 2008. doi: 10.1115/gt2008-51191.

[73] Y. Ji, B. Ge, S. Zang, J. Yu, and J. Zhang. Experimental investigation of effusion cooling performance on the liner of a scaled three injector

annular combustor. In *Volume 5B: Heat Transfer*. ASME International, jun 2016. doi: 10.1115/gt2016-57035.

[74] M. Gerendas, K. Hoschler, and T. Schilling. Development and modeling of angles effusion cooling for the br715 low emission staged combustor core demonstrator. *RTO AVT Symposium on Advanced Flow Management: Part B - Heat Transfer and Cooling in Propulsion and Power Systems*, NATO Research and Technology Organisation, 2001.

[75] E. M. Sparrow and R. G. Kemink. Heat transfer downstream of a fluid withdrawal branch in a tube. *Journal of Heat Transfer*, 101(1): 23, 1979. doi: 10.1115/1.3450923.

[76] A.R. Byerley, P.T. Ireland, T.V. Jones, and S.A. Ashton. Detailed heat transfer measurements near and within the entrance of a film cooling hole. In *Volume 4: Heat Transfer; Electric Power; Industrial and Cogeneration*. ASME International, jun 1988. doi: 10.1115/88-gt-155.

[77] A.R. Byerley. *Heat transfer near the entrance to a film cooling hole in a gas turbine blade*. PhD thesis, Merton College, Oxford, 1989.

[78] H.H. Cho. Effect of plenum crossflow on heat (mass) transfer near and within the entrance of film cooling holes. *Journal of Turbomachinery*, 119(4):761, oct 1997. doi: 10.1115/1.2841186.

[79] I. Ieronymidis, D. R. H. Gillespie, P.T. Ireland, and R. Kingston. Detailed heat transfer measurements in a model of an integrally cast cooling passage. *Journal of Turbomachinery*, 132(2):021002, 2010. doi: 10.1115/1.3140283.

[80] G. Cottin, E. Laroche, N. Savary, and P. Millan. Modeling of the heat flux for multi-hole cooling applications. In *Volume 5: Heat Transfer, Parts A and B*. ASME International, 2011. doi: 10.1115/gt2011-46330.

[81] A. Andreini, G. Caciolli, R. Da Soghe, B. Facchini, and L. Mazzei. Numerical investigation on the heat transfer enhancement due to coolant

extraction on the cold side of film cooling holes. In *Volume 5B: Heat Transfer*. ASME International, jun 2014. doi: 10.1115/gt2014-25460.

[82] R. Da Soghe, A. Andreini, B. Facchini, and L. Mazzei. Heat transfer enhancement due to coolant extraction on the cold side of effusion cooling plates. *Journal of Engineering for Gas Turbines and Power*, 137(12):122609, jul 2015. doi: 10.1115/1.4030837.

[83] M. Raffel, C. E. Willert, S. Wereley, and J. Kompenhans. *Particle Image Velocimetry*. Springer-Verlag Berlin Heidelberg, 2nd edition, 2007. doi: 10.1007/978-3-540-72308-0.

[84] C. Tropea, A. Yarin, and J. F. Foss. *Springer Handbook of Experimental Fluid Mechanics*. Springer-Verlag Berlin Heidelberg, 1st edition, 2007.

[85] D.J. Farina, J.M. Hacker, R.J. Moffat, and J.K. Eaton. Illuminant invariant calibration of thermochromic liquid crystals. *Experimental Thermal and Fluid Science*, 9(1):1 – 12, 1994. ISSN 0894-1777. doi: 10.1016/0894-1777(94)90002-7.

[86] T.L. Chan, S. Ashforth-Frost, and K. Jambunathan. Calibrating for viewing angle effect during heat transfer measurements on a curved surface. *International Journal of Heat and Mass Transfer*, 44:2209–2223, 2001.

[87] Inc. Innovative Scientific Solutions. Psp basics. URL `http://psp-tsp.com/`.

[88] K.R. Navarra. *Development of the Pressure-Sensitive-Paint Technique for Turbomachinery Applications*. Virginia Polytechnic Institute and State University, 1997.

[89] J.C. Han and P. Rallabandi. Turbine blade film cooling using PSP technique. *Frontiers in Heat and Mass Transfer*, 1, 2010.

[90] M.E. Crawford and W.M. Kays. Convective heat and mass transfer. *McGraw-FEE*, 1993.

[91] T. V. Jones. Theory for the use of foreign gas in simulating film cooling. *International Journal of Heat and Fluid Flow*, 20:349–354, 1999.

[92] D. Charbonnier, P. Ott, M. Jonsson, F. Cottier, and T. Kobke. Experimental and numerical study of the thermal performance of a film cooled turbine platform. In *Volume 3: Heat Transfer, Parts A and B*. ASME International, 2009. doi: 10.1115/gt2009-60306.

[93] S. J. Kline and F. A. McClintock. Describing uncertainties in single sample experiments. *Mechanical Engineering*, 75:3–8, Jan 1953.

[94] Ente Nazionale di Unificazione UNI. *Measurerement of fluid flow by means of pressure differential devices*, volume UNI EN ISO 5167-1. UNI, sept 1997.

[95] J Westerweel. Fundamentals of digital particle image velocimetry. *Measurement Science and Technology*, 8(12):1379–1392, dec 1997. doi: 10.1088/0957-0233/8/12/002.

[96] A. Picchi. *Experimental Investigations of Effusion Cooling Systems for Lean Burn Aero-Engine Combustors*. PhD thesis, Department of Industrial Engineering - University of Florence, 2013.

[97] P.E. Roach. The generation of nearly isotropic turbulence by means of grids. *International Journal of Heat and Fluid Flow*, 8(2):82 – 92, 1987. ISSN 0142-727X. doi: 10.1016/0142-727X(87)90001-4.

[98] B. Facchini, F. Maiuolo, L. Tarchi, and D. Coutandin. Combined effect of slot injection, effusion array and dilution hole on the heat transfer coefficient of a real combustor liner: Part 1—experimental analysis. In *Volume 4: Heat Transfer, Parts A and B*. ASME International, 2010. doi: 10.1115/gt2010-22936.

[99] D.H. Rhee, P.H. Yoon, and H. H. Cho. Local heat/mass transfer and flow characteristics of array impinging jets with effusion holes ejecting spent air. *International Journal of Heat and Mass Transfer*, 46(6): 1049–1061, mar 2003. doi: 10.1016/s0017-9310(02)00363-0.

[100] F. Haselbach and R. Parker. Hot end technology for advanced, low emission large civil aircraft engines. *ICAS2012 - 28th International Congress of the Aeronautical Sciences*, 2012.

[101] Q. Yang, Y. Lin, Q. Xu, C. Zhang, and C.J. Sung. Cooling effectiveness of impingement/effusion cooling with and without turbulence promoter ribs. In *Volume 4: Heat Transfer, Parts A and B*. ASME International, jun 2012. doi: 10.1115/gt2012-69209.

[102] N. Rogers, Z. Ren, W. Buzzard, B. Sweeney, N. Tinker, P. Ligrani, K. Hollingsworth, F. Liberatore, R. Patel, and H.K. Moon. Effects of double wall cooling configuration and conditions on performance of full coverage effusion cooling. In *Volume 5A: Heat Transfer*. ASME International, jun 2016. doi: 10.1115/gt2016-56515.

[103] A. Andreini, R. Becchi, B. Facchini, L. Mazzei, A. Picchi, and A. Peschiulli. Effusion cooling system optimization for modern lean burn combustor. In *Volume 5B: Heat Transfer*. ASME International, jun 2016. doi: 10.1115/gt2016-57721.